Title	Pore Effects and Local Viscoelasticity at Resin-Metal Interfaces Studied by MD Simulation
Author(s)	森, 穂高
Citation	大阪大学, 2019, 博士論文
Version Type	VoR
URL	https://doi.org/10.18910/76211
rights	
Note	

Pore Effects and Local Viscoelasticity at Resin-Metal Interfaces Studied by MD Simulation

Hodaka Mori

DECEMBER 2019

Pore Effects and Local Viscoelasticity at Resin-Metal Interfaces Studied by MD Simulation

A dissertation submitted to
THE GRADUATE SCHOOL OF ENGINEERING SCIENCE
OSAKA UNIVERSITY
in partial fullfillment of the requirements for the degree of
DOCTOR OF PHILOSOPHY IN ENGINEERING

by

Hodaka Mori

DECEMBER 2019

Abstract

To understand the mechanism of adhesion, we analyze the filling of epoxy resin into nano-sized pores, and local viscoelasticity at the resin-metal interface.

In Chapter 1, atomic MD simulations were conducted for the filling of epoxy resin into a nano-sized pore formed on an aluminum surface. The epoxy resin was polyphenol mixed with polyglycidylether of *o*-cresol formaldehyde novolac and their oligomers formed through ring-opening reactions. The degree of oligomerization was varied from 0.5 to 2.5 nm in terms of the radius of gyration, and the radius of the cylindrical pore was fixed at 2.5 nm. It was observed that a smaller-sized resin penetrates into the pore along the wall, while larger resins move rather uniformly in the pore. The maximum density in the pore was observed to be larger when the resin was smaller in size. It was found that when the radius of gyration of the resin is larger than half of the pore radius, the resin density in the pore does not reach half the bulk density of the resin. This implies that the resin-resin interaction inhibits the filling of the nano-sized pore.

In Chapter 2, we extended the work of Chapter 1 into a wider examination of resins and pore sizes, and it was found that the pore is filled to several tens of % at practically employed pressure when the radius of gyration of resin is less than 10% of the pore radius. Larger resins require a very high pressure and efficient filling can only be achieved with a resin that is an order of magnitude smaller in size than the pore. The stress map was also analyzed in and around the pore, and it was observed that the local stress is not uniformly distributed unless the resin is small. This indicates that a common rate of pushing does not lead to the relaxation of the resin structure, suggesting in turn that more effective filling may be possible with reduced rate of pushing.

In Chapter 3, a spatial-decomposition formula is presented for viscoelasticity. In this formula, the relaxation modulus is decomposed with respect to the spatial coordinates, and the local viscoelasticity is analyzed with the spatiallyly decomposed stress-stress time correlation function. The spatial-decomposition formula is then applied to the planar interface between the resin and metal by using the Kremer-Grest model at a variety of adhesion strengths. It was observed that when the resin-metal interaction is strong, the resin forms a layered structure extending over a spatial range an order of magnitude larger than the segment size of the resin. The motion of the resin is suppressed there, and the effect of the interface is localized near the wall only when adhesion is weak. Actually, the layered region is more viscous than the bulk when the resin interacts strongly with the wall, where the stress-stress correlation in the layered region persists over longer times. In the spatial scale corresponding to the segment size, the resin-metal interaction does not significantly affect the elasticity and primarily modifies the decay of the local stress of the resin within the layers as a function of time. The present work demonstrates that the spatially-decomposed relaxation modulus can be a general framework for analyzing the viscoelasticity at the interface and revealing the relationship of the adhesion to the stress-stress correlation in the segment-scale space and time.

Contents

General Introduction

Adhesives in electronic devices for automobiles

Modern automobiles are controlled by electronic devices such as sensors and integrated circuits. Electric control of powertrains including engines, motors, and batteries has become essential for automobiles, and recently the targets of the control extend to advanced driver assistance systems represented by autonomous driving [1]. In an engine, for example, the exhaust gas recirculation is commonly performed to purify the exhaust gas and improve the fuel consumption, where a pressure sensor with high accuracy is used for system control [2]. Power semiconductors are also widely used to control the current and voltage of hybrid and electric vehicles. These typical electronic structures are shown in Fig. 1. Generally, these devices have a common structure, and the semiconductor silicon wafer is mounted to the substrate with an adhesive and bonded to the electrodes, and the whole assembly is further encapsulated with the resin [3–7]. Each semiconductor element is chosen by its purpose of usage and typically uses a micro-electromechanical system (MEMS) for a mechanical sensor, a photo detector for an optical sensor, a metal-oxide-semiconductor field-effect transistor for current control, and an integrated circuit for calculations. The electrode is typically platinum, aluminum, gold, or copper. In terms of heat and chemical resistances, epoxy and silicone resins are often used as the adhesive and encapsulation resin, respectively.

As shown in Fig. 1, the resin-metal interfaces exist everywhere in the internals of the electronic devices. These interfaces require a tight adhesion to prevent the intrusion of corrosive substances from the outside and while maintaining the integrity of the semiconductor element. When electronic devices are directly mounted on the engine, temperature can reach 100-150 °C and become exposed to acids, alkalis, and fuels [1]. It is here that corrosive materials may intrude into the devices when the adhesion between the resin and the component is weak. In addition, a semi-

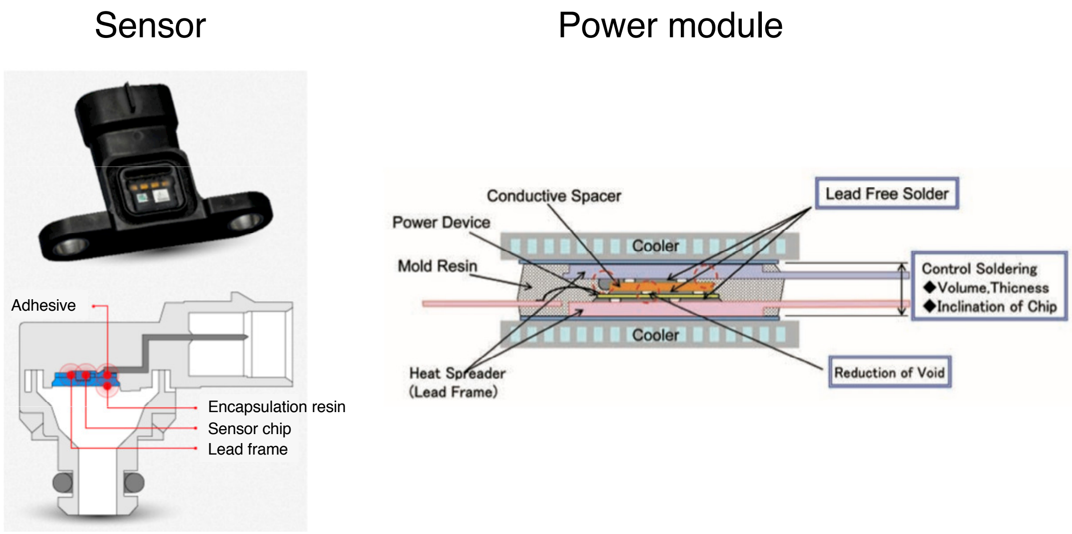

Figure 1: Typical structure of semiconductor devices [8–10].

conductor element such as piezo resistance which is sensitive to deformation, is exposed to these conditions, the weak interfacial adhesion may lead to deviations of the pressure characteristics of the element. Therefore, the encapsulation resin is required to have good adhesion to metals as well as high heat and chemical resistance.

Although the resin-metal interfaces are inevitably exposed to severe environments, they must maintain good adhesion over all conditions. It is predicted that both internal combustion engine-based and electric vehicle will be used until 2030, but there will a shift to more electrification in the future [11, 12]. The control of internal combustion engines will further evolve with regulations, and advanced technologies such as homogeneous-charge compression ignition and fuel reforming that generates hydrogen with exhaust heat will continue to be developed to improve fuel efficiency and clean exhaust gases [13–16]. Moreover, in electrification, the operating voltage and current will exceed 1000 V and several hundreds A from the demand of higher power density, respectively, and the temperature of the electronic devices will likely exceed 170 °C [17, 18]. As described above, the stress applied to the electronic devices will increase and the adhesion inside the devices must be secured even in such conditions.

Since automobiles have a long service life and a wide range of uses, it is necessary to design a reliable system that does not break down. The average replacement age of cars is said to be 11 years, which is known to be longer than electronic devices such as smartphones [19]. In terms of usage, electronic devices in vehicles must not break down over a wide range of service temperature and fuel compositions. For example, in South America, fuels containing a large amount of alcohol are distributed and in developing countries, unpurified gasoline is also used. The differences of the fuel affect the exhaust gas composition, which influences the chemical stress to the bonding interfaces [20]. Thus, it is necessary to identify the failure modes for reliable adhesive bonds, and to do so, it is required to deeply understand the mechanism of adhesion.

General mechanism of adhesion

Although the mechanism of adhesion is still under discussion, three are generally accepted: mechanical bonding, chemical interaction, and mechanical properties of the adhesive itself [21–29]. These three are described below.

Mechanical bonding is also called the anchor effect, in which the adhesive penetrates into pits on the surface of the adherend and the adhesive is captured in the pits. The most typical method to improve the adhesion is by roughening the surface of the adherend. Roughening methods include polishing, shot blast, and chemical etching [30–44]. The size of the roughness depends on the roughening method, which can range from several μm to several nm [45–47]. In order to obtain good adhesion by mechanical bonding, two aspects are most important: the design of the geometric shape and the filling of the resin into the roughened surface. When the size of the roughness becomes nanometer scale, in particular, the resin filling becomes more important since the roughness becomes close to the molecular size of the adhesive.

Another adhesion mechanism is the intermoleclar (chemical) interaction between the adhesive and adherend. When the atoms get closer, they cause chemical interactions such as van der Waals and Coulombic interactions. The reaction may further generate a covalent bond between the two molecules, depending on the combination of molecules. In adhesion by chemical interaction, it is important to form high energy chemical bonds such as hydrogen and covalent bonds in high density between the adhesive and the adherend. Oxidization by plasma or UV is a common approach to generate a carboxyl and a hydroxyl group on the adherend, where the introduction of functional groups into the adhesive can aid bonding [23, 48–50]. In the chemical interaction approach, it is important to improve the wettability of the substrate so that the adhesive is within several tenths of nm of the adherend.

Finally, viscoelasticity of the adhesive is also important. It is known that the energy of rupture of the adherend can be much greater than the work of adhesion calculated from the chemical interactions. This observation indicates that the strength of adhesion cannot be determined only by the interfacial interactions. In addition, depending on the measurement temperature and the peeling speed, the bonded body may have several modes of failure such as bulk fracture, interface fracture, and stick-slip fracture. These experimental results are due to the adhesive being a viscoelastic body. A viscoelastic body is a material that exhibits both elastic and viscous behaviour, and its behavior depends on the deformation rate and temperature. The viscoelastic behavior is, moreover, related to the dynamics of the adhesive molecule at the microscopic picture. Therefore, in analyzing the adhesion mechanism, it is necessary to take into consideration the viscoelasticity of the adhesive itself as well as the interactions at the interface.

Methods for analysis of adhesion and their features

As described above, adhesion is a phenomenon described using interactions at the interface and viscoelasticity. For example, van der Waals interactions are typically described as the Lennard-Jones potential $U_{\mathrm{LJ}}(r)$ and can be expressed as

$$U_{\mathrm{LJ}}(r) = 4\varepsilon\left[\left(\frac{\sigma}{r}\right)^{12} - \left(\frac{\sigma}{r}\right)^{6}\right] \tag{1}$$

where r is the inter-atomic distance, ε and σ are the interaction strength and length, respectively. According to Eq. 1, the interaction energy $U_{\mathrm{LJ}}(r)$ is inversely proportional to the sixth power of the distance, and $U_{\mathrm{LJ}}(r)$ decays quickly and is nearly zero at a few tenths of nm. The electrostatic interaction is commonly expressed as

$$U_{\mathrm{ES}}(r) = \frac{1}{4\pi\varepsilon_0}\frac{q_i q_j}{r} \tag{2}$$

where ε_0 is the dielectric constant of vacuum. $U_{\mathrm{ES}}(r)$ is inversely proportional to the distance and thus extends to a distance farther than the van der Waals force. However, it is still at most about a few nm. Furthermore, it is important that the dynamics of the polymer extend across a wide spatial and temporal scale. A time scale of bond vibration for fast dynamics is the femtosecond scale, and that of translational movement of the center-of-mass extends across the second scale, for example. There are also other modes such as movement of several monomers (segments) and entanglement, and the observed adhesion, in practice, reflects these complex dynamics. At present, there is no method that can simultaneously handle these phenomena with different spatial and temporal scales, and it is important to choose an appropriate method according to the target scale.

In experiments, spectroscopy and microscopy are commonly used for the analysis of the adhesion for a long time. Sum-frequency generation (SFG) spectroscopy is a method that can analyze the molecular vibrational state near the interface by using sum-frequency light generated in the second-order nonlinear optical process, and it can be used to determine the local conformation and the adhesion at the polymer interface. In fact, it has been reported that the π-π interaction between phenyl groups is increased by heat treatment at polystyrene/polystyrene interface. X-ray photoelectron spectroscopy is a method for analyzing atomic composition and its bonding state from the kinetic energy of photoelectrons, and can obtain information in a region several nm deeper than SFG [51–60]. Taking advantage of these methods, the residue at the adherend after peeling was observed and further analyzed at the bonding state of an alumina-PET interface [61]. As a way to evaluate the dynamics, space-resolved fluorescence was conducted for a modified adhesive with a fluorescent tag and the viscoelasticity of a surface was evaluated by an atomic force microscope [57, 62]. These methods are useful, however, they have limitations in terms of experimental setup and spatial or temporal resolution with respect to an adhesive interface. Indeed, these methods were only applicable for an optically transparent or a vacuum interface.

Simulation is also a powerful technique to analyze adhesion, and various methods are being actively developed according to spatial and temporal resolution. The finite element method (FEM) and computational fluid dynamics (CFD) are typical methods for macroscopic simulations. FEM has long been used for the analysis of the stress distribution around the adhesion in the field of structural analysis, and the relationship between the μm level shape and the adhesive strength has been analyzed recently [63–65]. CFD was adopted to simulate the wetting and spreading of liquid adhesives, and recently, the resin filling on the pore with μm has been analyzed [66–69]. Molecular dynamics (MD) simulation and quantum chemical (QM) calculation are of smaller scale than FEM and CFD, and primarily focuses on molecular aggregates and single molecules, respectively. MD simulation is a method that solves the motion of atoms and molecules based on classical mechanics, and analyzes the thermodynamic quantities and peeling process in adhesion [70–73]. QM calculations are based on quantum mechanics, and is the smallest scale simulation. This method is characterized by quantum chemical effects such as chemical reactions and charge transfer between atoms, and is utilized for optimization of the adhesion additive, for example [74–76]. As described above, simulation is also an effective technique for the analysis of the adhesion mechanism, and it is important in the elucidation of the mechanism for use as a complementary technique to the experimental approach.

Analysis of adhesion by MD simulation

Among various simulation methods, ND simulation features direct handling of the atomic structure and dynamics of the adhesive interface, which is difficult to determine experimentally. The analysis of adhesion using MD simulation can be roughly divided into two types: simulation of the thermodynamic quantities by equilibrium simulation, and non-equilibrium simulation of the adhesion and peeling processes. The main target of the thermodynamic quantity in adhesion is the work of adhesion. Work of adhesion W_a is defined as an energy change before and after separating the bonding body and is expressed as

$$W_a = \gamma_A + \gamma_B - \gamma_{AB} \tag{3}$$

where γ_A and γ_B are the surface free energies of the substances A and B, respectively, and γ_{AB} is the interfacial free energy of A-B interface. W_a can be evaluated directly by MD simulation, and treats γ as the internal energy change of each substance. W_a between polyphenylene sulfide (PPS) and epoxy resin is indeed analyzed by MD simulation [77]. It has also been carried out to analyze the change in free energy before and after separation of the adhesive in order to evaluate the adhesion work more precisely [73, 78]. W_a between a polymer brush formed on a substrate and water has been evaluated by thermodynamic integration using an external potential for polymer chains. Non-equilibrium MD is a method of directly adding an external field such as deformation to the adhesion interface as in the experiment. The tensile strength of the adhesive body, for example, can be evaluated from the stress when the adhesive is moved along the normal direction. A variety of simulations were carried out such as peeling adhesive from the silica surface, wetting liquid adhesive to metal-oxides, understanding the effect of the nano-level roughness on the peeling strength, and the influence of the composition of the adherend on the peeling behavior [70–73]. In these Non-equilibrium MD simulation, it was also possible to analyze the local stress distributions from atomic virials, and stress distributions that cannot be simulated by continuum models and experiments.

Although the MD simulations are applied to the adhesion regardless of equilibrium or non-equilibrium, it is not still enough in terms of elucidation of the adhesion mechanism. An open question is the atomic-level picture of the wetting and filling processes of the adhesive corresponding to the real time scale. Indeed, MD analysis of the filling simulation has been performed, however, there is a gap in the time scale. For example, an adhesion test commonly conducted at a few mm/min corresponds to the time scale of 10^{-5} nm/ns and is much slower for MD simulations. In addition, polymers greatly differ in dynamics between the interface and bulk. This difference in dynamics suggests that the viscoelastic properties at the interface will be different from those of the bulk. Even in actual adhesives, it was implied that viscoelastic properties near the interface will affect the strength of adhesion.

Until now, MD simulation has limited its application in terms of spatial and temporal resolution due to computer performance. This limitation, however, has become smaller by computer performance such as many-core CPU, GPUs, and the development of parallelization techniques. Calculations on the order of tens of nm can be routinely performed on large PC clusters. In terms of the dynamics analysis, the MD simulation is also applicable in the order of tens of μs by coarse-graining methods such as coarse-grained molecular dynamics methods and dissipative particle dynamics method [79–81]. In addition, recently, a framework has been developed which uses MD to evaluate the physical quantity of the entire system by decomposing it into specific factors. Tu et al proposed the spatially decomposed formula for the viscosity represented by the Green-Kubo formula with respect to the distance between particles, and analyzing the contribution of the distance between particles to the viscosity for the Lennard-Jones fluid [82]. The spatially decomposed formula is also applied to the electrical conductivity and the solvation free energy [83–85].

Objective and focus of this dissertation

In this dissertion, we aim to understand the adhesion mechanism by molecular simulation, using the filling of epoxy resin into a nano-sized pore, and local viscoelasticity at the resin-metal interface.

Nano-sized pores fabricated on metal surfaces have attracted attention to improve adhesion strength [45–47]. In particular, a dry process such as backward pulsed laser deposition was recently developed to provide good performance at an economical cost. In nano-sized pores, it is desirable to analyze the filling via atomic resolution since the molecular size is close to the pore size. In polymers used for electronic devices, filling and curing may occur simultaneously. An example is transfer molding, where the typical encapsulation process polymerizing while molding simultaneously. These processes increase the degree of polymerization during molding, Thus it is important to analyze the influence of the degree of polymerization to the extent of filling into the pore. Therefore, we have analyzed the filling of epoxy resin into a nano-sized pore, and explored a variety of combinations of the resin and pore sizes to understand a more universal guidelines for efficient filling.

Another objective is the analysis of viscoelastic heterogeneity at the resin-metal interface. The viscoelastic properties of the adhesive itself greatly affect adhesion, but the dynamics of the polymer at the interface is different from that at the bulk. It was experimentally observed that a polystyrene thin film has a glass transition temperature (T_g) lower than that of the bulk at the air interface, and the increase in T_g depends on the interaction strength with the interface. These experimental results imply that the viscoelastic properties at the interface are also different, and expected to be closely related to the adhesion mechanism. In this study, we develop the framework for the analysis of local viscoelasticity by MD simulation, and apply it to the resin-metal interface. The framework is based on the spatially decomposed formula for viscosity proposed by Tu et al.

Organization of this dissertation

In the first chapter, we demonstrate the analysis of resin filling into a nano-sized pore formed on the aluminum surface by all-atom molecular simulation, and analyze the extent of filling for various degrees of oligomerization of the epoxy resin. In Chapter 2, we further explore the concepts of Chapter 1, and examine a variety of combinations of resin and pore sizes to generate a more universal guideline for efficient filling. Atomistic simulation was used to further analyze the relationship between stress distribution at filling. Chapter 3 provides a spatial-decomposition method for relaxation modulus. The spatial-decomposition formula is then applied to the planar interface between the resin and metal by using the Kremer-Grest model at a variety of adhesion strengths, which helps to reveal the relationship of the adhesive to the viscoelastic inhomogeneity in the segment-scale space and time.

Chapter 1

MD Simulation Analysis of Resin Filling into Nano-Sized Pore Formed on Metal Surface

1.1 Introduction

Resin-metal interface is nowadays prevalent in integrated circuits and sensing devices equipped with automobile [4, 5]. A requirement for their stable operations is then that resin and metal be tightly adhered. A common scheme for improving the adhesion strength is to roughen the resin-metal interface by shot-blast or chemical etching [30–44], and the roughening technique has recently exploits pores sized-down to nanometer scale [45–47]. In a nano-sized pore, atomic details of resin-metal interactions play key roles in determining the extent and rate of resin filling into the pore. It is thus desirable to explore the resin-metal interaction in and around a nano-sized pore at atomic resolution.

To analyze the filling of resin into a nano-sized pore, a technique with high-spatial resolution needs to be employed. TEM (transmission electron microscope) and AFM (atomic force microscope) have nanometer resolutions, though the dynamics of filing is still difficult to approach [86–88]. Spectroscopic techniques can detect the dynamics, on the other hand, while the spatial resolution is not yet at nanometer scale [86, 89, 90]. Molecular dynamics simulation (MD) is an alternative for overcoming the limitations of spatial and time resolutions. When the force field is appropriately modeled, the atomic-level pictures can be obtained at pico- to nanosecond time scale [91–98]. Indeed, all-atom MD was conducted to analyze nano imprint lithography [99–102], and a coarse-grained method was further developed to extend the time scale of computation [103–106].

In the present work, we analyze the filling of epoxy resin into nano-sized pore formed on aluminum surface by all-atom MD. Our particular focus is the effect of the degree of oligomerization of resin. Indeed, the structural and viscoelastic properties of a resin is controlled by the degree of oligomerization and its size may need particular attention in the analysis of the interaction with metal when the pore is of nanometer scale and is comparable in dimension to the resin. In our simulations, the pore radius was set to 2.5 nm and the resin radius (of gyration) was varied from 0.5 to 2.5 nm. A typical observation in practice is that the filling efficiency of a resin can be improved by tuning its size [34], though the molecular mechanism is still to be sought for rational design of filling procedure. It is thus important to analyze the effect of the degree of resin oligomerization on the filling behavior with regard to the relationship between the resin and pore sizes. The filling of resin into pore is achieved by pushing the former. An experimental rate of pushing is typically 0.1-1.0 m/s as a semi-quantitative estimate, and this converts to 1-10 ns per nm of the pore depth when the resin is pushed at uniform rate. In the present work, the pushing MD is conducted at a rate comparable to the experimental. It will then be observed that the control of resin size is important for efficient filling of the pore.

1.2 Simulation model and method

Two kinds of resin were examined in the present work. One is polyphenol (PH) mixed with polyglycidylether of *o*-cresol formaldehyde novolac (EP), and the other is oligomers formed through ring-opening reactions of EP and PH. The chemical structures and the properties of the resin models are shown in Fig. 1.1 and Table 1.1. The oligomer was constructed by combining the terminal groups of EP and PH alternately, and will be called OL_n according to their degree of oligomerization n. The metal side was modeled with aluminum of face-centered-cubic (fcc) structure. The interface was treated as the (001) plane, and a cylindrical pore of a radius of 2.5 nm and a depth of 7.0 nm was located on the upper side. The overview of the simulation model is depicted in Fig. 1.2.

The force field employed was Dreiding for the resins, and the embedded atom method (EAM)

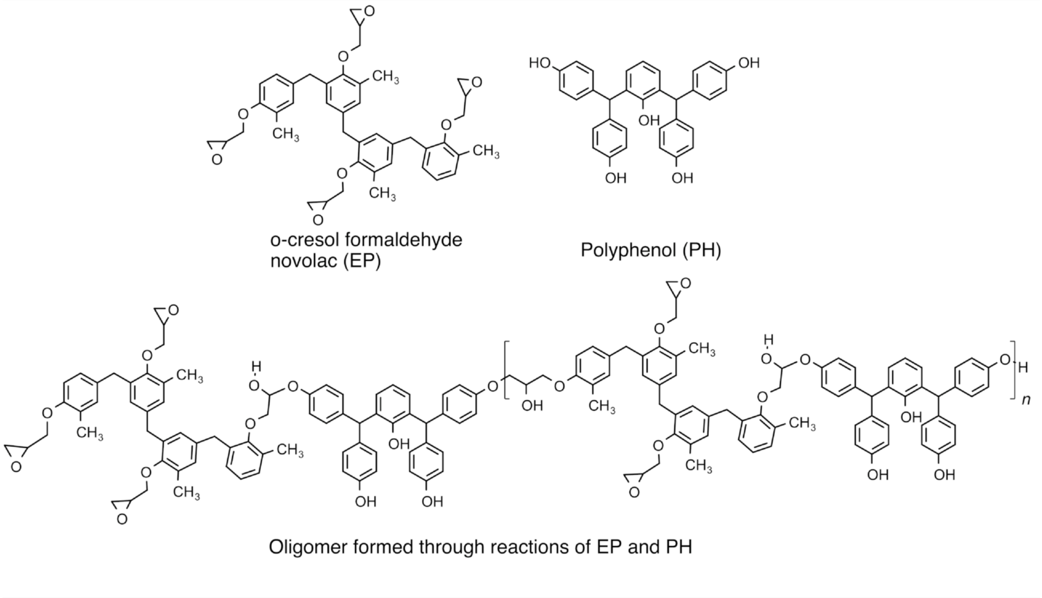

Figure 1.1: Chemical structures of the resin models

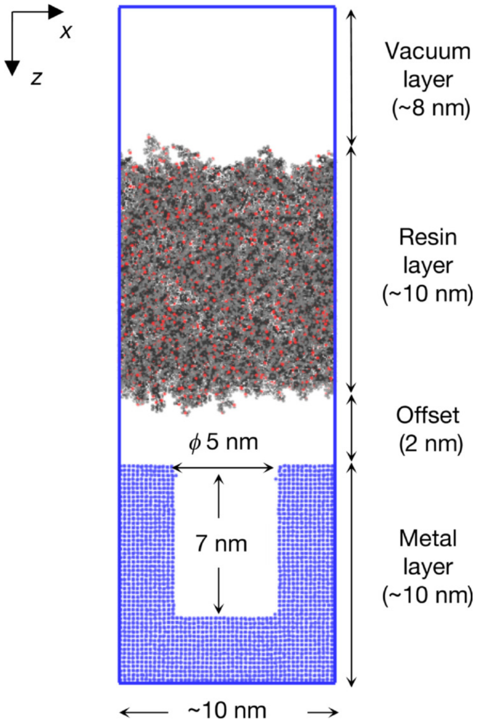

Figure 1.2: Overview of the simulation model

Table 1.1: Properties of the resin models

Species	n	Molecular weight [g/mol]
EP	-	692
PH	-	490
OL_0	0	1182
OL_1	1	2364
OL_7	7	9456

parametrized by Jacobson was adopted for aluminum [91–93, 95]. They have been adopted commonly in simulations of epoxy resin and metal [107–116]. The resin-aluminum interaction was then of Lennard-Jones (LJ) 12-6 form, and all the LJ energy and length parameters were taken from Dreiding with Lorentz-Berthelot combining rule. It has been actually seen that the LJ 12-6 potential describes the resin-metal interaction effectively, with calculated results in agreement with experiments for such properties as surface tension, interfacial tension, and contact angle [94, 97, 102, 117–123].

The partial charges on the atoms in the resins were determined by the RESP procedure [124, 125]. Quantum-chemical calculations were conducted for the monomers of EP and PH and for three fragments of the oligomers shown in Fig. 1.3. Gaussian 09 was employed at B3LYP/6-31G(d,p) level in vacuum with geometry optimization [126], and the partial charges on EP and PH were assigned with the constraint that the total charges of the molecules are zero. The charges in the oligomer OL_n was determined through three steps. In the first step, the charges on the fragments of Fig. 1.3 were computed with the constraint of zero, total charge. In the second step, the charges on the fragments were transferred to the oligomers with the convention of color matching in Fig. 1.3; note that the red part is generated by the ring-opening reaction of EP and PH. The third step was to shift the charges in the second step uniformly so that the total charge of OL_n vanishes.

Each MD simulation was carried out using LAMMPS version 14May16 with the velocity Verlet integrator at a time step of 0.5 fs without any constraints on the molecular structures [127, 128]. The electrostatic interaction was handled by the particle-particle particle-mesh (PPPM) method [129, 130] implemented in LAMMPS with a root mean square force accuracy of 10^{-4}. The pair interaction was truncated at 1.0 nm on atom-atom basis both for the real-space part of PPPM and

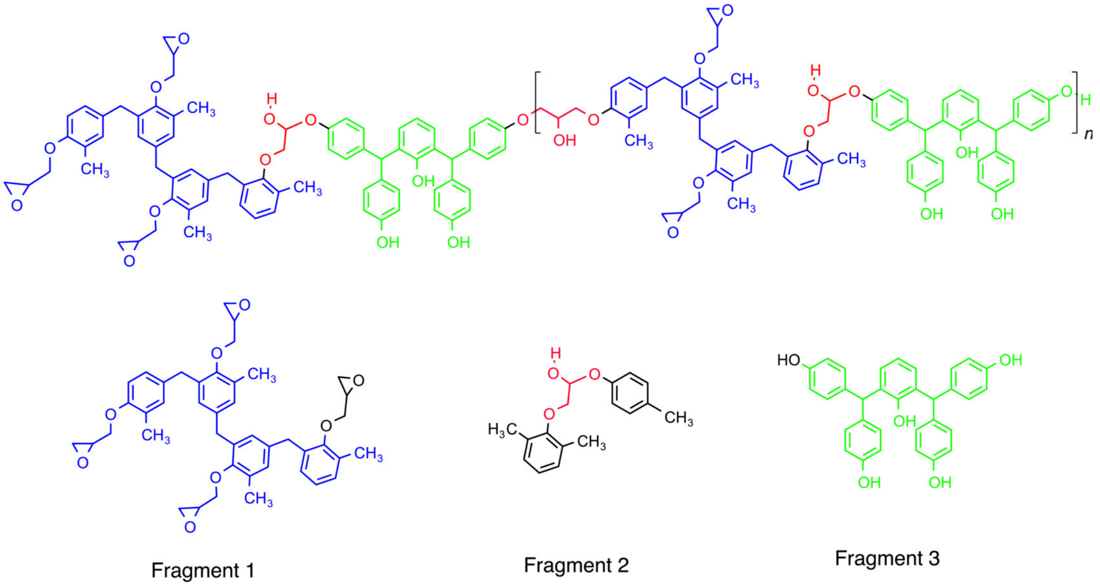
Fragment 1

Fragment 2

Fragment 3

Figure 1.3: Fragment models for determining the atomic charges in the oligomers

for LJ, and the LJ long-range correction was not included. The periodic boundary condition was adopted with minimum image convention, and the numbers of resin molecules in the MD unit cell are listed in Table 1.2. In all the MD simulations, the temperature and pressure were regulated with the Nosé-Hoover thermostat and barostat at coupling constants of 1.0 ps [131–134].

Before simulating the resin-aluminum system, aluminum and resin layers were separately prepared. To set up the aluminum layer, a cubic crystal of fcc form with an edge length of 10 nm was built with (001) plane facing upward to the positive z direction, and the pore was introduced by removing the atoms in the cylindrical region with a radius of 2.5 nm and a depth of 7.0 nm from the crystal surface. A vacuum layer of 2.0 nm was then located above the aluminum region, and the aluminum system was subject to MD over 1 ns in the *NPT* ensemble at 450 K and 1 atm. This was done to relax the aluminum configuration around the pore. A layer of resin molecules was then made by placing them in a rectangular unit cell. The edge lengths of the resin layer along the x and y directions were taken to be the same as those of the aluminum layer, and the z length was adjusted so that the density of the layer is identical to the bulk density of the resin shown in Table 1.2. To relax the resin layer, an MD was done in the *NVT* ensemble at 1000 K for 50 ps, followed by one at 450 K for 500 ps. Finally, the initial configuration of MD was built by combining the resin

Table 1.2: Composition of the resin in the MD unit cell

Entry	Number of molecules					Bulk density [g/cm^3]
	EP	PH	OL$_0$	OL$_1$	OL$_7$	
1	500	500				0.975
2			500			1.042
3				250		1.054
4					60	1.002

and metal layers to the form of Fig. 1.2, using Winmostar package and adding a vacuum region of 8.0 nm thickness above the resin layer [135]. This vacuum region was introduced to prevent the contact between the top part of the resin layer and the bottom of the metal layer due to the periodic boundary condition, and the resin and metal layers forms an interface spanning along the *x* and *y* directions.

We now describe the scheme of filling. In the following, the top 2.0-nm region of the resin layer and the bottom 2.0-nm region of the metal layer are called resin wall and metal wall, respectively. The filling was done by 800 steps. At each step, the atoms belonging to the resin was pushed downward instantaneously over 0.01 nm and the whole system was energy-minimized and further simulated with MD over 20 ps in the *NVT* ensemble at 450 K; the first 10 ps was for equilibration and the latter 10 ps was for production. The energy minimization and MD at each step of filing was done by restraining the atoms in the resin wall to their positions right after the pushing; the restraint is a harmonic potential with a force constant of 10^4 kcal/mol/Å^2 and is applied only to those atoms contained in the resin-wall region which is distant from the resin-metal interface. The atoms in the metal wall were also restrained to their initial positions throughout the entire simulation with the same harmonic potential. It should be noted that the metal layer was restrained only for the wall part. This "partial" scheme of restraining was adopted to allow the deformation of the upper part of the metal layer, and is in contrast to the schemes in previous studies where the whole layer of metal was restrained [99–102]. The pushing over 0.01 nm at an interval of 20 ps corresponds to a filling rate of 0.5 m/s, and is actually comparable to the rate commonly used in reality. In the present calculations, the above scheme of pushing was done 3 times, and the averages of the 3 independent runs are presented in the following.

1.3 Results and discussion

As noted at the end of the previous section, the resin was filled into the pore through 800 steps of 0.01-nm displacement. As shown in Fig. 1.2, the "bottom" of the resin and the "top" of the pore were initially separated by 2 nm, and in the following, we describe the position of the resin region at the *n*-th step of the displacement using the value *d* defined as

$$d = 2 - 0.01n. \tag{1.1}$$

Note that the distance between the "bottom" of the resin region and the "top" of the pore region cannot be precisely specified due to the flexibility of the resin. At large *n*, in particular, *d* may not refer to the separation of the two regions since the resin and/or pore can be deformed. We employ *d* only as an index for the progress of pushing.

In the following, we often discuss the effect of the degree of oligomerizaiton in terms of the resin size. The radius of gyration (R_g) is a common measure to express the size and is written as

$$R_g = \langle \frac{1}{M} \sum_j m_j (\mathbf{r}_j - \mathbf{r}_{\mathrm{com}})^2 \rangle_{d=2} \tag{1.2}$$

where M and $\mathbf{r}_{\mathrm{com}}$ are the molecular weight and the center-of-mass coordinate of a resin molecule, respectively, m_j and $\mathbf{r}_j$ are the mass and the coordinate of the j-th atom within the resin molecule, respectively, and $\langle \cdots \rangle_{d=2}$ refers to the average over all the resin molecules in the 10-ps production at the initial stage of the pushing ($d = 2$). For the resins treated in the present work, R_g is 0.51, 0.87, 1.51, and 2.47 nm for entries 1-4 of Table 1.2, respectively.

Fig. 1.4 illustrates snapshot configurations at $d = 2$, -3, -4, -5, and -6 (corresponding to n = 0, 500, 600, 700, and 800, respectively) at the end of the 20-ps MD at fixed d. It is evident that the pore is filled earlier (at larger d) when the resin is smaller. Entry 1 of Table 1.2 is the smallest among the resins studied in the present work and fills the pore at $d \simeq -4$. Pushing effort for filling the pore increaces with the degree of oligomerization, and the metal pore is further observed to deform with the large resins (entries 3 and 4). A small resin can thus be introduced easily into the nano-sized pore, and a large one needs more efforts of pushing and accompanies the shrinkage of the pore.

As described above, the metal pore deforms with introduction of the resin. The deformation can then be addressed in terms of the root mean square displacement (RMSD) of the Al atoms adjacent to the pore, which is written as

$$\mathrm{RMSD} = \left\langle \sqrt{\frac{1}{N}\sum_{i=1}^{N}(\mathbf{r}_{i,d} - \mathbf{r}_{i,2})^2} \right\rangle \tag{1.3}$$

where $\mathbf{r}_{i,d}$ is the coordinate of the i-th Al atom at the step specified by d of Eq. (1.1), $\mathbf{r}_{i,2}$ refers to its initial value ($d = 2$; see Eq. (1.1)), the sum is taken over the atoms which are located within 0.5 nm from the surface of the pore at time 0 ($d = 2$), N is the number of such atoms, and the average $\langle \cdots \rangle$ is taken over the 10-ps productions at fixed d of the 3 independent runs. In Fig. 1.5, we show the RMSD as a function of d. It is evident that the deformation of the pore is the weakest for entry 1. In this case, RMSD is essentially unchanged till $d \simeq -4$. The deformation is appreciable at larger d (more separated resin and metal) for the entries with larger degree of oligomerization. For example, it is at $d \simeq -3$ when RMSD for entries 2, 3, and 4 reach the value at $d = -5$ for entry 1. In fact, the metal pore can deform when a high pressure is applied. In other words, the region of d without appreciable deformation is the practically available one in resin pushing, and in the following, we restrict our analysis to $d > d_{\mathrm{min}}$ with $d_{\mathrm{min}} = -5$ for entry 1 and $d_{\mathrm{min}} = -4$ for the others.

The extent of filling can be quantified by the density of the resin in the pore defined as

$$\rho_{\mathrm{pore}} = \langle \frac{1}{V_{\mathrm{pore}}} \sum_i m_{i,\mathrm{pore}} \rangle \tag{1.4}$$

where V_{pore} is the volume of the cylindrical-pore region with a radius of 2.5 nm and a depth of

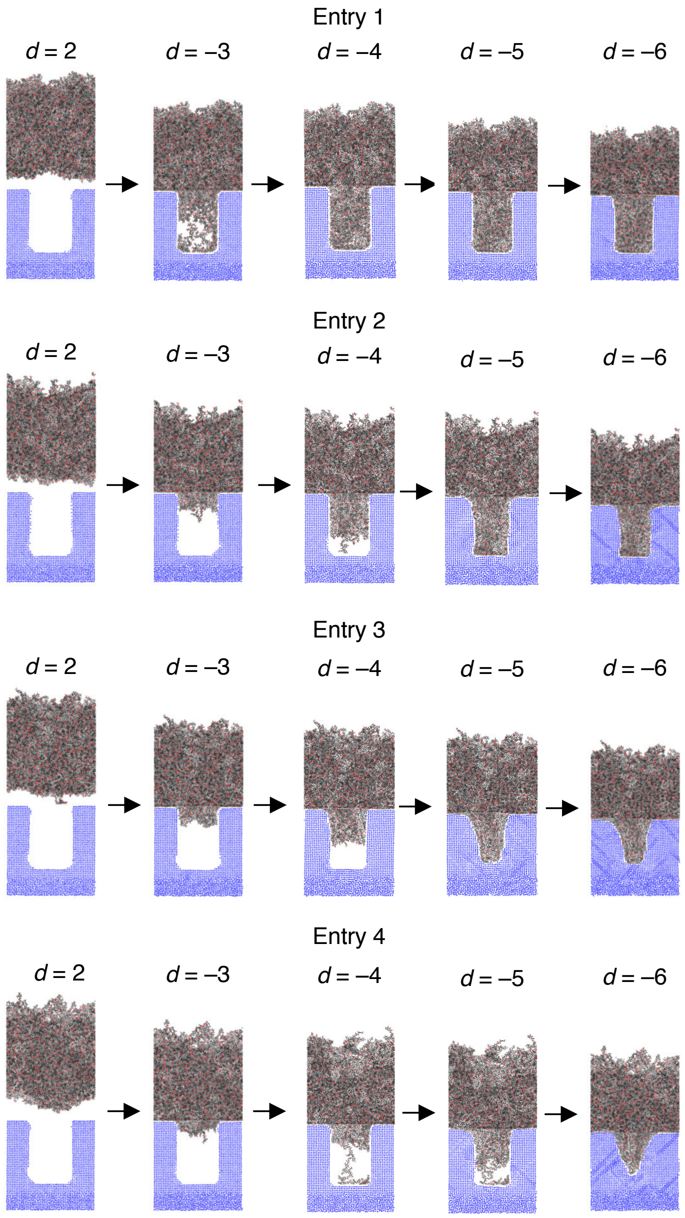

Figure 1.4: Snapshot configurations of the resin-metal systems. See Table 1.2 for the entry of the resin and Eq. (1.1) for the definition of *d*.

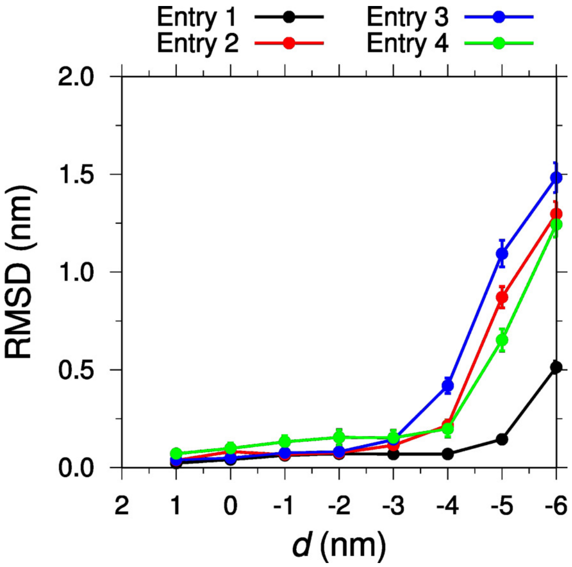

Figure 1.5: RMSD of the Al atoms which are located on the pore surface at time 0 ($d = 2$), plotted against the pushing distance d defined by Eq. (1.1).

7.0 nm, $m_{i,\mathrm{pore}}$ is the mass of the i-th atom of resin contained in the pore region, and the average $\langle\cdots\rangle$ is taken over the 10-ps productions at fixed d of the 3 independent runs. Fig. 1.6 shows the density thus defined. As a reference, the resin density in the bulk is listed in Table 1.2 and is $\sim$1.0 $\mathrm{g/cm^3}$ for all the entries. According to Fig. 1.6, the density in the pore increases monotonically with the pushing (decrease of d). For the smallest resin (entry 1), the density reaches the bulk value at $d \simeq -5$. This indicates for entry 1 that the pore inside becomes well filled through pushing of the resin. The extent of filling expressed as the density is smaller for the other entries with larger degree of oligomerizaion. The density is only $\sim$0.3 $\mathrm{g/cm^3}$ at d_{min} for the largest degree of oligomerization (entry 4), and the pore inside is not filled with the resin when the pore is not deformed.

To see the process of penetration in more details, the density map of resin in and around the pore was analyzed as a function of the pushing distance d. To compute the density map, a set of small cells were defined in the simulation box with linear bins of $\Delta z = 0.2$ nm along the vertical direction (z direction in Fig. 1.2) and concentric bins of $\Delta r = 0.2$ nm over the lateral directions; the concentric bins were employed since the system examined is of cylindrical symmetry. The density

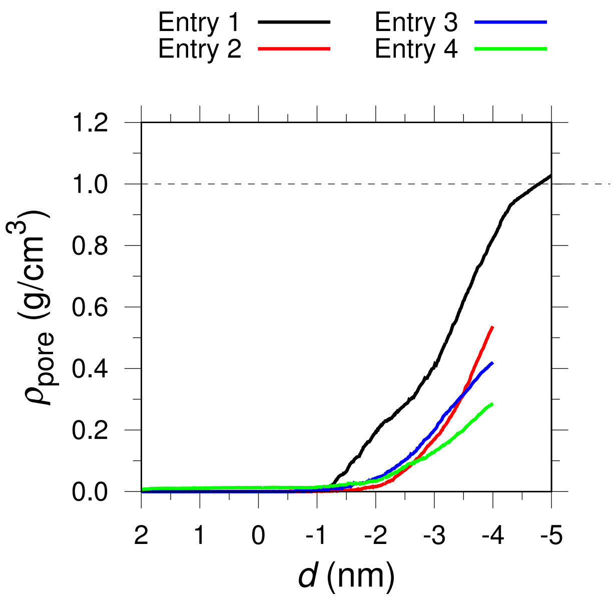

Figure 1.6: Evolution of the density in the pore ρ_{pore} against the pushing distance d. See Table 1.2 for the entry of the resin and Eqs. (1.1) and (1.4) for the definitions of d and ρ_{pore}, respectively. The dotted line refers to the bulk density of the resin listed in Table 1.2.

within each cell was then calculated through

$$\rho_{\mathrm{cell}} = \langle \frac{1}{V_{\mathrm{cell}}} \sum_i m_{i,\mathrm{cell}} \rangle \tag{1.5}$$

where V_{cell} is the volume of the small cell, $m_{i,\mathrm{cell}}$ denotes the mass of the i-th atoms contained in the cell, the metal atoms were not counted in the sum, and the average $\langle \cdots \rangle$ was taken over the 10-ps productions at fixed d of the 3 independent runs. Fig. 1.7 shows the density map at a variety of d. For entry 1, it is seen that the resin penetrates into the pore along the wall at the early stage ($d \gtrsim -2$). The penetration then proceeds preferentially near the wall and the filling is completed at $d \simeq -5$. For the other entries, the resin moves rather uniformly with respect to the radial distance along the lateral directions of the cylindrical pore. The contrast due to the resin size reflects the competition between the resin-metal and resin-resin interactions. The metal surface can be wet by resin since the former generally has higher surface free energy than the latter [136, 137], and this leads to the adhesion of the small resin (entry 1) on the metal wall. The resin-resin interaction is strengthened with the degree of oligomerization, on the other hand. The role of resin-metal interaction then reduces relatively for the larger resins, and the filling proceeds uniformly in the pore.

To examine the extent of filling in terms of the resin size, Fig. 1.8 shows the correlation of the radius of gyration R_g introduced by Eq. (1.2) against the maximum density in the pore $\rho_{\text{pore}}^{\text{max}}$ achieved at $d = d_{\text{min}}$. It is evident that $\rho_{\text{pore}}^{\text{max}}$ reduces with R_g, as inferred from the arguments presented above. According to Fig. 1.8, $\rho_{\text{pore}}^{\text{max}}$ reaches half the bulk density for entries 1 and 2, which have R_g smaller than half the pore radius. It is to be noted that $R_g < R_p$ for all the resins examined, where R_p is the pore radius. The half filling of the pore is achieved only when $R_g < R_p/2$. This indicates that the efficient filling of the pore is inhibited by the associative interaction among the resin molecules.

1.4 Conclusion

All-atom MD simulation was conducted for the filling of epoxy resin into a nano-sized pore formed on aluminum surface. The resin species examined were polyphenol mixed with polyglycidylether of *o*-cresol formaldehyde novolac and their oligomers formed through ring-opening reactions. The degree of oligomerization was then varied from 0.5 to 2.5 nm with respect to the radius of gyration, and the radius of the cylindrical pore was fixed at 2.5 nm. The filling was simulated by preparing a layer of amorphous resin above an aluminum surface with a nano-sized pore. The resin was pushed into the pore at a rate comparable to the one commonly employed in reality, and it was seen that the penetration into the pore proceeds along the wall for small resin and rather uniformly in the pore for larger ones. The maximum density achieved with pushing was found to be larger when the resin is smaller. When the radius of gyration of the resin is larger than half the pore radius, the resin density in the pore does not reach half the bulk density of the resin without deformation of the pore. It is therefore implied that the resin-resin interaction inhibits the filling of a nano-sized pore. A rational guideline for improving the filling efficiency is then to reduce the relative strength of the

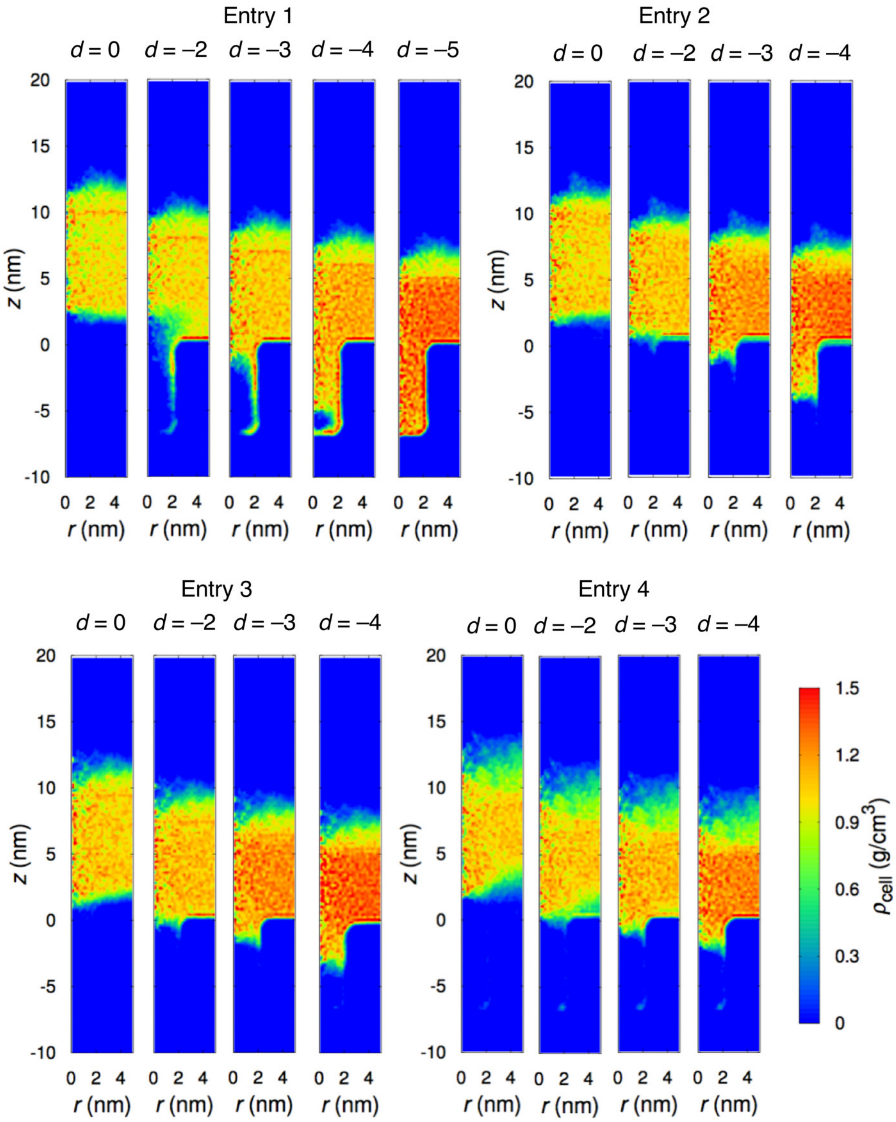

Figure 1.7: Density map of resin, where z is the coordinate along the direction of depth of the cylindrical pore (z direction in Fig. 1.2) and r is the radial distance over the lateral directions from the center of the cylinder. $z = 0$ is taken to be the "top" position of the pore before the pushing starts ($d = 2$ in Eq. (1.1)). See Table 1.2 for the entry of the resin.

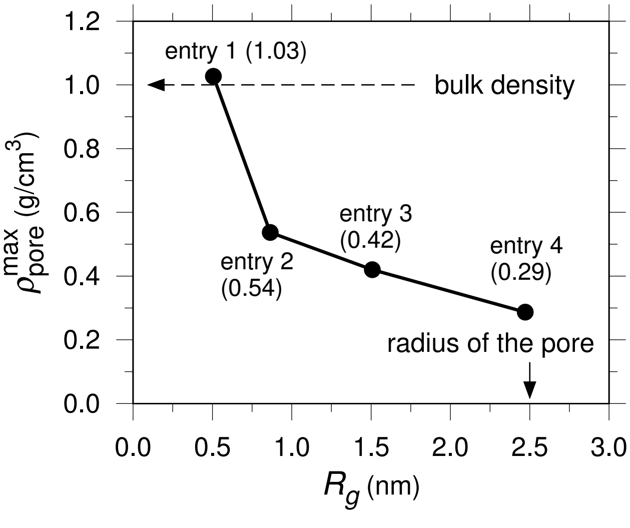

Figure 1.8: Relationship between R_g and the maximum density in the pore $\rho_{\text{pore}}^{\text{max}}$, where $\rho_{\text{pore}}^{\text{max}}$ is the maximum value of the ρ_{pore} in Fig. 1.6 and its value shown in the parenthesis. See Eq. (1.2) for the definition of R_g.

resin-resin interaction to the resin-metal. In subsequent work, we vary the metal species, resin size, and pore size toward further support and refinement of the guideline.

Chapter 2

Resin Filling into Nano-Sized Pore on Metal Surface Analyzed by All-Atom Molecular Dynamics Simulation over a Variety of Resin and Pore Sizes

2.1 Introduction

Adhesion between resin and metal is widely used in electronic devices for automobile [4, 5]. Indeed, multi-material methods involving an organic/inorganic interface are under active development, and guidelines are sought for improving the strength of adhesion. The roughening of the metal surface is an efficient scheme for better adhesion [30–44]. The number of interaction sites between resin and metal increases with use of a rough surface, and can enhance further with introduction of nano-sized pores onto the surface [45–47]. The resin-metal interface with nano-sized pore is thus an emerging technology for multi-material adhesion, with a key factor being the extent of filling of resin into the pore [138]. Actually, a nano-scale filling may be strongly affected by the sizes of resin and pore and the resin-metal interaction at atomic resolution [139]. Its mechanism can be revealed through methodologies with high spatial and/or temporal resolution.

The spatial resolution at nanometer scale is achieved by TEM (transmission electron microscopy) and AFM (atomic force microscopy). They can show atom-specific densities at an interface, though it is still difficult to probe the dynamics of filling [86–88]. Spectroscopic methods can detect the dynamics, on the other hand, while the nano-scale resolution is not commonly available in space [86, 89, 90]. All-atom molecular dynamics simulation (MD) is an alternative method for investigating an atomic-level process at nanometer and nanosecond resolution. It can provide faithful pictures when the force field is appropriately set, and has been indeed employed to analyze the filling process including nanoimprint lithography [68, 71, 99–102, 139, 140].

In a previous work, we conducted MD simulation to analyze the filling of resins into a nano-sized pore on aluminum, with the purpose of finding a guideline for efficient filling [139]. The resins examined were the mixture of polyphenol (PH) and polyglycidylether of *o*-cresol formaldehyde novolac (EP) and a set of oligomers of EP and PH with varied extent of oligomerization. They are commonly employed as thermosets in manufacturing of electronic devices. The typical temperature for curing the thermosets is 450 K, at which EP and PH are fed as raw materials and oligomerize in the manufacturing process. EP, PH, and their oligomers then stay melted and the resin is more viscous with the degree of oligomerization [5, 141–143]. The MD in Ref. 139 was done at 450 K, and a main finding was that when the radius of gyration of the resin is less than half the radius of the pore, the half filling of the pore is achieved at commonly employed speed of pushing the resin toward the metal. A single size was examined for the pore, however, since the major purpose of the previous study was to establish the computational setups; all-atom MD is still not prevalent for resin-metal interface with nano-sized pores.

In the present work, we examine a variety of combinations of the resin and pore sizes to explore a more universal guideline of efficient filling. The pore radius was fixed at 2.5 nm in Ref. 139, that corresponds to the smallest available in reality. The radius is varied between 2.0 and 7.5 nm in this work, on the other hand, reflecting the range commonly employed in manufacturing. It will be shown that the resin is efficiently filled when its size is smaller than of the pore by an order of magnitude.

A pressure is applied to push the resin into the pore, typically at several tens of MPa in practice. The manufacturing system is usually set so that the pushing stops beyond 100 MPa. In the present work, we monitor the pressure as a function of the extent of filling. This is done to keep closer correspondence between computation and experiment, and a guideline for efficient filling needs to be formulated within practically used range of pressure. It will be observed that the pressure becomes high at earlier stages of filling when the resin is larger.

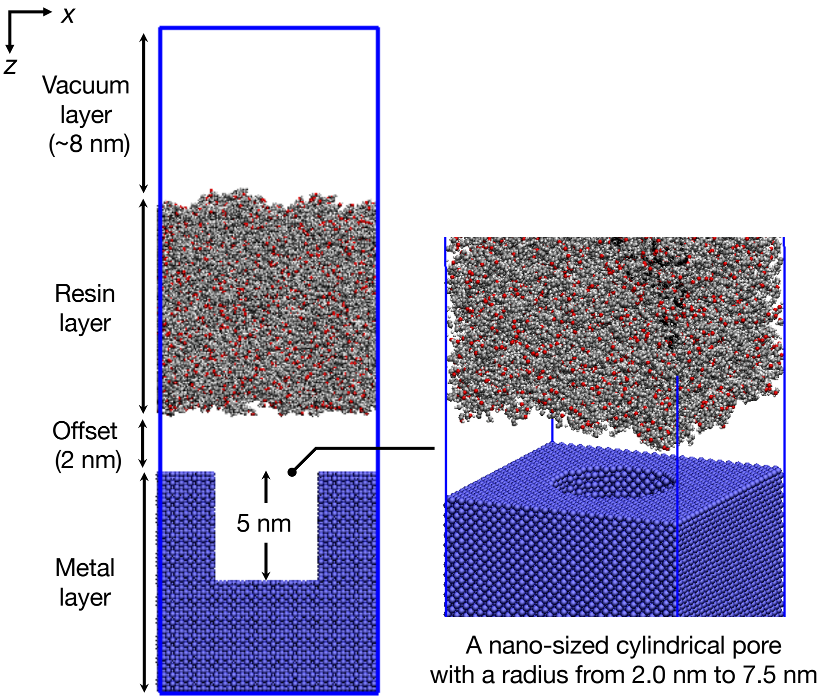

Figure 2.1: Overview of the simulation model

2.2 Simulation model and method

In the present work, two kinds of resin systems were examined. One is the mixture of polyphenol (PH) and polyglycidylether of *o*-cresol formaldehyde novolac (EP), and the other is a set of oligomers formed through ring-opening reactions between EP and PH. The oligomer is called OL_n according to its degree of oligomerization n, that was constructed by connecting the terminal groups of EP and PH alternately. Aluminum of face-centered-cubic (fcc) structure was used as the metal, with the (001) plane as the interface. A cylindrical pore with a radius described below was located on the upper side of the metal, and Fig. 2.1 shows the overview of the simulation model.

Dreiding was adopted as the force field for the resins, and the modified embedded atom method (MEAM) was used for alumiunm as parametrized by Pascuet [93, 144, 145]. These force fields have been commonly employed in simulations of epoxy resin and metal [96, 98, 112–116]. The parameters for resin-aluminum interaction were taken from Heinz *et al* [97]. They are suitable for the simulation of resin-metal interface, as reported for such properties as surface tension, interfacial tension, and contact angle [94, 118, 120–123]. All the Lenard-Jones (LJ) energy and length parameters were subject to the Lorentz-Berthelot combining rule.

The atomic charges in the resins were determined by ab initio quantum-chemical (QM) treatment using Gaussian09 program package [126]. QM calculations were conducted at the B3LYP level with the 6-31G(d,p) basis set for the monomers of EP and PH and for the three fragments of the oligomers shown in Fig. 2.2. The geometry optimization was done in vacuum, and the atomic charges were specified by the restrained electrostatic potential (RESP) procedure [124, 125], with the constraint that the total charge of each QM system is zero. The charges in the oligomer OL_n was derived as follows. The charges on the fragments of Fig. 2.2 were transferred to the oligomers with the convention of color matching in Fig. 2.2; it should be noted that the red part comes from the ring-opening reaction of EP and PH. All the charges thus assigned were then shifted uniformly so that the total charge of OL_n vanishes.

All the MD simulations were conducted using LAMMPS version 14May16 [128]. In the present work, MD was performed both for building the simulation cell and for the resin filling into the aluminum pore, with the SHAKE constraints for all the bond lengths with hydrogen [146]. To build the cell, the velocity Verlet integrator was employed at a time step of 0.5 fs [127], and the temperature and pressure were regulated with the Nosé-Hoover thermostat and barostat at coupling constants of 1.0 ps and 2.0 ps, respectively [131–134]. In the filling process, the Langevin dynamics was conducted in the *NVT* ensemble at 0.5 fs with an inverse friction constant of 1.0 ps for temperature control [147, 148]. The particle-particle particle-mesh (PPPM) method was used to handle the electrostatic interaction at a root mean square force accuracy of 10^{-4}. The truncation was applied to pair interactions on atom-atom basis both for the real-space part of PPPM and for LJ. The LJ long-range correction was not incorporated, and the periodic boundary condition was employed with minimum image convention.

The simulation cell was built in the following scheme. First, aluminum and resin layers were separately prepared. A cubic crystal of fcc form was set up with the (001) plane facing upward to the positive z direction, and the pore was introduced by removing the atoms in the cylindrical region

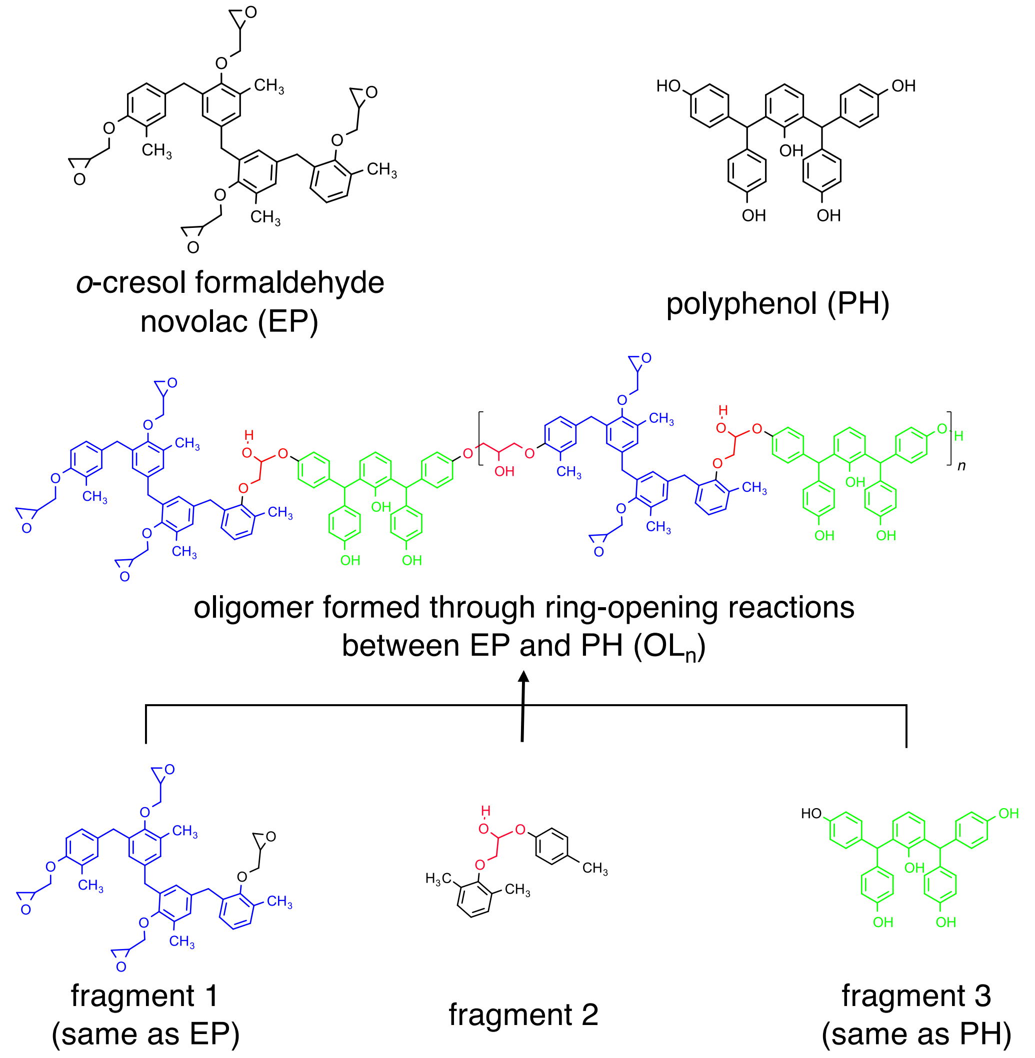

Figure 2.2: Fragment models for determining the atomic charges in the oligomers

with the radius (R_p) given next at a depth of 5.0 nm from the crystal surface. The edge lengths along the x and y directions were taken to be 10 nm when $R_\mathrm{p} = 2.0$ and 2.5 nm, and they were 20 nm for $R_\mathrm{p} = 5.0$ and 7.5 nm. A vacuum layer of 2.0 nm was then placed above the aluminum region, followed by the energy minimization. A layer of resin molecules was prepared by locating them in a rectangular unit cell with the numbers of EP, PH, and the oligomers listed in Table 2.1. The initial density was very low ($\sim 0.001 \mathrm{g/cm^3}$) in a cubic unit cell, and the system was subject to MD over 100 ps in the *NVT* ensemble at 450 K. In this process, the x and y lengths of the unit cell was gradually modified so that they are 80% of those of aluminum layer at the end of the 100-ps MD, with the z length decreased correspondingly to 8 nm. After that, 50-ps MD was conducted at the cell length fixed. A similar process followed with a 500-ps MD at 450 K to match the x and y lengths to those for aluminum, where the z length was set to keep the volume of the unit cell constant. The resin system was then treated through the steps in Table 2.2. This preparation procedure was proposed by Hoffman; it is an efficient scheme of equilibration for an amorphous polymer [149, 150]. After the aluminum and resin layers were made, the initial configuration of MD was built by combining them in the form of Fig. 2.1, with a vacuum region of 8.0 nm thickness further above the resin layer. This vacuum region was introduced to prevent the contact between the top part of the resin layer and the bottom of the metal due to the periodic boundary condition. The resin and metal layers forms an interface spanning along the x and y directions, and the number of the molecule in the unit cell and the geometry of the pore are listed in Table 2.1.

With the resin-metal system built as above, the resin was filled into the pore by repeating the following procedure. The resin atoms were first pushed downward to the metal side by 0.01 nm. The whole system was then energy-minimized and was subject to a 20-ps MD at 450 K. The atoms in the top 2.0-nm region of the resin layer and all the metal atoms were restrained to their positions right after the pushing, and the restraint was a harmonic potential with a force constant of 10^4 kcal/mol/Å^2. In the MD, the first 10 ps was for equilibration and the latter half was for production. The above procedure was repeated for 700 times. Note that the pushing with 0.01 nm every 20 ps converts to a filling rate of 0.5 m/s, and this corresponds to the common rate in reality. To describe

Table 2.1: Pore geometry and composition of the resin in the MD unit cell. The value in parenthesis at the column of Composition is the number of resin molecules in the MD unit cell. The radius of gyration (R_g) is defined by Eq. (2.2), and R_g and R_p are expressed in nm. The entry ID is shown for each combination of R_g and R_p with their ratio in the bracket.

Entry $[R_\mathrm{g}/R_\mathrm{p}]$	Resin layer				
	Composition	EP (500), PH (500)	OL_0 (500)	OL_1 (250)	OL_7 (60)
Metal layer	R_p \ R_g	0.5	0.9	1.5	2.5
	2.0	1-1 [0.25]	1-2 [0.45]	1-3 [0.75]	1-4 [1.25]
	2.5	2-1 [0.20]	2-2 [0.36]	2-3 [0.60]	2-4 [1.00]
	5.0	3-1 [0.10]	3-2 [0.18]	3-3 [0.30]	3-4 [0.50]
	7.5	4-1 [0.07]	4-2 [0.12]	4-3 [0.20]	4-4 [0.33]

Table 2.2: Equilibration step for the resin system.

Step	Simulation conditions			
	Ensemble	Temperature (K)	Pressure (atm)	Time (ps)
1	*NVT*	600	-	50
2	*NVT*	450	-	50
3	*NPT*	450	1000	50
4	*NVT*	600	-	50
5	*NVT*	450	-	100
6	*NPT*	450	30000	50
7	*NVT*	600	-	50
8	*NVT*	450	-	100
9	*NPT*	450	5000	50
10	*NVT*	600	-	50
11	*NVT*	450	-	100
12	*NPT*	450	1	1000

the progress of filling, in the following we employ the index d defined as

$$d = 2 - 0.01n \tag{2.1}$$

at the n-th step of pushing. The size of resin will be further analyzed in terms of the radius of gyration written as

$$R_{\mathrm{g}} = \langle \frac{1}{M} \sum_j m_j (\mathbf{r}_j - \mathbf{r}_{\mathrm{com}})^2 \rangle_{d=2} \tag{2.2}$$

where M and $\mathbf{r}_{\mathrm{com}}$ are the molecular weight and the center-of-mass coordinate of a resin molecule, respectively, m_j and $\mathbf{r}_j$ are the mass and the coordinate of the j-th atom within the resin molecule, respectively, and $\langle \cdots \rangle_{d=2}$ refers to the average over all the resin molecules in the 10-ps production at the initial stage of the pushing ($d = 2$). The pushing simulation was done three times for each of the entries in Table 2.1, and the averages of the three independent runs will be presented.

2.3 Results and discussion

The resin was filled into the pore by applying the pressure. In reality, the pushing pressure is typically at several tens of MPa and up to 100 MPa. In the present work, the pressure P_{push} was defined from the zz component of the stress tensor σ^{zz} and was evaluated as

$$P_{\mathrm{push}} = -\frac{\langle \sigma^{zz} \rangle_d}{V_{\mathrm{resin}}} \tag{2.3}$$

where $\langle \cdots \rangle_d$ refers to the average in the 10-ps production run at fixed d. σ^{zz} was computed as

$$\sigma^{zz} = \sum_i \sigma_i^{zz} \tag{2.4}$$

where the sum is taken over the resin atoms i except for those restrained in the top 2.0-nm region of the resin layer. σ_i^{zz} is the stress on atom i introduced as

$$\sigma_i^{ab} = m_i v_i^a v_i^b + \frac{1}{2}\sum_{i \neq j} \left(\frac{r_{ij}^a r_{ij}^b}{r_{ij}} \right) \left(\frac{\partial U_{ij}}{\partial r_{ij}} \right) \tag{2.5}$$

where m_i and v_i are respectively the mass and velocity of the ith atom, a and b refer to the x, y or z direction, r_{ij}^a is the a-component of the vector connecting from the ith to the jth atom, U_{ij} and r_{ij} are the pair potential and the radial distance between the ith and jth atoms, respectively, and the sum in the second term is taken over j. σ_i^{ab} was computed using *compute stress/atom* command in LAMMPS [151–153]. V_{resin} corresponds to the volume occupied by the unrestrained resin molecules and was introduced by

$$V_{\text{resin}} = \frac{N_{r,u}}{N_r} V \tag{2.6}$$

where V is the system volume of the resin right after the procedures in Table 2.2 are finished and N_r and $N_{r,u}$ are the numbers of total and unrestrained resin atoms, respectively. Although P_{push} is not literally equal to the pushing pressure, it is a measure with an ambiguity of $O(N_{r,u}/N_r)$, which is less than 0.1 in the present simulations. In fact, the measured quantity is the stress σ^{zz}. It is not an intensive property, however, and P_{push} is employed to show the results with an intensive one. In Fig. 2.3, we show P_{push} as a function of d. It is seen that P_{push} is unchanged within 20 MPa till $d \simeq -1$ and rises steeply at $d \lesssim -2$; the pressure calculation involves an error of 20 MPa. The rise of P_{push} is mild for entry 4-1, where the relative size of the resin to the pore is the smallest in Table 2.1, and P_{push} exceeds a few hundred MPa at $d \simeq -3$ for the other entries. At R_{p} = 2.0, 2.5 and 5.0 nm, P_{push} reaches 1000 MPa at $d \simeq -3.5$, $d \simeq -4.0$, and $d \lesssim -4.0$, respectively. The pushing is harder for a smaller pore, while it is commonly seen that an impractically high pressure is applied at late stage of pushing process (note that $n = 600$ at $d = -4.0$ and that the resin was pushed by 700 steps in total). At R_{p} = 7.5 nm, P_{push} stays several hundred MPa even at the end of the process ($d \simeq -5.0$). It should be actually noted that P_{push} at common $R_{\text{g}}/R_{\text{p}}$ rises more slowly at R_{p} =

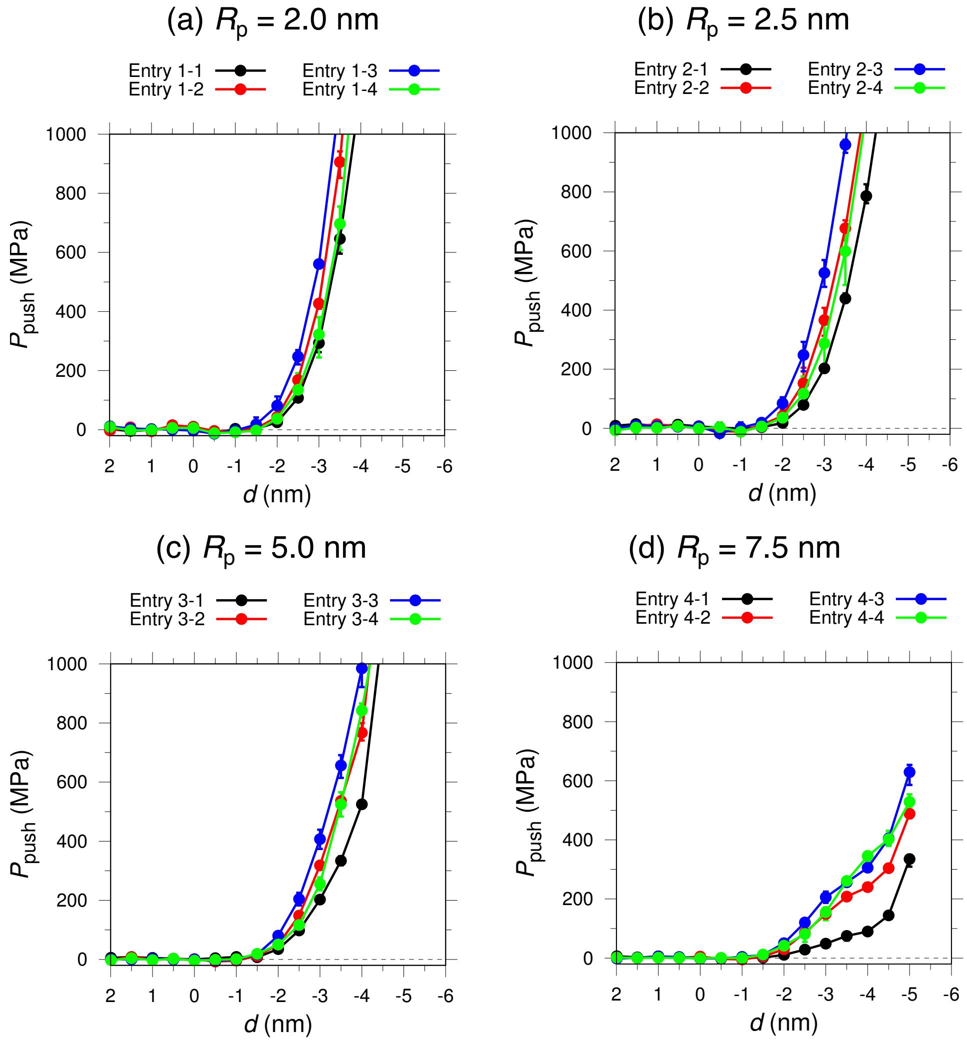

Figure 2.3: Pushing pressure P_{push} defined as Eq. (2.3), plotted against the pushing index d of Eq. (2.1). See Table 2.1 for the entry of the system. The dotted line refers to $P_{\text{push}} = 0$.

7.5 nm than at the others. This shows that the d dependence of P_{push} does not simply scale with R_g/R_p. The steep rise of P_{push} at the early stage of resin filling was also observed in Kim et al's and Yasuda et al's studies of polyethylene and polymethylmethacrylate into pores of silicon [100, 140]. Our resins have aromatic and hydrophilic groups as shown in Fig. 2.2, and the rising tendency of P_{push} at the entrance of the pore may not be strongly affected by the chemical composition of the resin (polymer).

The extent of filling was quantified with the density of the resin in the pore defined as

$$\rho_{\text{pore}} = \langle \frac{1}{V_{\text{pore}}} \sum_i m_i \rangle_d \tag{2.7}$$

where V_{pore} is the volume of the cylindrical pore, m_i denotes the mass of the ith atom, the sum is taken only over the resin atoms contained in the pore region, and $\langle \cdots \rangle_d$ is the average over the 10-ps production run at fixed d. Fig. 2.4 plots ρ_{pore} as a function of d. It is observed that ρ_{pore} increases faster with the pushing (decrease of d) for a smaller resin; the filling proceeds more efficiently for a resin with smaller radius of gyration R_{g} defined by Eq. (2). According to Fig. 2.1 and Eq. (2.1), in fact, the pushing index d is defined so that if the process were done at macroscopic scale, d were zero at the entrance and were -5.0 at full filling. The computed ρ_{pore} does not correspond to this "macroscopic" expectation in which ρ_{pore} grows linearly with d in the range of $-5 \leq d \leq 0$. ρ_{pore} is appreciable only in $d \lesssim -2$ and reaches half the bulk density (0.5 g/cm^3) only at $-3 \lesssim d \lesssim -4$. The filling to half density is thus slower than the macroscopic expectation and is more so at larger R_{g}. When Figs. 2.3 and 2.4 are compared, $d \simeq -2$ corresponds to the step of pushing where both the pressure and density rise. The intrusion of resin starts at $d \simeq -2$ and brings the increase of the pressure.

To see the relationship between the pushing pressure and the extent of filling, ρ_{pore} is plotted against P_{push} in Fig. 2.5. It is observed at each radius of the pore R_{p} that ρ_{pore} for smaller resin increases faster with P_{push}, while the difference in ρ_{pore} is not appreciable among entries 1-2, 1-3, and 1-4. The previous work also analyzed ρ_{pore} at fixed R_{p} = 2.5 nm and showed that the pressure can be lowered by introducing a resin with smaller R_{g} into the pore [139]. Fig. 2.5 demonstrates the validity of this result over wider ranges of R_{g} and R_{p}. When the pore is small and its radius R_{p} is 2.0 or 2.5 nm, ρ_{pore} reaches half of the averaged bulk value (1.01 g/cm^3 obtained for the bulk density from step 12 in Table 2.2) only beyond 500 MPa of P_{push}. In a previous work [139], it was shown that the half filling is achieved for the pore of $R_{\text{p}} = 2.5$ nm when $R_{\text{g}} \lesssim R_{\text{p}}/2$, where R_{g} is the resin radius of gyration defined by Eq. (2.2). Actually, the pore was seen to deform when a larger resin

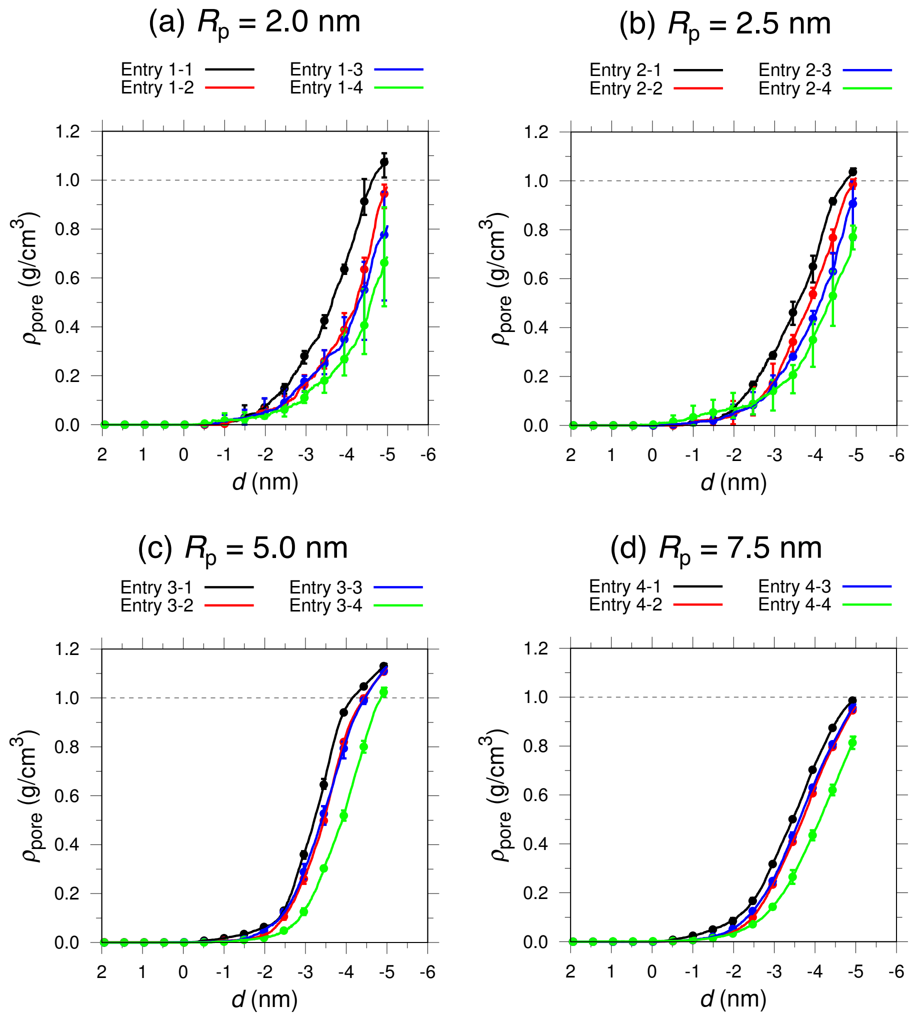

Figure 2.4: Density in the pore ρ_{pore} defined as Eq. (2.7), plotted against the pushing index d of Eq. (2.1). See Table 2.1 for the entry of the system. The dotted line refers to the averaged bulk density of the resin computed at step 12 in Table 2.2.

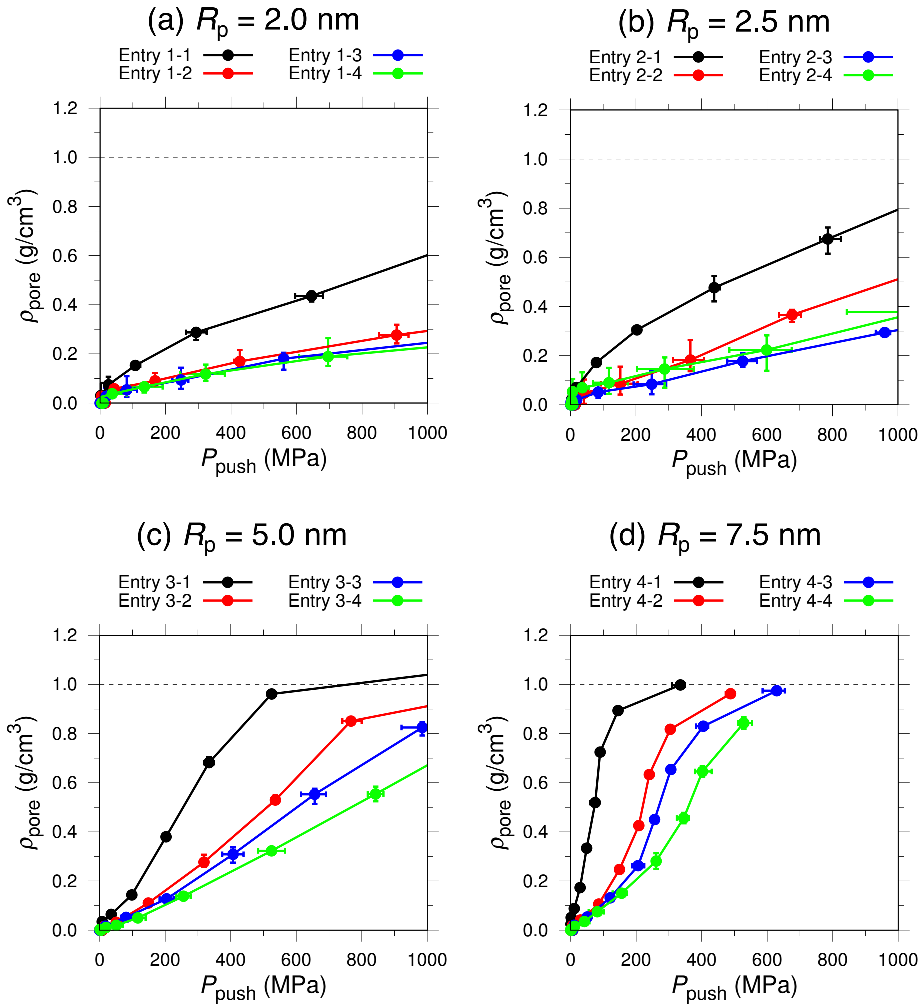

Figure 2.5: Density in the pore ρ_{pore} against the pushing pressure P_{push}. See Table 2.1 for the entry of the resin and Eqs. (2.3) and (2.7) for the definitions of P_{push} and ρ_{pore}, respectively. The dotted line refers to the averaged bulk density of the resin computed at step 12 in Table 2.2.

is filled to half, and at the deformation, $P_{\text{push}} \simeq 1000$ MPa. ρ_{pore} is thus practically less than the half density at $R_{\text{p}} = 2.0$ or 2.5 nm, since the commonly applied pressure is smaller than 100 MPa to avoid the deformation of metal. With $R_{\text{g}}/R_{\text{p}} = 0.07$ (entry 4-1 of Table 2.1), the half density is attained at $P_{\text{push}} \simeq 100$ MPa. The half filling is available only for a resin smaller by $\sim$1/10 than the pore as far as the pressure remains practical. ρ_{pore} increases faster with P_{push} when the resin is smaller and/or the pore is larger. The pressure is more effective to fill the pore at small $R_{\text{g}}/R_{\text{p}}$.

Fig. 2.6 shows ρ_{pore} at fixed P_{push} of 50, 100, 500, and 1000 MPa against the relative size of resin and pore expressed as $R_{\text{g}}/R_{\text{p}}$. Only at $R_{\text{g}}/R_{\text{p}} = 0.07$, the pore is 30% filled at 50 MPa and

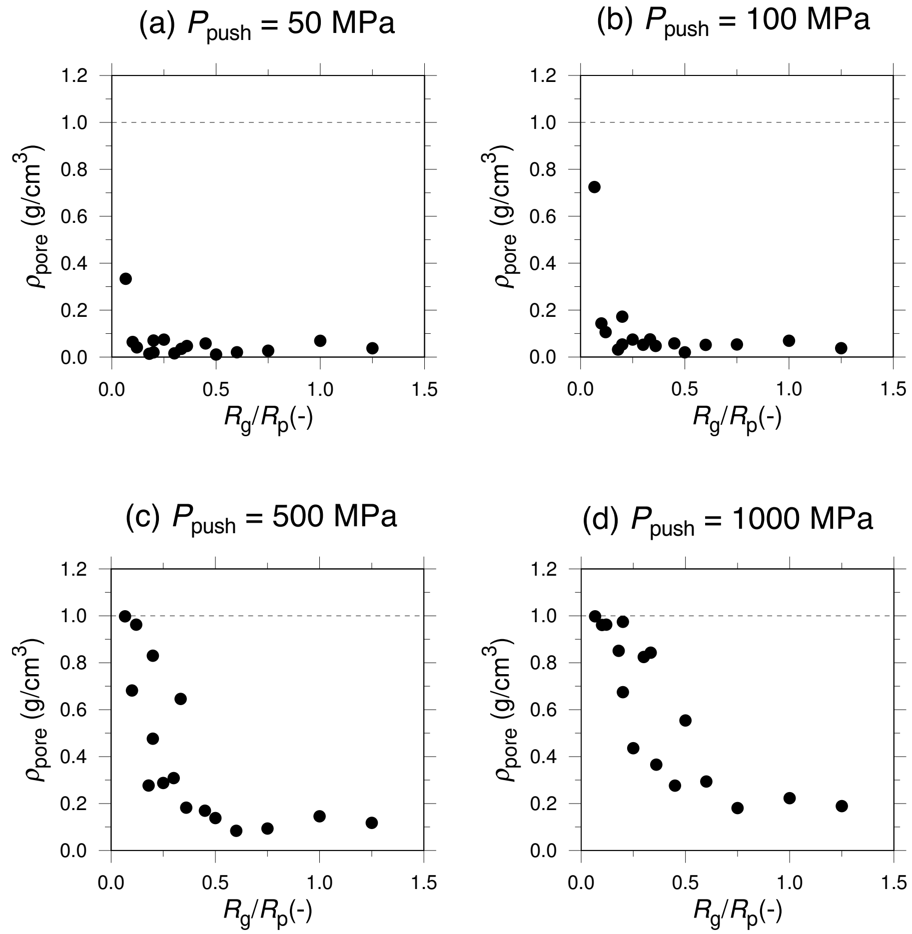

Figure 2.6: Relationship between $R_\mathrm{g}/R_\mathrm{p}$ and the density in the pore ρ_pore at P_push = 50, 100, 500, and 1000 MPa. See Eq. (2.2) for the definition of R_g. It should be noted that the values at $P_\text{push} = 50, 100, 500,$ and 1000 MPa in Fig. 2.6 are obtained by linearly interpolating the data of Fig. 2.5. The dotted line refers to the averaged bulk density of the resin computed at step 12 in Table 2.2.

70% at 100 MPa. This implies that the resin filling at practical pressure is effectively attained at $R_\mathrm{g}/R_\mathrm{p} \lesssim 0.1$. When the resin is larger, the filling can be achieved only through hard pushing. At $R_g/R_p \simeq 0.25$, for example, the pore is filled to half with $P_\text{push} \simeq 500$ MPa and the full filling needs $\simeq$1000 MPa. The half filling of the pore is not possible even with $P_\text{push} \gtrsim 1000$ MPa when $R_\mathrm{g}/R_\mathrm{p} \gtrsim 0.5$.

We saw that a large pressure is necessary for resin filling. To obtain spatially resolved views on the pressure, the stress map of resin in and around the pore was analyzed. The stress map was computed by defining a set of small cells in the simulation box with linear bins of $\Delta z = 0.2$ nm along the vertical direction (z direction in Fig. 2.1) and concentric bins of $\Delta r = 0.2$ nm over the lateral directions; the concentric bins were used since the pore is of cylindrical symmetry. The local pressure within each cell was then calculated through

$$P_L = \langle \frac{1}{V_{\text{cell}}} \sum_i \sigma_i^{zz} \rangle_d \tag{2.8}$$

where V_{cell} denotes the volume of the small cell, σ_i^{zz} is the zz component of the stress tensor from the ith atom introduced by Eq. (2.5), the sum is taken only over the resin atoms contained in the cell, and $\langle \cdots \rangle_d$ is the average over the 10-ps production at fixed d. Fig. 2.7 illustrates the stress map for a set of $R_{\text{g}}/R_{\text{p}}$ and d; P_L is shown for all the entries of Table 2.1 in Supplementary Material. When the pore is small and $R_{\text{p}} = 2.0$ or 2.5 nm, P_L of several hundreds of MPa is observed at $d \simeq -4$ and is localized above the pore; it is seen that a strong stress is not present within the pore. This indicates that the resin is congested at the entrance of the pore, and at $R_{\text{g}}/R_{\text{p}} \gtrsim 0.5$, the stress is not distributed uniformly into the pore even when $d \approx -5$ and the pore is more than half filled (see Fig. 2.4). For the larger pores of R_{p} = 5.0 and 7.5 nm, on the other hand, a high P_L is seen only outside the cylindrical region corresponding to the pore ($r > R_{\text{p}}$); entry 4-1 is exceptional in that the stress distributes uniformly in and around the pore. In any case, the spontaneous motion of the resin is inhibited from a region with increased stress. The non-uniform distribution of the stress indicates that the resin structure is not well relaxed right before the penetration into the pore, furthermore, and it is accordingly inferred that the pushing is too fast compared to the relaxation of the resin to effectively fill the pore. Although our pushing rate corresponds to the experimental practice, it is suggested that a reduced rate be employed toward more efficient filling. It is also to be noted that R_{p} can be several tens of nm in realistic manufacturing process, while R_{g} in the present study corresponds to the resin size actually used [45–47]. This means that a smaller $R_{\text{g}}/R_{\text{p}}$ may be employed in practice, which further facilitates the filling with weaker pushing.

As discussed with respect to Fig. 2.3, Kim et al examined the filling of polyethylene into a cylindrical pore of silicon. The system was simulated above the glass transition temperature of polyethylene, and it was observed that the polymer with $R_\mathrm{g}/R_\mathrm{p} \simeq 1$ can fill well into the pore even at several tens of MPa [140]. The present study shows, on the other hand, that the efficient filling is achieved only at $R_\mathrm{g}/R_\mathrm{p} \lesssim 0.1$ when $P_\mathrm{push} \lesssim 100$ MPa. This difference can be attributed to the state of the polymer (resin). Our resins are more viscous than polyethylene treated in Ref. 140. They are then more difficult to be filled in the pore since the relaxation of the molecular structure is slower for a more viscous species; the reduced efficiency of filling in the present work is evidenced as the smaller range of $R_\mathrm{g}/R_\mathrm{p}$ for filling as mentioned above. It is also expected that P_push reduces at high temperature, and this is indeed observed by Kim et al for polyethylene into a silicon pore [140].

To obtain the spatially resolved view of the resin density, the density map of filling was also examined. The density map was calculated by the similar equation to Eq. (2.8) expressed as

$$\rho_L = \langle \frac{1}{V_\mathrm{cell}} \sum_i m_i \rangle_d, \tag{2.9}$$

and is illustrated in Fig. 2.8; ρ_L is depicted for all the entries of Table 2.1 in Supplementary Material. It is seen for all the entries that the resin initially penetrates along the metal wall. The resin-metal interaction brings the wetting of the metal wall and acts as a driving force for filling. A strengthened interaction between the resin and wall can thus facilitate their tighter adhesion. Above the pore, a high-density region appears more strongly at larger $R_\mathrm{g}/R_\mathrm{p}$. This means the congestion of the resin at the pore entrance, and the smooth filling is inhibited by the resin-resin interaction. The increase of the resin size leads to stronger interactions among the resins and needs to be counteracted by a high pressure to fill the nano-sized pore.

2.4 Conclusion

The resin filling into nano-sized pore was simulated with all-atom MD simulation. The resin systems treated were the mixture of polyphenol and polyglycidylether of *o*-cresol formaldehyde novolac and their oligomers formed through ring-opening reactions. A variety of resin and pore sizes were examined, which were from 0.5 to 2.5 nm for the radius of gyration and from 2.0 to 7.5 nm

(a) $R_g/R_p = 1.25$ (R_g= 2.5 nm, R_p= 2.0 nm, Entry 1-4)

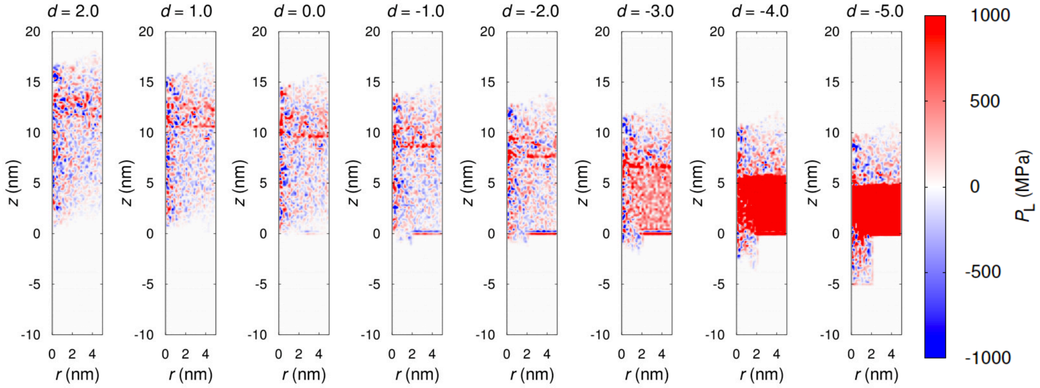

(b) $R_g/R_p = 0.3$ (R_g= 1.5 nm, R_p= 5.0 nm, Entry 3-3)

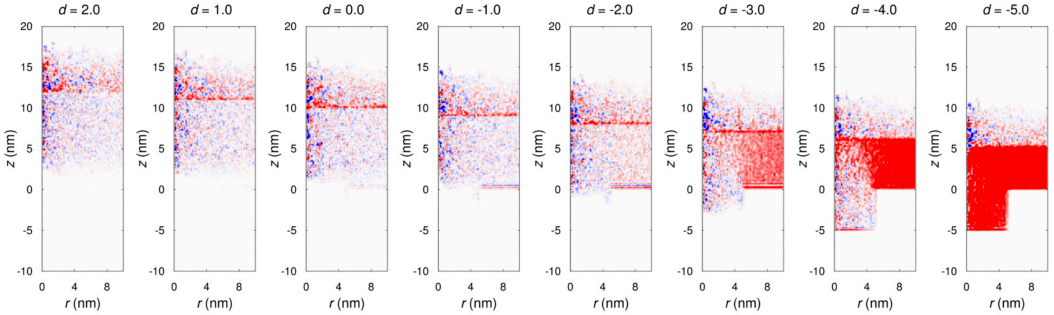

(c) $R_g/R_p = 0.07$ (R_g= 0.5 nm, R_p= 7.5 nm, Entry 4-1)

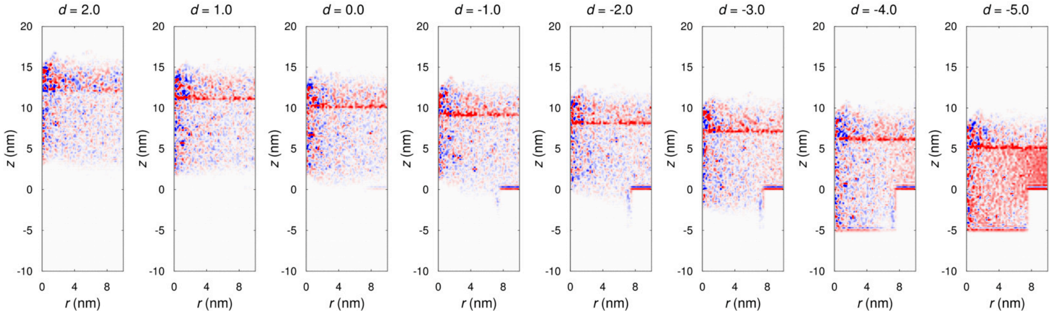

Figure 2.7: Stress map of the resin calculated by Eq. (2.8), where z is the coordinate along the direction of depth of the cylindrical pore (z direction in Fig. 2.1) and r is the radial distance over the lateral directions from the center of the cylinder. $z = 0$ is shifted to the "top" position of the pore before the pushing starts ($d = 2$ in Eq. (2.1)). See Table 2.1 for the entry of the system. P_L is defined to be positive when the force points to the direction of pushing (negative z direction)

(a) R_g/R_p = 0.07 (R_g= 0.5 nm, R_p= 7.5 nm, Entry 4-1)

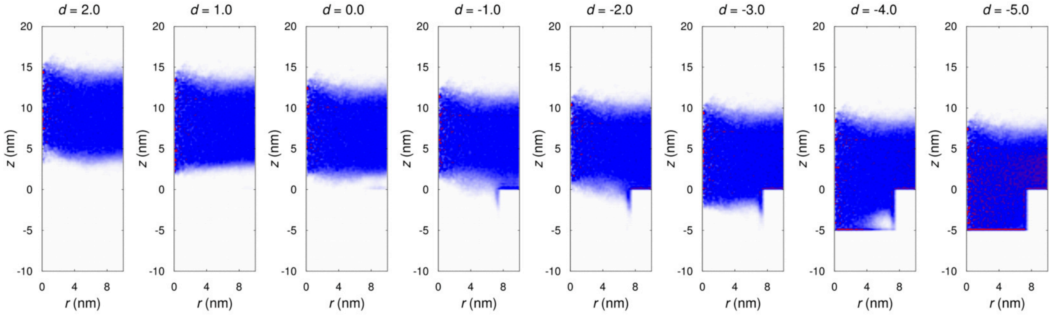

(b) R_g/R_p = 1.25 (R_g= 2.5 nm, R_p= 2.0 nm, Entry 1-4)

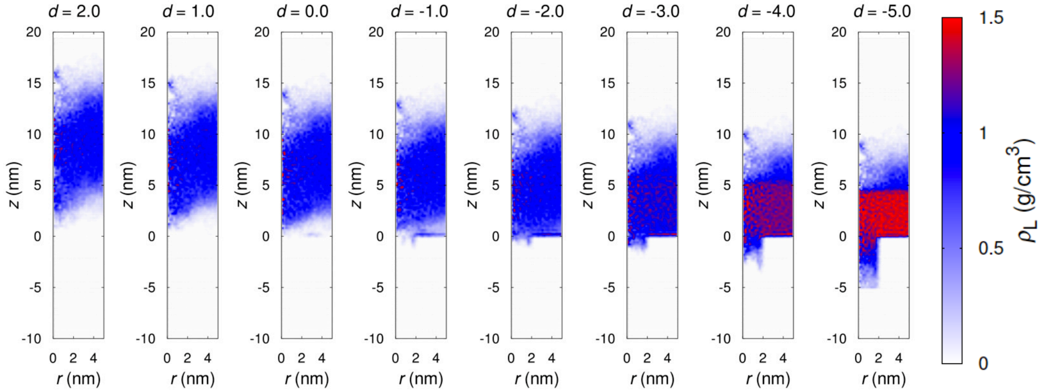

Figure 2.8: Density map of resin calculated by Eq. (2.9), where z is the coordinate along the direction of depth of the cylindrical pore (z direction in Fig. 2.1) and r is the radial distance over the lateral directions from the center of the cylinder. $z = 0$ is shifted to the "top" position of the pore before the pushing starts ($d = 2$ in Eq. (2.1)). See Table 2.1 for the entry of the system.

for the radius of the pore. The filling was simulated by pushing the resin layer to metal layer at a common rate in reality, and the pushing pressure was monitored to see the relationship between the extent of filling and the pushing pressure. The pore is 30% filled at 50 MPa of pushing pressure and 70% at 100 MPa when the radius of gyration of resin is smaller than 1/10 of the pore radius. This implies that the resin filling at practical pressure is effectively attained when the resin is smaller than the pore by an order of magnitude. To establish a local picture of the pushing process, the stress map was analyzed in and around the pore. A non-uniform distribution was then observed for the local stress, indicating that the resin structure is not well relaxed at a common rate of pushing. It is thus suggested that a reduction of the pushing rate can be an approach for more effective filling. The dynamics of filling was also examined in terms of the density map, and it was observed that the resin-resin interaction brings the congestion at the pore entrance.

2.5 Supplementary material

Stress map of the resin calculated by Eq. (8), where z is the coordinate along the direction of depth of the cylindrical pore (z direction in Fig. 1) and r is the radial distance over the lateral directions from the center of the cylinder. $z = 0$ is shifted to the top position of the pore before the pushing starts ($d = 2$ in Eq. (1)). See Table 1 for entry of the system. P_L is defined to be positive when the force points to the direction of pushing (negative z direction).

Entry1-1 ($R_g/R_p = 0.25$, $R_g = 0.5$ nm, $R_p = 2.0$ nm)

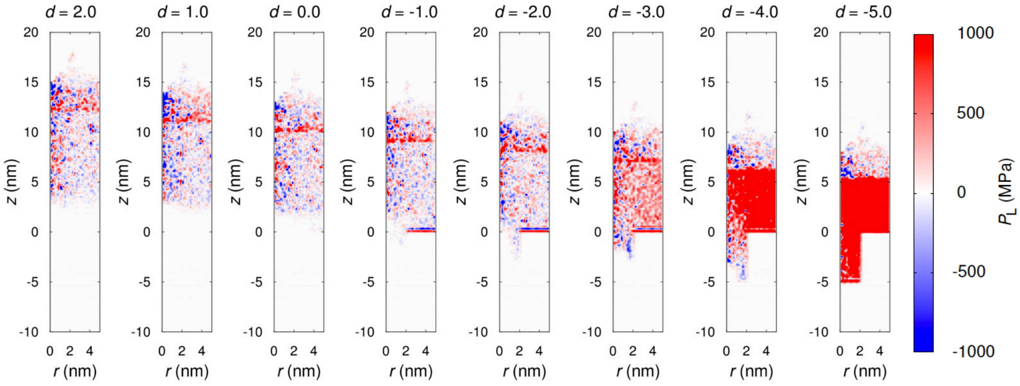

Entry1-2 ($R_g/R_p = 0.45$, $R_g = 0.9$ nm, $R_p = 2.0$ nm)

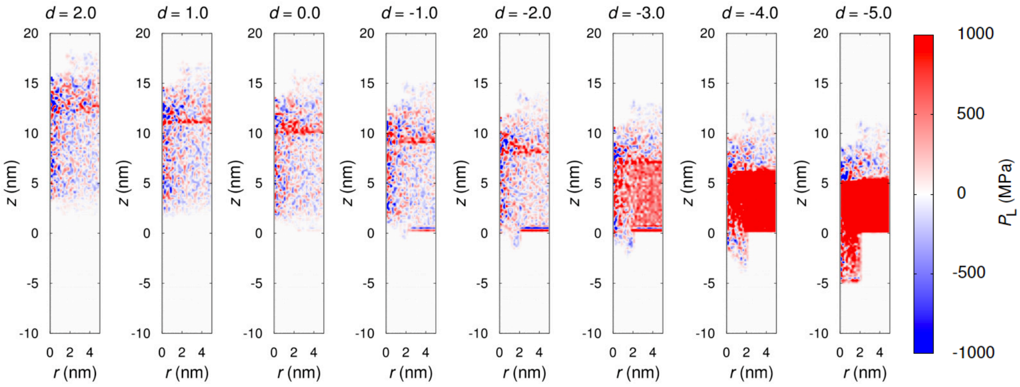

Entry1-3 ($R_g/R_p = 0.75$, $R_g = 1.5$ nm, $R_p = 2.0$ nm)

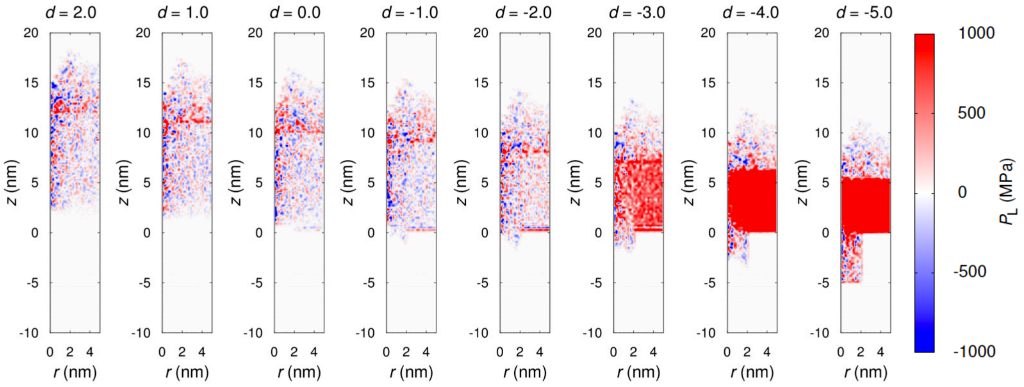

Entry1-4 ($R_g/R_p = 1.25$, $R_g = 2.5$ nm, $R_p = 2.0$ nm)

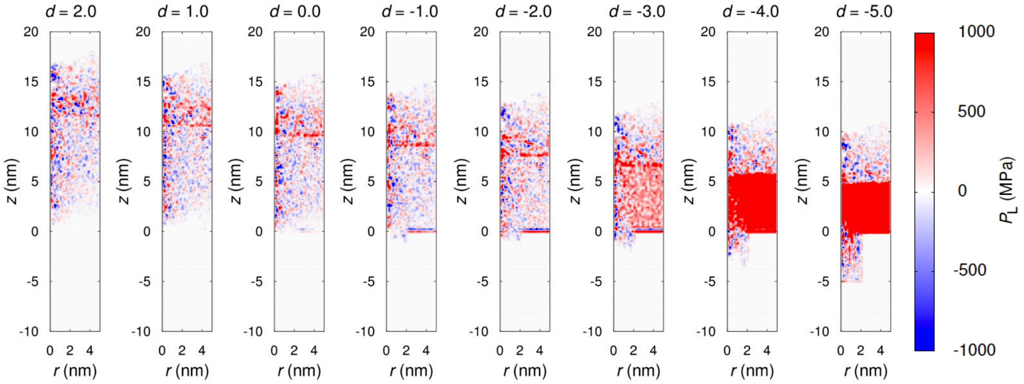

Entry2-1 ($R_g/R_p = 0.20$, $R_g = 0.5$ nm, $R_p = 2.5$ nm)

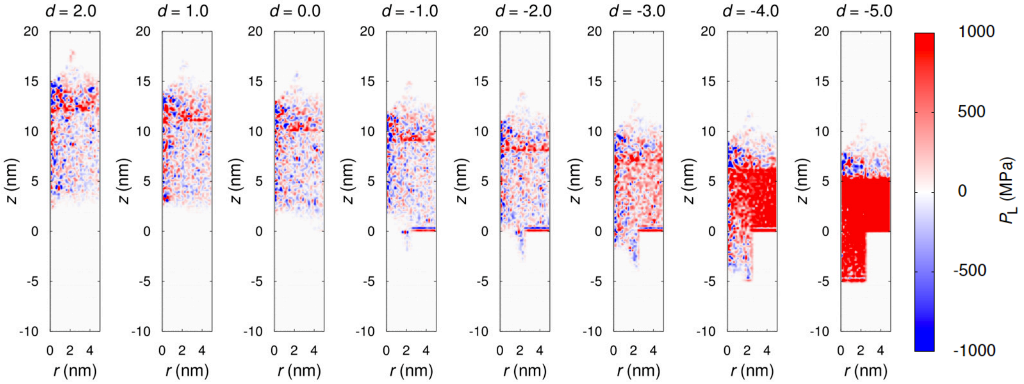

Entry2-2 ($R_g/R_p = 0.36$, $R_g = 0.9$ nm, $R_p = 2.5$ nm)

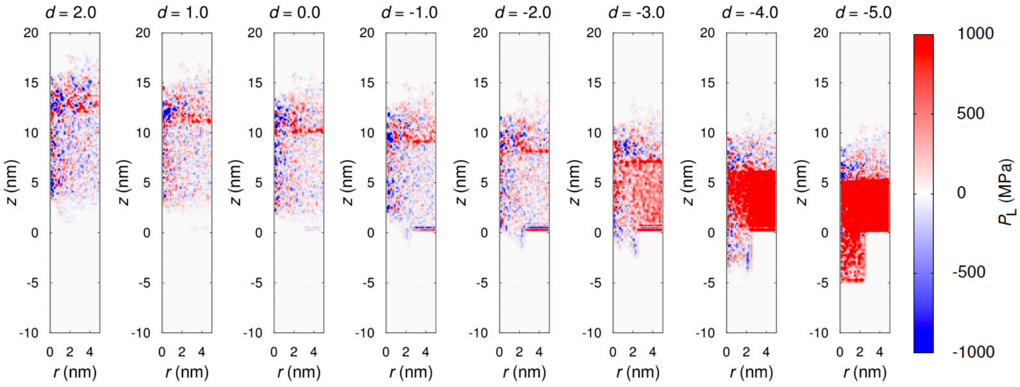

Entry2-3 ($R_g/R_p = 0.60$, $R_g = 1.5$ nm, $R_p = 2.5$ nm)

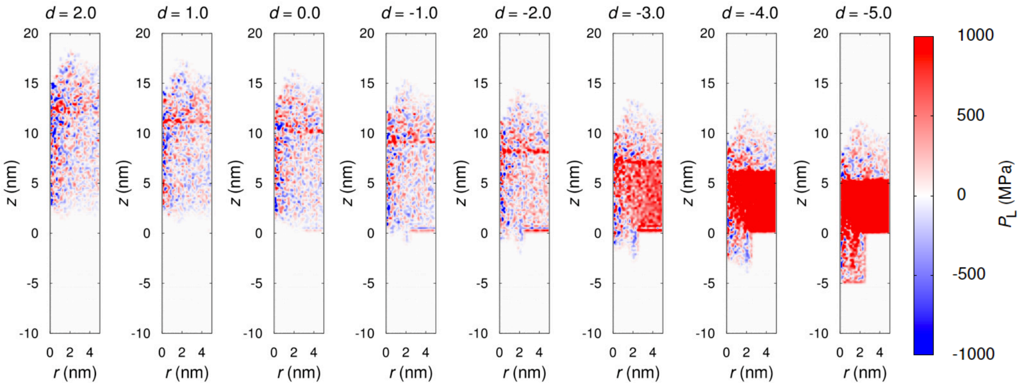

Entry2-4 ($R_g/R_p = 1.00$, $R_g = 2.5$ nm, $R_p = 2.5$ nm)

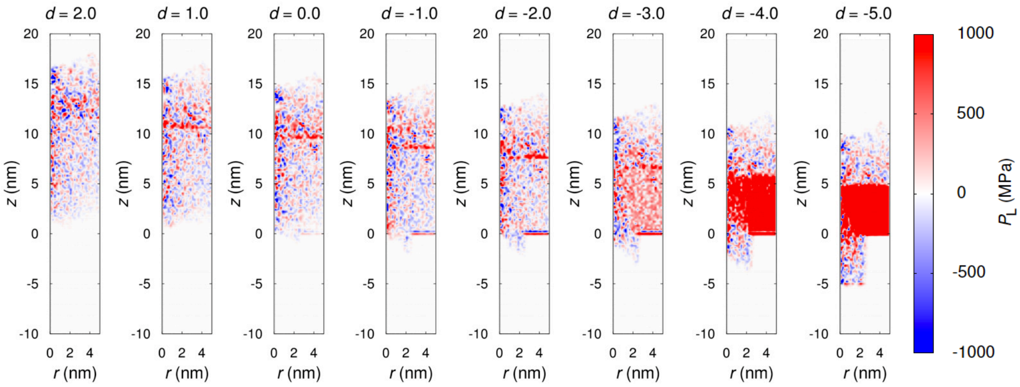

Entry3-1 ($R_g/R_p = 0.10$, $R_g = 0.5$ nm, $R_p = 5.0$ nm)

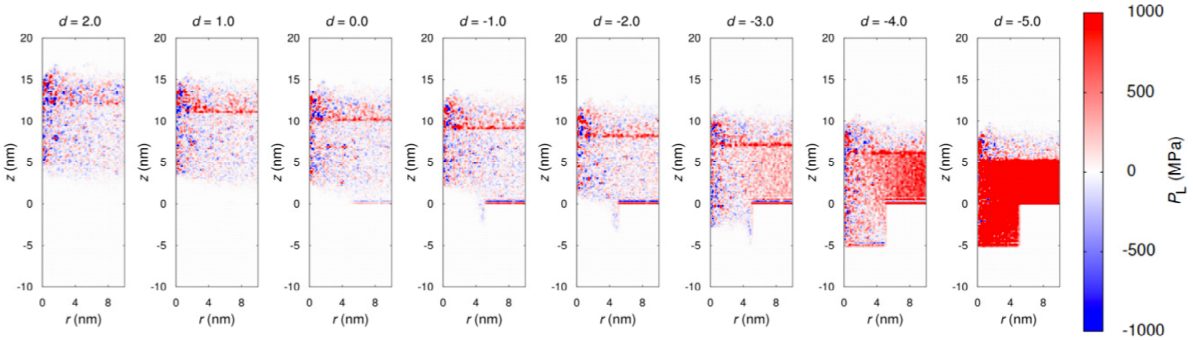

Entry3-2 ($R_g/R_p = 0.18$, $R_g = 0.9$ nm, $R_p = 5.0$ nm)

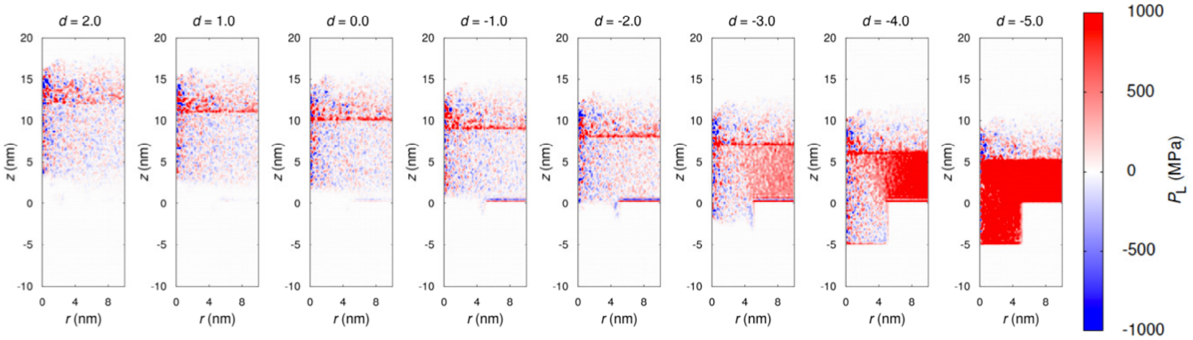

Entry3-3 ($R_g/R_p = 0.30$, $R_g = 1.5$ nm, $R_p = 5.0$ nm)

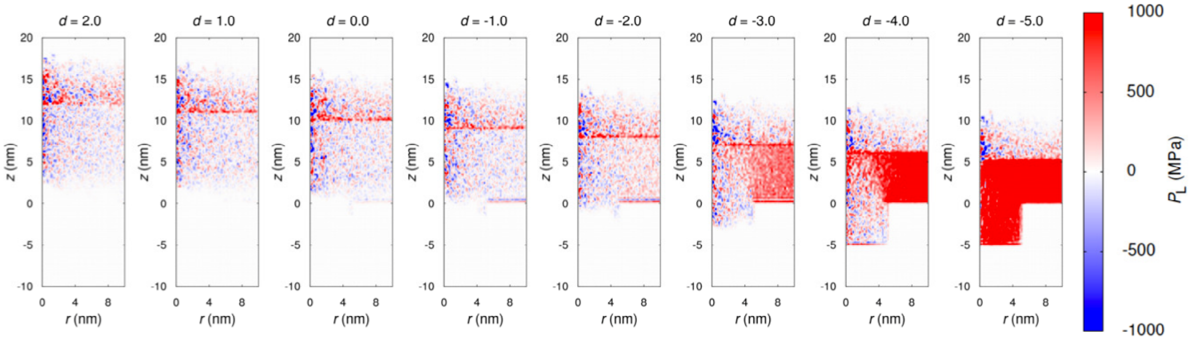

Entry3-4 ($R_g/R_p = 0.50$, $R_g = 2.5$ nm, $R_p = 5.0$ nm)

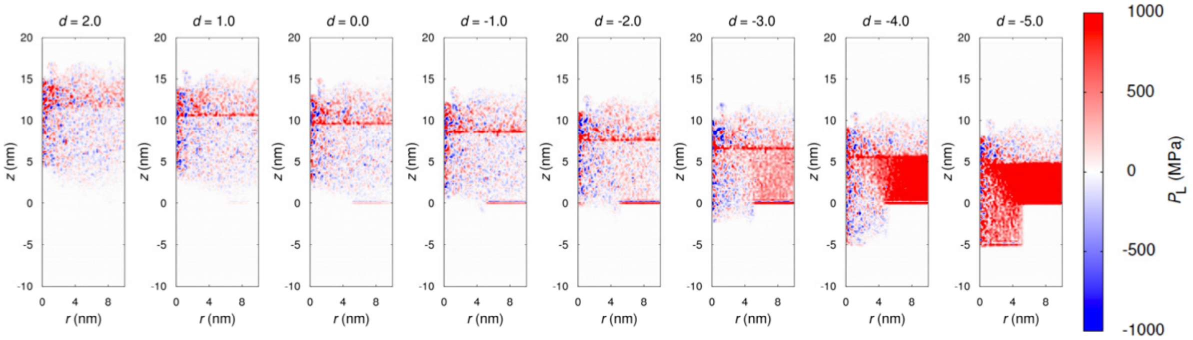

Entry4-1 ($R_g/R_p = 0.07$, $R_g = 0.5$ nm, $R_p = 7.5$ nm)

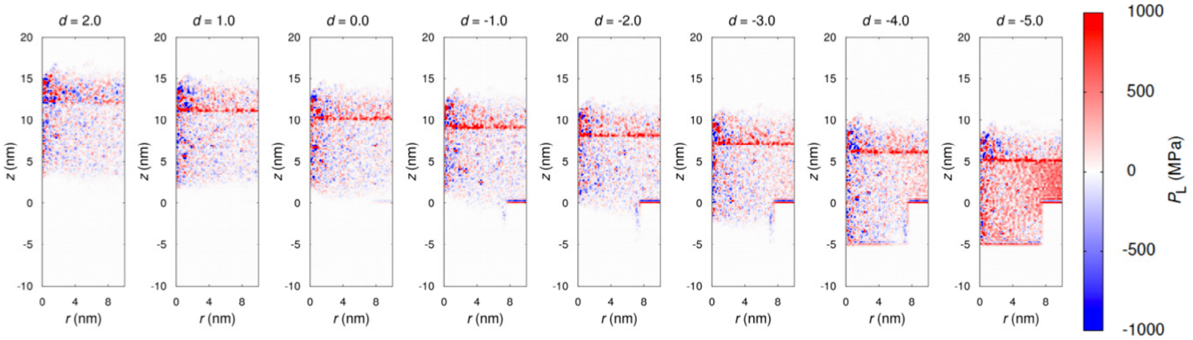

Entry4-2 ($R_g/R_p = 0.12$, $R_g = 0.9$ nm, $R_p = 7.5$ nm)

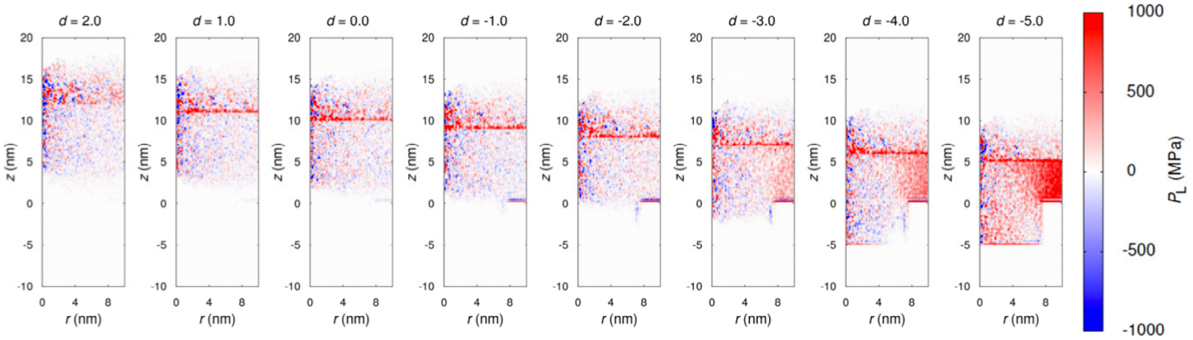

Entry4-3 (R_g/R_p = 0.20, R_g = 1.5 nm, R_p = 7.5 nm)

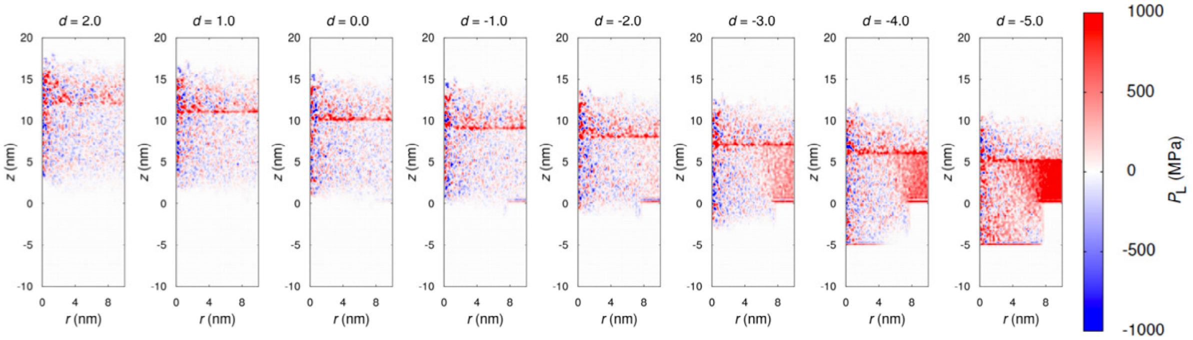

Entry4-4 (R_g/R_p = 0.33, R_g = 2.5 nm, R_p = 7.5 nm)

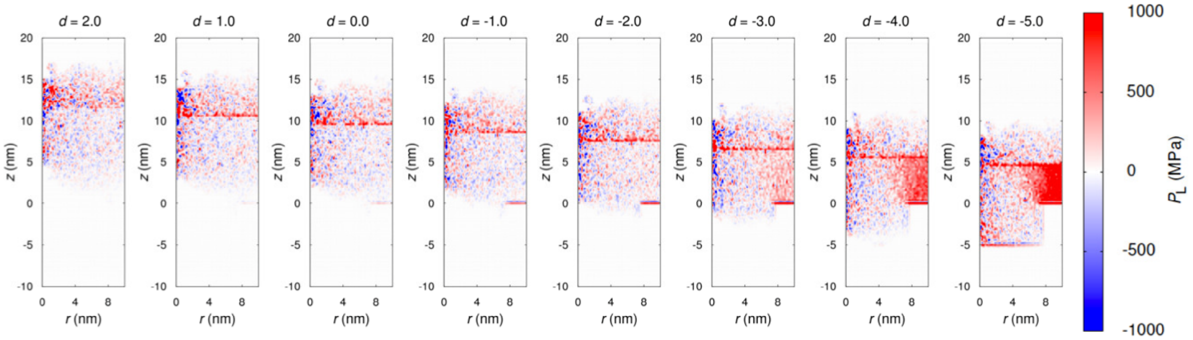

Chapter 3

Local Viscoelasticity at Resin-Metal Interface Analyzed with Spatial-Decomposition Formula for Relaxation Modulus

3.1 Introduction

Multi-material adhesion involving a resin-metal interface has been widely used in electronic devices for automobile [4, 5]. The mode of adhesion is governed by the physico-chemical properties at the interface, and reflects intermolecular interactions in inhomogeneous environments. [21–25] Viscoelasticity is a measure for assessing the adhesion strength against the stress [26–29]. Still, the stress distribution is not uniform around the interface, and the role of interface can be assessed by taking into account the spatial variation of the local stress. Indeed, it is experimentally suggested that resin at several nm from a metal interface can have different solubility and glass-transition temperature compared to the bulk [154–157]. The spatial resolution of nm scale is thus desired for the viscoelastic analysis of adhesion interface.

Nanoscale resolutions of space and time have been sought experimentally for resin-metal interface. Space-resolved fluorescence spectroscopy, sum-frequency generation (SFG) vibrational spectroscopy, and X-ray photon correlation spectroscopy have revealed the dynamics of resin near substrate [51–60] , though it is still a subject of active development to directly evaluate the viscoelasticity around the resin-metal interface. Molecular dynamics (MD) simulation is a powerful technique to analyze a multi-material interface. It can describe microscopic processes of adhesion with spatial resolution of nm and temporal resolutions of ps, and has proven to be useful in addressing the wetting of substrate, nano-scale filling of adhesive into metal pore, and nanoimprint lithography [68, 71, 73, 100–102, 140, 158–163]. In the present work, we analyze the local stress at the resin-metal interface by coarse-grained MD simulation in connection to the viscoelasticity of adhesion.

Viscoelasticity is quantified by the relaxation modulus, which is the autocorrelation function of the stress tensor. Its zero-time value provides the extent of stress fluctuation and the time integral determines the viscosity. The correlation function contains information only in time domain, however. The spatial resolution is not involved in the original Green-Kubo-type formulation. Recently, the method of spatial decomposition has been developed to obtain spatially resolved insights into transport and spectroscopic quantities [82–84, 164–172]. In this method, a time correction function conditioned by a spatial variable such as particle-particle distance is defined to express a dynamic observable of interest as an integral over the space. In the case of electrical conductivity, for example, the correlated motions of ions are conditioned by the ion-ion distance and the extent of spatial localization of the ion-pair contribution to the conductivity is examined by introducing a cutoff into the integral expression and assessing the convergence of the integral with respect to the cutoff length [83, 84, 172]. The spatial decomposition was also conducted to connect thermodynamic quantities to molecular distribution (correlation) functions [85, 173–176]. Partial molar quantities of hydration were formulated as integrals over the whole space, and the localization of the solute's effect on solvent water were addressed.

In the present work, we formulate a spatial-decomposition method for relaxation modulus and apply it to a resin-metal interface. The distance along the normal direction to the planar interface is adopted as the spatial coordinate to introduce a spatially decomposed time correlation function as a conditional average. The spatial inhomogeneity of temporal variation of the stress can then be analyzed in connection to the viscoelasticity at the interface. Coarse-grained MD is done for an oligomer of polyglycidylether of *o*-cresol formaldehyde novolac and polyphenol at flat interfaces with platinum and aluminum. The stress-stress correlation is analyzed at the segment-scale space and time, and a slower relaxation is observed in the resin layers on the metal when the resin is tightly adhered.

Our model resin is commonly used as a thermoset for electronic devises. The effect of the resin-metal interaction is also examined by scaling the interaction parameter. The point of the present work is to connect the viscoelastic inhomogeneity and the adhesion strength, and the method developed is applicable to both all-atom and coarse-grained simulations. We will examine the extent of localization of the interface's effect on the stress-stress correlation of the resin.

3.2 Theory

Viscoelasticity describes the time-dependent response of the stress against the strain. In the linear-response regime, it is quantified by the relaxation modulus, which is further determined by the time correlation function of the stress at equilibrium. In this section, we incorporate the spatial view into the relaxation modulus by defining the stress correlation function conditioned by the position of a particle in the system; the particle refers to an atom in the all-atom treatment and to a segment in the coarse-grained modeling.

The stress tensor on the ith particle σ_i^{ab} is defined as

$$\sigma_i^{ab} = m_i v_i^a v_i^b + \frac{1}{2}\sum_{j \neq i}\left(\frac{r_{ij}^a r_{ij}^b}{r_{ij}}\right)\left(\frac{\partial U_{ij}}{\partial r_{ij}}\right) \tag{3.1}$$

where m_i and v_i are respectively the mass and velocity of the ith particle, a and b refer to the x, y or z direction, r_{ij}^a is the a-component of the relative position between the ith and jth particles, U_{ij} and r_{ij} are the pair potential and the radial distance between the ith and jth particles, respectively, and the sum is taken over j. In Eq. (3.1), the first term is the kinetic contribution involving only the translational velocity, and the second term is the contribution from the inter-particle interaction. See Appendix 3.6.1 for more discussion on the form of σ_i^{ab}. According to the linear-response theory, the relaxation modulus $G^{ab}(t)$ is expressed with $\sigma_i^{ab}(a \neq b)$ as

$$G^{ab}(t) = \frac{1}{k_B T V}\langle \sum_i \sigma_i^{ab}(0) \sum_j \sigma_j^{ab}(t) \rangle \tag{3.2}$$

where t is the lag time, k_B is the Boltzmann constant, T is the temperature, V is the volume of the system, and $\langle \cdots \rangle$ refers to the average over the configurations at the initial time ($t = 0$). Eq. (3.2) shows that the relaxation modulus is expressed as the autocorrelation function of the stress tensor, and the viscoelasticity has been analyzed for resin systems on the basis of Eq. (3.2) [177–179]. It should be noted that the relaxation modulus is actually given as the sum of $G^{ab}(t)$ of Eq. (3.2) and the static elastic modulus G_s [180–183]. G_s vanishes for a fluid, while it is positive otherwise. This work focuses only on the time-dependent part of the relaxation modulus given by Eq. (3.2) to examine the position dependence of the stress-stress time correlation, and $G^{ab}(t)$ of Eq. (3.2) is called relaxation modulus throughout the paper.

We now decompose Eq. (3.2) in terms of the spatial position. To do so, we introduce a conditional time correlation function as

$$\Gamma^{ab}(t;\mathbf{r}) = \frac{\langle \sum_i \delta(\mathbf{r}-\mathbf{r}_i(0))\sigma_i^{ab}(0)\sum_j \sigma_j^{ab}(t)\rangle}{\langle \sum_i \delta(\mathbf{r}-\mathbf{r}_i(0))\rangle} \tag{3.3}$$

where $\mathbf{r}_i(t)$ is the position vector of the ith particle and the delta function $\delta(\mathbf{r}-\mathbf{r}_i(0))$ serves to categorize the particle according to its position at the initial time. With Eq. (3.3), the relaxation modulus is decomposed as

$$G^{ab}(t) = \frac{1}{k_B TV}\int d\mathbf{r}\Gamma^{ab}(t;\mathbf{r})\rho(\mathbf{r}), \tag{3.4}$$

where $\rho(\mathbf{r})$ is the local number density of the particle and is given by

$$\rho(\mathbf{r}) = \langle \sum_i \delta(\mathbf{r}-\mathbf{r}_i(0))\rangle. \tag{3.5}$$

$\Gamma^{ab}(t;\mathbf{r})$ is the time correlation between the stress exerted on a particle with position $\mathbf{r}$ at time 0 and the stress of the whole system at time t. It is integrated with the weight of $\rho(\mathbf{r})$ over the whole space to determine the (total) modulus of relaxation. Since $\rho(\mathbf{r})d\mathbf{r}$ is the number of particles in the volume element $d\mathbf{r}$, Eq. (3.4) corresponds to the sum of the local modulus over all the particles in the system. $\Gamma^{ab}(t;\mathbf{r})$ does not depend on $\mathbf{r}$ in a homogeneous system, and it describes the dynamical inhomogeneity per particle when the system is not homogeneous. The local stress at $\mathbf{r}$ responds more slowly to the strain when $\Gamma^{ab}(t;\mathbf{r})$ persists over longer t, and such a spatial picture can be obtained on the basis of Eqs. (3.3)-(3.5) at particle resolution. It should be further noted that our formulation is parallel to the spatial-decomposition treatment of viscosity in Ref. 82.

In this work, we treat a planar interface. The spatial inhomogeneity is present along the direction normal to the interface, and the system is homogeneous over the lateral directions. When the z-axis is set to the normal direction, the spatially-decomposed time correlation function of the stress is introduced as

$$\Gamma^{xz}(t;z) = \frac{\langle \sum_i \delta(z - z_i(0)) \sigma_i^{xz}(0) \sum_j \sigma_j^{xz}(t) \rangle}{\langle \sum_i \delta(z - z_i(0)) \rangle}, \tag{3.6}$$

where $z_i(t)$ is the location along the z-direction of the ith particle at time t. The shear relaxation modulus is then given by an expression similar to Eq. (3.4) as

$$G^{xz}(t) = \frac{1}{k_B T L_z} \int dz \Gamma^{xz}(t;z) \rho(z), \tag{3.7}$$

$$\rho(z) = \frac{1}{S_{xy}} \langle \sum_i \delta(z - z_i(0)) \rangle, \tag{3.8}$$

where S_{xy} is the area of the system over the lateral directions and L_z is the z-length of the system. $\Gamma^{xz}(t;z)$ is the contribution to the relaxation modulus from a particle located at z along the normal direction at time 0, and $\rho(z)$ is the local density. For the resin-metal system of our interest, the xz or yz component of the relaxation modulus describes the response of the stress along the direction parallel to the interface against the shear strain building over the normal direction.

In our formalism, the relaxation modulus is decomposed in terms of the spatial distance from the interface. $\Gamma^{xz}(t;z)$ is a dynamical quantity per particle to describe the viscoelastic behavior at position z. It does not depend on z in the homogeneous bulk, and varies with z over a certain region near the interface. The spatial inhomogeneity of the time evolution of the stress is to be reflected in the z dependence of $\Gamma^{xz}(t;z)$, that provides dynamical information for the “thickness” of the interface in turn. $\rho(z)$ is a static property to describe the local density. The variation range of $\rho(z)$ with respect to z corresponds to the interfacial region (seen from the density), and $\Gamma^{xz}(t;z)\rho(z)dz$ is the contribution to the (total) relaxation modulus from the particles located in an infinitesimal region of z to $z+dz$; $\Gamma^{xz}(t;z)$ is the contribution from a single particle and is weighted by the number of particles $\rho(z)dz$. The general idea of the spatial-decomposition formula is to introduce a time correlation function conditioned by a spatial position and integrate it over the space for determining the total response function [82–84, 171, 172], and Eqs. (3.3) and (3.6) are specific forms of position-dependent correlation function to analyze the viscoelasticity.

In Eqs. (3.3) and (3.6), the sum over j is taken for all the particles in the system. It is not a sum over particles within a certain range around $\mathbf{r}$ or z that appears as the argument for the delta function in the sum over i. In particular, the particles involved in the sum over j is not restricted to those close to the particles contributing to the sum over i. Such “partial sum may be of physical appeal, while all the particles in the system are involved in the sums over j of Eqs. (3.3) and (3.6) in order to satisfy Eqs. (3.4) and (3.7). The left-hand sides of Eqs. (3.4) and (3.7) are the relaxation moduli, that are observables. These equations provide the connections between the local quantities of Eqs. (3.3) and (3.6) and the observables obtained as integrals over the whole space. Our spatial-decomposition formulae have been developed to assess the contribution of the local quantity to an integrated observable, and the “sum rules as in the forms of Eqs. (3.4) and (3.7) need to be kept to assure that the sum (integral) of the local contributions is equal to the observable [82–85, 171–176]. In Appendix 3.6.2, we note the summing procedures of Eqs. (3.3) and (3.6) in more details.

3.3 Methods

Coarse-grained MD simulations were performed to analyze the local viscoelasticities of the resin-metal systems. The interface between the resin and metal was taken to be planar, and the direction normal to the interface was set to the z-axis. The resin was modeled to mimic an oligomer of polyglycidylether of *o*-cresol formaldehyde novolac (EP) and polyphenol (PH), and its interaction parameters were determined by referring to all-atom treatments. In the following, we first describe the computational procedures for the coarse-grained MD, and after that, we note the methods for the all-atom calculations.

3.3.1 Coarse-grained MD simulation

The resin was modeled as the KremerGrest model with the chain length $N = 60$ and the segment density $\rho = 1$ [184]. This chain length was chosen by computing the Kuhn length in the all-atom model and keeping the correspondence between the all-atom and coarse-grained treatments. See Appendix 3.6.3 for the procedure to determine N. The segment particles in the chains interact with one another through the FENE-LJ (finite extensible nonlinear elastic potential-Lennard Jones) potential expressed as

$$U = U^{\mathrm{FENE}}(r) + U^{\mathrm{LJ}}(r) \tag{3.9}$$

$$U^{\mathrm{FENE}}(r) = \begin{cases} -\frac{1}{2}kR_0^2 \ln\left[1-\left(\frac{r}{R_0}\right)^2\right], & r \leq R_0 \\ \infty, & r > R_0 \end{cases} \tag{3.10}$$

$$U^{\mathrm{LJ}}(r) = \begin{cases} 4\varepsilon\left[\left\{\left(\frac{\sigma}{r}\right)^{12}-\left(\frac{\sigma}{r}\right)^{6}\right\}-\left\{\left(\frac{\sigma}{r_{\mathrm{cut}}}\right)^{12}-\left(\frac{\sigma}{r_{\mathrm{cut}}}\right)^{6}\right\}\right], & r \leq r_{\mathrm{cut}} \\ 0, & r > r_{\mathrm{cut}} \end{cases} \tag{3.11}$$

where r is the distance between the segments, k is the spring constant, R_0 is the maximum extension of the spring, ε and σ are taken as the units for energy and length, respectively, and r_{cut} is the cutoff length. In our MD, these parameters were adopted from Morita et al: $k = 30.0\varepsilon/\sigma^2$, $R_0 = 3.0\sigma$, $r_{\mathrm{cut}} = 2.0\sigma$, and $0.5\tau^{-1}$ for the inverse friction constant for the Langevin dynamics where τ is the unit of time given by $\sigma(m/\varepsilon)^{1/2}$ and m is the mass of the segment particle taken as unity in the coarse-grained MD [185]. The FENE part is operative only between bonded segments located as neighbors along a chain, and the LJ potential is active among all the segment particles. In the present simulation, the attractive term was retained for the Lennard-Jones component of the interparticle interaction. $\varepsilon/k_{\mathrm{B}}$ is the unit temperature T_0, and it was reported that the glass-transition

Table 3.1: Metal parameters for coarse-grained MD. See Sec. 3.3.2 for the meaning of λ.

Metal	λ	$\varepsilon_{\mathrm{wall}}$ / ε	σ_{wall} / σ
Pt	1.0	2.65	0.401
Al	1.0	1.80	0.407
Al	0.1	0.18	0.407

temperature of the Kremer-Grest model with $20 \leq N \leq 200$ is $T_{\mathrm{g}} = 0.4T_0$ [185].

The metal was treated as a Lennard-Jones wall with the potential $U_{\mathrm{wall}}(z)$ expressed as

$$U_{\mathrm{wall}}(z) = \varepsilon_{\mathrm{wall}} \left[\frac{2}{15} \left(\frac{\sigma_{\mathrm{wall}}}{z} \right)^9 - \left(\frac{\sigma_{\mathrm{wall}}}{z} \right)^3 \right] \tag{3.12}$$

where z is the distance from the wall along the direction normal to the interface, $z = 0$ is the position of the wall, and $\varepsilon_{\mathrm{wall}}$ and σ_{wall} are the interaction strength and length, respectively. They were determined by referring to the all-atom parameters and are listed in Table 3.1. The procedures to obtain $\varepsilon_{\mathrm{wall}}$ and σ_{wall} are described in Appendix 3.6.4.

MD was performed with LAMMPS-31Mar17 [128], and the simulation system was built through the following procedures. A low-density system of $\rho \simeq 0.001$ was first prepared by locating 2,000 chains in a cubic unit cell without metal wall. The Langevin dynamics was then performed over 10^8 steps at a temperature of T_0 and a time step of 0.01τ. In this calculation, the unit cell was gradually reduced in size so that each of the x, y, and z lengths was modified linearly with time to have the z length of 120σ and $\rho = 1$ at the end of run. The periodic boundary condition was employed along the x and y directions with the minimum image convention, and the non-periodic reflective boundary condition was adopted for the z direction; in the reflective boundary condition, a particle is given the reversed velocity (along z) when it comes to the boundary. The next step is to fix the z length of the unit cell and introduce $U_{\mathrm{wall}}(z)$ at both ends of the z boundary. Three systems were actually examined with $\varepsilon_{\mathrm{wall}}$ and σ_{wall} in Table 3.1, and for each system, MD was done at a time step of 0.01τ and a temperature of $0.5T_0$ over 10^8 steps for equilibration and over 3×10^6 for production. $0.5T_0$ was chosen so that the ratio of the simulation temperature to the glass-transition temperature (T_{g}) is identical between the coarse-grained treatment and the all-atom simulation described below.

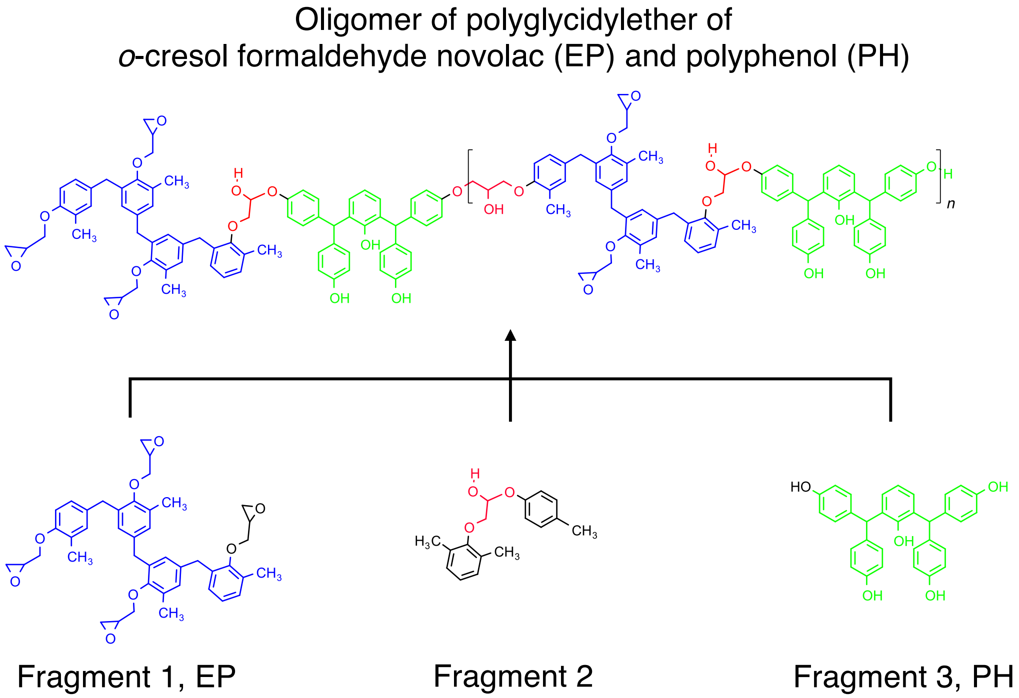

Figure 3.1: Fragment models for determining the atomic charges in the oligomers. The all-atom MD simulations were performed at $n = 7$.

See Appendix 3.6.5 for the determination of T_g. To improve the statistics, the above procedures for coarse-grained MD were repeated 100 times and the results were obtained by averaging over the 100 runs.

3.3.2 All-atom MD simulation

To see the resin-metal interfaces in more details and provide a justification for the coarse-grained modeling, we also conducted all-atom simulations for the resin-metal systems with a variety of adhesion strengths. The resin used in our calculations is an oligomer of polyglycidylether of *o*-cresol formaldehyde novolac (EP) and polyphenol (PH), which is a common thermoset in manufacturing of electronic devices. In a typical process, the mixture of EP and PH are fed as raw materials and polymerize to the chemical structure of Fig. 3.1 by connecting their terminal groups alternately [5, 141–143]. Our simulations adopted $n = 7$. The metals treated were platinum and aluminum of face-centered-cubic (fcc) structure with the (001) plane as the interface.

The force field adopted was Dreiding for the oligomer of EP and PH and the parameters for the metals were taken from Heinz et al [93, 94, 97]. The resin-metal interaction was of Lennard-Jones form written as

$$U_{\mathrm{rm}}(r_{ij}) = 4\varepsilon_{\mathrm{rm}}\left[\left(\frac{\sigma_{\mathrm{rm}}}{r_{ij}}\right)^{12} - \left(\frac{\sigma_{\mathrm{rm}}}{r_{ij}}\right)^{6}\right] \tag{3.13}$$

where $\varepsilon_{\mathrm{rm}}$ and σ_{rm} are the energy and length parameters for the resin-metal interaction, respectively, and r_{ij} is the inter-atomic distance between the ith atom of resin and the jth atom of metal. The electrostatic part is not present in Eq. (3.13) since the metal was treated as an uncharged material. Heinz et al.'s parameters are suitable for simulations of resin (polymer)-metal interface, as reported for such properties as surface tension, interfacial tension, and contact angle [93, 94, 96, 98, 112–116, 118, 120–123]. To further analyze the effect of resin-metal interaction on the adhesion strength, the scaled interaction with aluminum was examined by replacing $\varepsilon_{\mathrm{rm}}$ to $\lambda\varepsilon_{\mathrm{rm}}$ in Eq. (3.13) with $\lambda = 0.1, 0.2$, and 0.5. The resin-aluminum interaction was artificially weakened by this scaling.

The partial charges on the resin were determined from quantum-chemical calculations at B3LYP/6-31G(d,p) level using Gaussian09 package and the restrained electrostatic potential (RESP) procedure [124–126], with the following steps. The geometry optimization in vacuum was conducted for the three fragments shown in Fig. 3.1, and the charges on the fragments were transferred to the resin with the convention of color matching in Fig. 3.1. All the charges thus assigned were then shifted by an equal amount so that the total charge vanishes.

The all-atom MD simulations were also carried out with LAMMPS-31Mar17 [128]. The lengths of the bonds involving a hydrogen atom were constrained by SHAKE [146]. The electrostatic interaction was handled by the particle-particle particle-mesh (PPPM) method with a real-space cutoff of 1.2 nm and a root mean square force accuracy of 10^{-5} [129, 130]. The Lennard-Jones (LJ) interaction was truncated at 1.2 nm without long-range correction, and the periodic boundary condition was adopted with minimum image convention.

The simulated system was set by first building the metal and resin layers separately and then attaching them. The metal layer was a cubic crystal of fcc form with an edge length of 4 nm with

(001) plane facing upward to the positive z direction. A vacuum region of 2.0 nm was added above the layer, and the metal was subject to energy minimization. The resin layer was prepared by first locating 28 resin molecules at a low initial density (0.001 $\mathrm{g/cm^3}$) in a cubic unit cell. The resins were then subject to a 2-step procedure presented next. The first step was a 100-ps MD. The x and y lengths of the unit cell were reduced at a uniform rate to make them equal to those of the metal layer at the end of run, and the z length was modified gradually to reach a unit-cell density of 0.97 $\mathrm{g/cm^3}$. This is the average density at 450 K and 1 bar and was obtained by performing MD for bulk resin through the procedures in Table 2 of Ref. 163 for 10 times. In the second step, MD was carried out in the *NVT* ensemble first at 600 K for 1 ns and further at 450 K for 2 ns. In the 2-step preparation of the resin layer, the equation of motion was solved by the velocity Verlet integrator at a time step of 0.5 fs and the temperature was maintained with the Nosé-Hoover thermostat at coupling constants of 1 and 2 ps, respectively, for the first and second steps [127, 131–134]. The use of 450 K in the above actually corresponds to the practical procedure of curing the resin; see the end of the next paragraph.

The resin-metal interface was built by stacking the resin over the metal along the z direction with a vacuum region of 2.0 nm further above the resin layer. The top of this vacuum region is coincident with the bottom of the metal due to the periodic boundary condition. The next step was to remove the vacuum region through a 500-ps MD conducted at 600 K to gradually reduce the z length of the unit cell of the combined resin-metal system to the sum of those of the resin and metal layers at the final snapshots of their separate preparations. The equilibration and production runs followed with *NVT* MD over 10 ps at a temperature of 600 K and a time step of 0.1 fs and subsequently over 1 ns at 600 K and 0.5 fs. In these MD runs, the Langevin dynamics was employed at an inverse friction constant of 1.0 ps for temperature control [147, 148] and the production part was the last 250 ps. The set of simulations described above was done 20 times, thus 5-ns *NVT* data in total were used for analyses. It should be noted that the resin-metal system was simulated at 600 K after the resin bulk was first prepared at 450 K and was then stacked on the metal by keeping the resin volume at the one at 450 K. This computation scheme corresponds to the common process in manufacturing

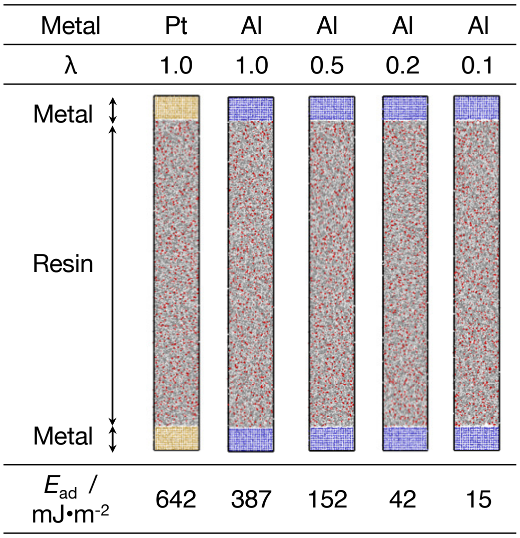

Figure 3.2: Snapshot configurations of the resin-metal systems in the all-atom models and the adhesion energies E_{ad}. See Eq. (3.14) for the definition of E_{ad}.

of electronic devices with thermosets. The thermosets (epoxy resins) are polymerized and cured typically at 450 K, and they are often used in practice at ∼600K to cure other materials [3, 6, 7].

3.4 Results and Discussion

We first describe the strength of adhesion in the all-atom model. Figure 3.2 shows snapshot configurations of the resin-metal systems right after their production runs. In all the systems examined, the resins do not detach from the interface. To assess quantitatively the adhesion strength, we introduce the adhesion energy E_{ad} as

$$E_{\mathrm{ad}} = -\frac{1}{2S_{xy}} \sum_{i,j} U_{\mathrm{rm}}(r_{ij}) \tag{3.14}$$

where U_{rm} is the resin-metal interaction of Eq. (3.13), the sum is taken over all the pairs of resin and metal atoms, and S_{xy} is the area of the MD unit cell over the lateral directions. The right-hand side of Eq. (3.14) is divided by 2 since the metal wall is present both at the upper and lower sides of the resin layer. E_{ad} is listed in Fig. 3.2. It is the largest for platinum interface, and reduces for aluminum

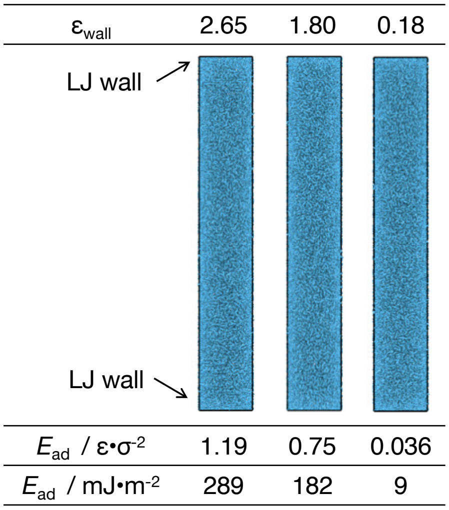

Figure 3.3: Snapshot configurations of the resin-metal systems in the coarse-grained models and the adhesion energies E_{ad}. See Eq. (3.15) for the definition of E_{ad}. The E_{ad} values are also converted to those in the units of $\mathrm{mJ} \cdot \mathrm{m}^{-2}$ using the values of $\varepsilon_{\mathrm{ss}}$ and σ in Appendices 3.6.3 and 3.6.4.

when λ becomes small. The three systems of platinum and aluminum with $\lambda = 1.0$ and 0.5 are of tight adhesion with adhesion energies of more than 10^2 $\mathrm{mJ/m^2}$. These energies are larger than the commonly observed work of adhesion between immiscible resins, which is typically of several tens of $\mathrm{mJ/m^2}$ [186, 187]. Accordingly, the resin-metal interaction overwhelms the interactions among the resins and the tight adhesion is expected when the metal surface is clean, for example, without (unintended) adsorption of an organic compound. E_{ad} for the aluminum with $\lambda = 0.2$ and 0.1 is at the same order of magnitude as the adhesion work of immiscible resins. In fact, these λ's were examined for the purpose of elucidating the effect of the resin-metal interaction strength. The metals used in practice are platinum, aluminum, copper, and gold [3–7], and their interactions with the resins are stronger than the resin-resin interaction [94].

We now turn to analyses with the coarse-grained model. The metal is modeled as a Lennard-Jones wall of Eq. (3.12), and we analyze only the resin part. Although the $\varepsilon_{\mathrm{wall}}$ value examined was 2.65ε, 1.80ε, and 0.18ε, it will be simply written as 2.65, 1.80, and 0.18, respectively, in the following. These $\varepsilon_{\mathrm{wall}}$ correspond to platinum, aluminum at $\lambda = 1.0$, and aluminum at $\lambda = 0.1$ in the all-atom treatment, respectively. To evaluate the strength of adhesion in the coarse-grained model, we adopt the adhesion energy E_{ad} with

$$E_{\mathrm{ad}} = -\frac{1}{2S_{xy}} \sum_i U_{\mathrm{wall}}(z_i) \tag{3.15}$$

where U_{wall} is the resin-wall interaction of Eq. (3.12), z_i is the distance along the z direction from the wall to the ith segment particle, and the sum is taken over all the segments in the resins. Snapshot configurations of the coarse-grained resin-wall systems are depicted in Fig. 3.3 with the values of E_{ad}. In all the systems examined, the resin is adhered to the wall. This is consistent with the results for the resin-metal interface in the all-atom treatment for platinum and aluminum with λ=1.0 and 0.1. It is further observed that E_{ad} grows with $\varepsilon_{\mathrm{wall}}$. As was also seen with the all-atom models, E_{ad} reflects the strength of resin-wall interaction directly. The E_{ad} values expressed in the units of $\mathrm{mJ} \cdot \mathrm{m}^{-2}$ are shown in Fig. 3.3, in addition. When they are compared with the all-atom values in Fig. 3.2, E_{ad} in the coarse-grained model is about half of that in the all-atom model. The interactions are not taken into account when they are in the spatial scales smaller than the size of the segment, which is considered a cause of the smaller E_{ad} in the coarse-grained model.

To study the motion of the segment at the interfacial region, we analyzed the mean-square displacement (MSD) as a function of the normal distance from the wall z . The local MSD of a segment $\phi(t;z)$ is defined as

$$\phi(t;z) = \frac{\langle \sum_i \delta(z - z_i(0))(\mathbf{r}_i(t) - \mathbf{r}_i(0))^2 \rangle}{\langle \sum_i \delta(z - z_i(0)) \rangle} \tag{3.16}$$

where $z_i(t)$ and $\mathbf{r}_i(t)$ are the z-position and the position vector of the ith segment at time t, respectively, and $\langle \cdots \rangle$ refers to the average over the configurations at the initial time ($t = 0$). This expression was proposed by Tanaka et al [154, 185], and Figure 3.4 shows $\phi(t;z)$ as contours of t and z. It is evident that the motion of the segment slows down near the wall when $\varepsilon_{\mathrm{wall}} = 2.65$ or 1.80 and the resin-wall interaction is strong. The effect of the wall extends from the interface to $\sim 20\sigma$ and $\sim 10\sigma$ for $\varepsilon_{\mathrm{wall}} = 2.65$ and 1.80, respectively, and an appreciable growth of MSD is not observed there. The resin then adheres tightly to the wall as evidenced in Fig. 3.3, and in such

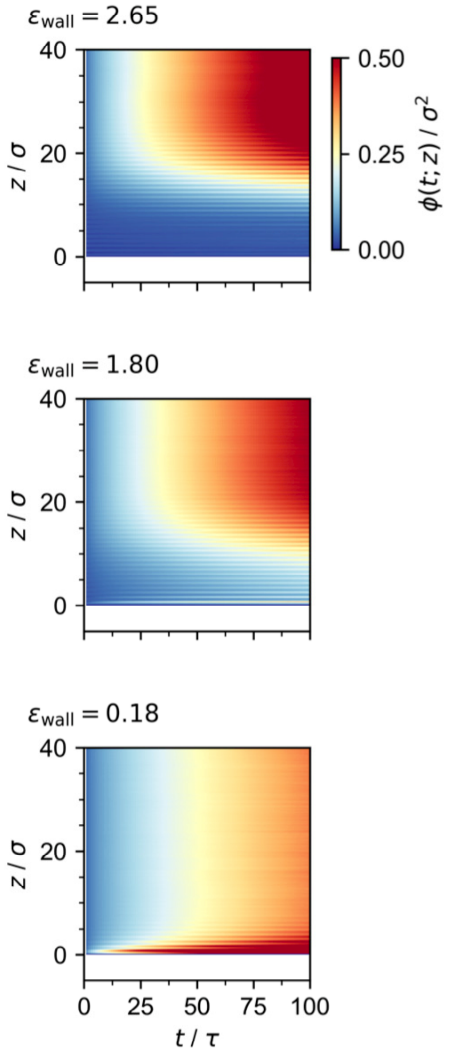

Figure 3.4: Local mean-square displacement of a segment $\phi(t;z)$ as contours of t and z at $\varepsilon_{\mathrm{wall}} =$ 2.65, 1.80, and 0.18 from top to bottom. $z = 0$ refers to the position of the interface, where U_{wall} of Eq. (3.12) is singular. The displayed $\phi(t;z)$ is the average of the values calculated at the upper and lower walls. $\phi(t;z)$ is plotted by discretizing Eq. (3.16) with $\Delta z = 0.1\sigma$ and $\Delta t = 0.01\tau$.

circumstances, the wall acts to retard the motion of the resin. The slowdown of the segment motion at $\varepsilon_{\text{wall}} = 2.65$ or 1.80 is consistent with an increase of T_{g} observed with fluorescence experiment for polystyrene and with results of previous coarse-grained simulations, in which the diffusion was shown to be slower near the wall [154]. $\phi(t;z)$ at $z \lesssim 20\sigma$ is further smaller for $\varepsilon_{\text{wall}} = 2.65$ than for $\varepsilon_{\text{wall}} = 1.80$. This shows that the segment motion is suppressed by the wall more when the resin-wall interaction is stronger. When $\varepsilon_{\text{wall}}$ is 0.18, on the other hand, the deviation of $\phi(t;z)$ from its bulk behavior is localized only within the region of a few σ from the wall and $\phi(t;z)$ in that region is larger than in the bulk. The resin moves fast only around the interface when its interaction with the wall is weak. The motions of resin along the lateral and normal directions to the interface can be separately analyzed, furthermore. See Appendix 3.6.6 for the lateral and normal components of $\phi(t;z)$.

Figure 3.5 depicts the segment density $\rho(z)$. Sharp and crystal-like peaks are present at each $\varepsilon_{\text{wall}}$, showing that the segments are well structured near the wall. As illustrated in the insets, $\rho(z)$ oscillates at a period of σ and the ordering is particularly evident at $\varepsilon_{\text{wall}}$ = 2.65 and 1.80. Since the structure formation is stronger at a larger $\varepsilon_{\text{wall}}$, the attractive interaction between the segment and wall is responsible for the formation of layers. Actually, the density enhancement at the interface was observed for polymer melts and films in previous works, which employed weaker resin-wall interactions than ours and did not exhibit layering structures [154, 185, 188]. The amplitude of oscillation of $\rho(z)$ decays in $\sim 20\sigma$ at $\varepsilon_{\text{wall}} = 2.65$ and 1.80 and in $\sim 5\sigma$ at $\varepsilon_{\text{wall}} = 0.18$. The thickness of the layer is thus larger than the radius of gyration of the resin (2.6σ) and the interaction range between the resin and wall ($\sim 0.4\sigma$ according to Eq. (3.12) and Table 3.1). This suggests that the ordered structure reflects not only the direct, resin-wall interaction but also the resin-resin correlation.

To analyze the spatial inhomogeneity of the equal-time correlation of the stress, $\Gamma^{xz}(t;z)$ is plotted against z at $t = 0$ in Fig. 3.5. The extent of stress fluctuation is connected to $\Gamma^{xz}(0;z)$, and according to Fig. 3.5, $\Gamma^{xz}(0;z)$ oscillates with z at a period of σ and decays to the bulk value in $\sim 20\sigma$ and $\sim 5\sigma$ for $\varepsilon_{\text{wall}} = 2.65$ and 1.80 and for $\varepsilon_{\text{wall}} = 0.18$, respectively. The spatial range of

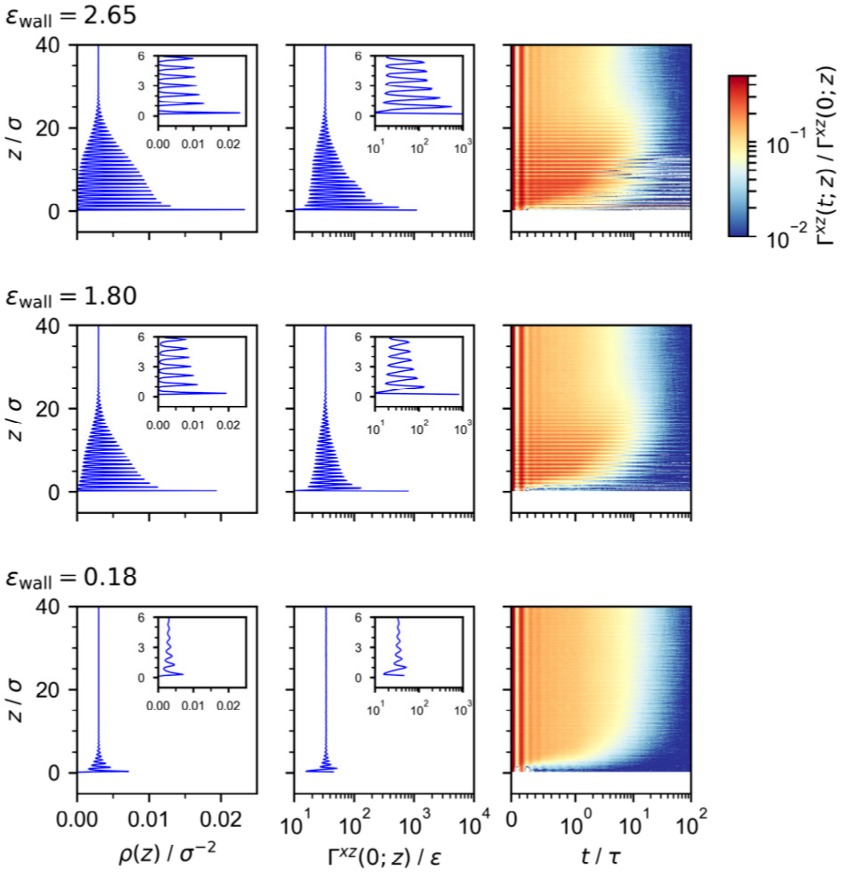

Figure 3.5: Local number density of segments $\rho(z)$ (left), equal-time correlation of the local stress $\Gamma^{xz}(0;z)$ (center), and spatially-decomposed relaxation modulus $\Gamma^{xz}(t;z)$ normalized by $\Gamma^{xz}(0;z)$ (right) at $\varepsilon_{\text{wall}} = 2.65$, 1.80, and 0.18 from top to bottom. $z = 0$ refers to the position of the interface, where U_{wall} of Eq. (3.12) is singular. The displayed $\rho(z)$ and $\Gamma^{xz}(t;z)$ are the averages of the values calculated at the upper and lower walls. The space and time are discretized with $\Delta z = 0.1\sigma$ and $\Delta t = 0.01\tau$, respectively. The graduation for t is linear in $t < \tau$ and is logarithmic in $t > \tau$.

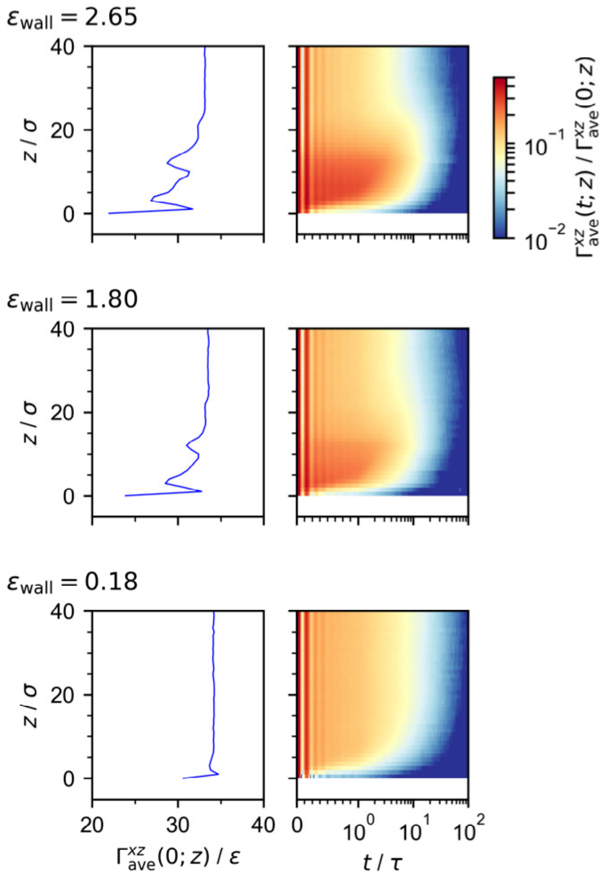

Figure 3.6: Averaged correlation of the stress $\Gamma^{xz}_{\rm ave}(0;z)$ (left) and the decay profile expressed as $\Gamma^{xz}_{\rm ave}(t;z)/\Gamma^{xz}_{\rm ave}(0;z)$ (right) at $\varepsilon_{\rm wall} = 2.65$, 1.80, and 0.18 from top to bottom. $z = 0$ refers to the position of the interface, where $U_{\rm wall}$ of Eq. (3.12) is singular. The displayed $\Gamma^{xz}_{\rm ave}(t;z)$ is the average of the values calculated at the upper and lower walls, and the space and time are discretized with $\Delta z = \sigma$ and $\Delta t = 0.01\tau$, respectively. The graduation for t is linear in $t < \tau$ and is logarithmic in $t > \tau$.

the wall's effect is thus in correspondence between $\Gamma^{xz}(0;z)$ and the density $\rho(z)$, and the amplitude of oscillation of $\Gamma^{xz}(0;z)$ is also larger in the order of $\varepsilon_{\rm wall} = 2.65$, 1.80, and 0.18. The layering of the stress correlation is caused by the resin-wall interaction and is more so when the adhesion is strong. The phase of oscillation is opposite between $\Gamma^{xz}(0;z)$ and $\rho(z)$, though. $\Gamma^{xz}(0;z)$ refers to the local correlation of the stress per particle, and a particle located at z with small $\rho(z)$ tends to be strongly stressed toward stable positions.

To see the local correlation of the stress in the spatial scale corresponding to the segment size, we show in Fig. 3.6 the averaged $\Gamma^{xz}(t;z)$ defined as

$$\Gamma^{xz}_{\text{ave}}(t;z) = \frac{\int_z^{z+\Delta z} dz' \rho(z') \Gamma^{xz}(t;z')}{\int_z^{z+\Delta z} dz' \rho(z')} \tag{3.17}$$

where $\Delta z = \sigma$. $\Gamma^{xz}_{\text{ave}}(t;z)$ is simply the stress-stress correlation function evaluated with a discretization of $\Delta z = \sigma$, which is in turn the thickness of a single layer in the interfacial region and is close to the Kuhn length of our resin model (see the end of Appendix 3.6.3). $\Gamma^{xz}_{\text{ave}}(0;z)$ corresponds to the stress fluctuation for a layer, and stays within a few tens of % from the bulk value. When seen per layer, the equal-time correlation of the stress is not strongly influenced by the formation of the layered structure due to the cancellation of the oscillation within the layer. Actually, the resin is weakly stressed for all the systems examined when the resin is right near the wall and z is within a few σ. The weakening of the stress correlation is further observed up to $\sim 20\sigma$ when $\varepsilon_{\text{wall}} = 2.65$ and 1.80, and reflects the observation in Fig. 3.5 that $\Gamma^{xz}(0;z)$ oscillates in opposite phase with $\rho(z)$. Within each layer, $\Gamma^{xz}(0;z)$ is smaller when $\rho(z)$ is larger. The averaging procedure in Eq. (3.17) then implies that a smaller $\Gamma^{xz}(0;z)$ is weighted more, and accordingly, the resin is less stressed in the interfacial region than in the bulk when examined over the spatial scale corresponding to the layer.

Figure 3.5 also shows $\Gamma^{xz}(t;z)/\Gamma^{xz}(0;z)$ as contours of t and z. For all the systems examined, $\Gamma^{xz}(t;z)/\Gamma^{xz}(0;z)$ in a few σ from the wall decays faster than in the bulk. The stress-stress correlation is shorter-lived near the wall, irrespective of the strength of resin-wall interaction. When $\varepsilon_{\text{wall}} = 2.65$ and 1.80, the correlation enhances in the region from a few σ to $\sim 20\sigma$. This region corresponds to the one with layered structure seen from $\rho(z)$ and also to the region with slowed motion of the resin in Fig. 3.4. The resin at z beyond a few σ keeps the local stress for longer time when it is ordered and moves slowly, and the decay time there is larger than that in $z \gtrsim 20\sigma$. When the resin-wall interaction is weaker and $\varepsilon_{\text{wall}} = 0.18$, the decay of $\Gamma^{xz}(t;z)/\Gamma^{xz}(0;z)$ beyond a few σ from the wall is similar to that in the bulk. The dynamic inhomogeneity can thus be observed when the resin-wall interaction is strong and the layer structure develops to $\sim$10 nm scale (σ corresponds to the Kuhn length of 0.7 nm, as noted in Appendix 3.6.3).

$\Gamma^{xz}_{\mathrm{ave}}(t;z)/\Gamma^{xz}_{\mathrm{ave}}(0;z)$ shown in Fig. 3.6 has common features with $\Gamma^{xz}(t;z)/\Gamma^{xz}(0;z)$ in Fig. 3.5, that involves finer resolution in space. The effect of the density oscillation is absorbed into $\Gamma^{xz}_{\mathrm{ave}}(0;z)$ when the averaging is done over the layers, and the stress-stress correlation function is rather insensitive to the setting of the spatial resolution when it is normalized by the equal-time ($t = 0$) value. To analyze the stress-stress correlation in more details, we depict $\Gamma^{xz}_{\mathrm{ave}}(t;z)/\Gamma^{xz}_{\mathrm{ave}}(0;z)$ at specific z of σ, 10σ, and 50σ in Fig. 3.7. $z = \sigma$ is close to the wall, and $z = 50\sigma$ corresponds to a point in the bulk. $\Gamma^{xz}_{\mathrm{ave}}(t;z)$ decays with oscillation in the short-time region up to several tenths of τ, where τ is defined as $\sigma(m/\varepsilon)^{1/2}$ and corresponds to 68 ps in our model (see the end of Appendix 3.6.4). The local stress oscillates over the ps scale, and the period of oscillation is $\sim 0.1\tau$ for all the cases. The oscillatory behavior of $\Gamma^{xz}_{\mathrm{ave}}(t;z)$ is thus due to the interactions among the resins since the interface does not affect the oscillation period. When $\varepsilon_{\mathrm{wall}}$ is 2.65 or 1.80, the initial decay of $\Gamma^{xz}_{\mathrm{ave}}(t;z)$ is weaker at $z = \sigma$ and 10σ than at $z = 50\sigma$. $\Gamma^{xz}_{\mathrm{ave}}(t;z)$ at $z = \sigma$ decays faster than that in the bulk only after it oscillates a few times. In other words, the resin flows more readily right near the wall when the crystal-like oscillation is damped. $\Gamma^{xz}_{\mathrm{ave}}(t;z)$ at $z = 10\sigma$ does not change appreciably over a duration of $\sim\tau$ after its oscillation becomes indistinct. A plateau is present during the stress-stress relaxation in the middle of the layered structure of the resin adhered strongly to the metal. When $\varepsilon_{\mathrm{wall}}$ is 0.18 and the resin-wall interaction is weak, $\Gamma^{xz}_{\mathrm{ave}}(t;z)$ at $z = \sigma$ decays fast over the whole range of time. We saw in Fig. 3.6 that the equal-time correlation of the local stress is not affected significantly by the wall also at $\varepsilon_{\mathrm{wall}} = 0.18$, and it is revealed in combination with Fig. 3.7 that the resin at the weakly interacting wall is stressed as in the bulk but relaxes easily. The decay profile of $\Gamma^{xz}_{\mathrm{ave}}(t;z)$ is similar between $z = 10\sigma$ and 50σ when $\varepsilon_{\mathrm{wall}} = 0.18$. This is in correspondence to the local MSD shown in Fig. 3.4, and the effect of the interface is not appreciable beyond a few σ.

We lastly discuss the connection between the inhomogeneity in the viscoelasticity and the strength of adhesion. Our simulation showed that the resin located at the interface is mostly more viscous than that in the bulk and relaxes slower when the resin-wall interaction is stronger than the resin-resin. The presence of more viscous regions indicates that the resin at the interface does not

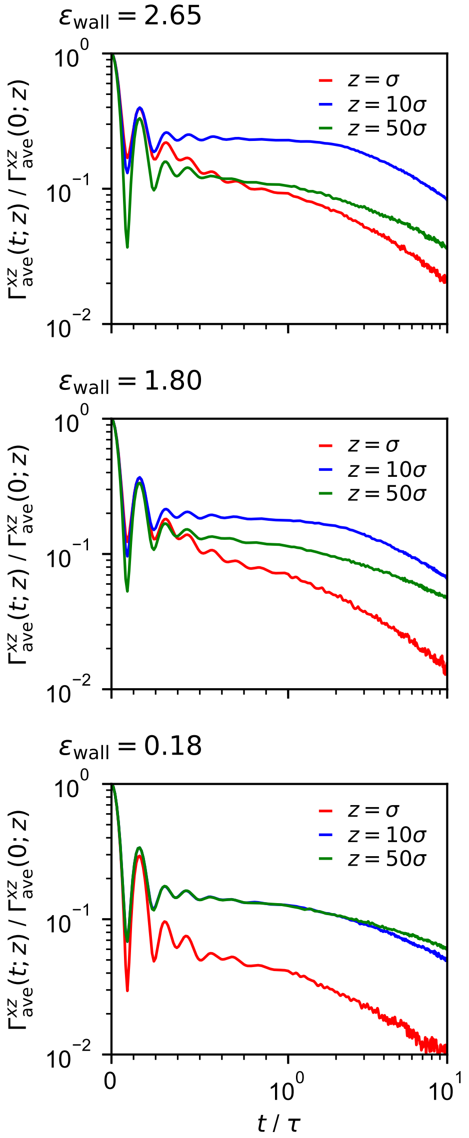

Figure 3.7: $\Gamma^{xz}_{\text{ave}}(t;z)$ normalized by $\Gamma^{xz}_{\text{ave}}(0;z)$ at $z = \sigma$, 10σ, and 50σ against t for $\varepsilon_{\text{wall}} = 2.65$, 1.80, and 0.18 from top to bottom. See Eqs. (3.6) and (3.17) for the definition of $\Gamma^{xz}_{\text{ave}}(t;z)$. The graduation for t is linear in $t < \tau$ and is logarithmic in $t > \tau$.

flow easily by the external stress, and the contact of the resin and metal is kept for longer time. A common approach for improving the adhesion strength is to increase the interaction with the substrate, with the wettability often employed as a measure of interaction strength. Our simulation results suggest, in addition, that an additive can be utilized for better adhesion if it is preferentially located near the interface and makes more viscous the adhesive (resin) there. In practical applications, indeed, an oligomer with high T_g is often mixed to the adhesive for the purpose of modifying the viscoelasticity at the interface [189–193].

3.5 Conclusion

The spatial-decomposition formula was developed for the relaxation modulus. The distance along the normal direction from a planar interface was taken as the spatial coordinate, and the spatially-decomposed relaxation modulus was introduced as the stress-stress time correlation function conditioned by the spatial coordinate. The spatial-decomposition analysis of viscoelasticity was then conducted for a thermoset resin in contact with metal, and coarse-grained MD simulations were carried out using the Kremer-Grest model. When the resin-metal interaction is strong, well-ordered layers of the resin was seen to form over a spatial range that is an order-of-magnitude larger than the segment size of the resin. The motion of the segment is slower in the ordered layers than in the bulk and is faster right near the wall when the interaction with the wall is weak. In the presence of a strong interaction between the resin and wall, in fact, the stress-stress correlations of the resins in the layers decay more slowly compared to the bulk. The equal-time correlation of the local stress in the interfacial region oscillates in opposite phase with the resin density, and when seen over the segment scale, it is not affected significantly by the resin-wall interaction. The resin is thus more viscous in the well-ordered layers in the sense that it has longer decay times against the local stress. When the interaction is weak between the resin and wall, the effect of the interface was evidenced only in the proximate region to the wall and the stress-stress correlation decays faster there. The interaction of the resin with the metal needs to be strong when the viscoelasticity is to be modified, and in such a case, the resin's viscoelasticity is modified over a range which is larger than the size of the resin segment by an order of magnitude.

In the present work, we developed a framework for analyzing the relaxation modulus with spatial resolution and applied it to resin-metal interfaces using a coarse-grained model. The framework is exact and general, and will be applicable to a non-planar interface and a polymer species with crosslinks. In subsequent work, we examine a resin at an interface with nano-sized pores to connect the viscoelastic inhomogeneity with the modifed adhesion by the nano-scale roughening of a metal surface.

3.6 Appendix

3.6.1 On the form of the stress tensor σ_i^{ab}

According to Eq. (3.1), the stress tensor on the ith particle is expressed as a sum of the kinetic contribution and the potential-energy contribution. Equation (3.1) is actually for a two-body potential, and a more general form is presented in this Appendix. The Kremer-Grest model is a two-body potential, while the angle bending, dihedral torsion, and improper torsion are described by potential functions involving more than two atoms. Following the Irving-Kirkwood-Noll (IKN) scheme, the stress tensor σ_i^{ab} is written as [151–153, 194–201]

$$\sigma_i^{ab} = m_i v_i^a v_i^b + \sum_K \left(\sum_{L=1}^{N_K} \frac{1}{n} \sum_{i=1}^{n} r_i^a f_{i,L}^b \right) + \Omega(r_i^a, f_i^b) \tag{3.18}$$

where K counts the type of interaction, N_K is the number of interactions of the Kth type, and the interaction L involves n bodies of $i = 1, \ldots n$. r_i^a is the a-component of the position of the ith atom and $f_{i,L}^b$ is the b-component of the force acting on the ith atom by interaction L. $\Omega(r_i^a, f_i^b)$ is the contribution from the reciprocal-space part in the lattice-sum treatment of the electrostatic interaction and its form for the particle-particle particle-mesh (PPPM) method is given in Ref. 153. The bond-stretching and Lennard-Jones interactions as well as the real-space part of the electrostatic interaction are of two-body, and the angle-bending motion corresponds to $n = 3$. The dihedral and improper torsions are described by potentials with $n = 4$. In Eq. (3.18), the contribution from the n-body interaction is assigned in the equal amount to each atom involved [202], and this is the scheme adopted in *stress/atom* command in LAMMPS-31Mar17 [128, 151–153]. The pressure profile in lipid membrane and the stress distribution in metallic alloys were indeed analyzed by Eq. (3.18) [199, 203–207], while the non-uniqueness of the partitioning of the n-body contribution ($n \geq 3$) was pointed out [208–211].

3.6.2 Introduction of layers in connection to the definition of $\Gamma^{ab}(t;z)$

The interfacial tension is related to the work of adhesion and is expressed as an integral of the difference between the stresses along the normal and lateral directions to the interface. When the interface is taken to span over the xy plane and the system is inhomogeneous along the z direction, the interfacial tension γ is written as

$$\gamma = \int \left[\langle \sigma^{zz}(z) \rangle - \frac{\langle \sigma^{xx}(z) \rangle + \langle \sigma^{yy}(z) \rangle}{2} \right] dz \tag{3.19}$$

where $\sigma^{ab}(z)$ is the ab-component of the stress tensor at position z and $\langle \ldots \rangle$ denotes the ensemble average. When a set of layers are introduced along z, the stress in the Ith layer is defined as

$$\sigma_I^{ab} = \sum_{i \in I} \sigma_i^{ab} \tag{3.20}$$

where σ_i^{ab} is the stress on the ith particle given by Eqs. (3.1) and (3.18) and the sum is taken over the particles belonging to the Ith layer $[z_I : z_I + \Delta z]$. Equation (3.19) then leads to

$$\gamma = \sum_I \left[\langle \sigma_I^{zz} \rangle - \frac{\langle \sigma_I^{xx} \rangle + \langle \sigma_I^{yy} \rangle}{2} \right], \tag{3.21}$$

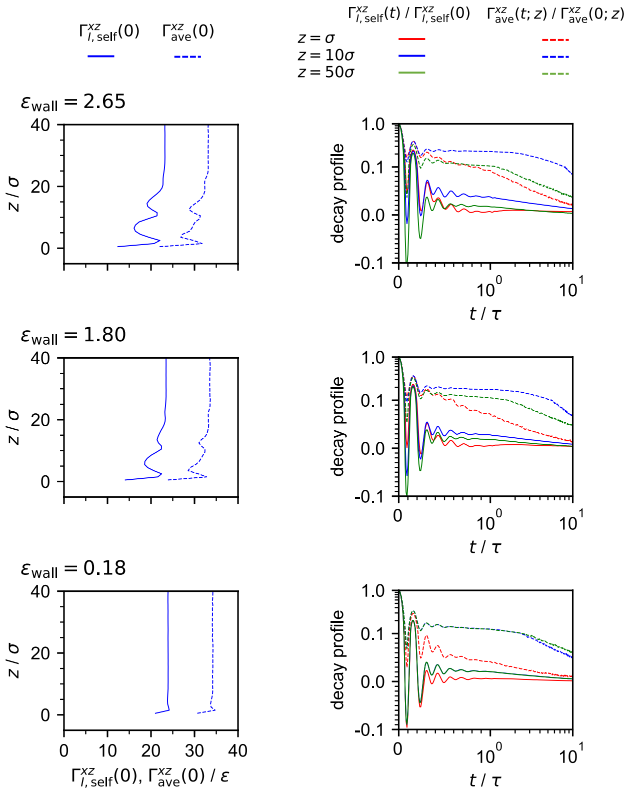

Figure 3.8: Self part of the stress-stress correlation function per particle contained in the Ith layer at time zero $\Gamma^{xz}_{I,\mathrm{self}}(0)$ and the averaged correlation of the stress $\Gamma^{xz}_{\mathrm{ave}}(0;z)$ (left) and the decay profiles expressed as $\Gamma^{xz}_{I,\mathrm{self}}(t)/\Gamma^{xz}_{I,\mathrm{self}}(0)$ and $\Gamma^{xz}_{\mathrm{ave}}(t;z)/\Gamma^{xz}_{\mathrm{ave}}(0;z)$ (right) at $\varepsilon_{\mathrm{wall}} = 2.65$, 1.80, and 0.18 from top to bottom. $z = 0$ refers to the position of the interface, where U_{wall} of Eq. (3.12) is singular. The displayed $\Gamma^{xz}_{I,\mathrm{self}}(t)$ is the average of the values calculated at the upper and lower walls, and the space and time are discretized with $\Delta z = \sigma$ and $\Delta t = 0.01\tau$, respectively. The graduation for t is linear in $t < \tau$ and is logarithmic in $t > \tau$. The ordinate for the right figure is graduated linearly below 0.1 and logarithmically above 0.1. $\Gamma^{xz}_{\mathrm{ave}}(0;z)$ and $\Gamma^{xz}_{\mathrm{ave}}(t;z)/\Gamma^{xz}_{\mathrm{ave}}(0;z)$ in the present figure are the same as those plotted in Figs. 3.6 and 3.7, respectively.

and Eq. (3.2) is rewritten as

$$G^{xz}(t) = \frac{1}{k_BTV}\sum_I \left[\langle \sigma_I^{xz}(0)\sigma_I^{xz}(t)\rangle + \langle \sigma_I^{xz}(0)\sum_{J\neq I}\sigma_J^{xz}(t)\rangle \right]. \tag{3.22}$$

It should be noted that while only a single sum over I is involved in Eq. (3.21), the double sum over I and J appear in Eq. (3.22). Although the interfacial tension γ of Eq. (3.19) is linear in σ_i^{ab}, the relaxation modulus $G^{ab}(t)$ of Eq. (3.2) is quadratic as required by the linear-response theory.

Equation (3.22) provides a decomposition of $G^{xz}(t)$ into the contributions from the layers.

Within the bracket, the time correlation function of the stress within the Ith layer and that between distinct layers are involved. Due to the presence of the double-sum term, $G^{xz}(t)$ is not given by the sum of $\langle \sigma_I^{xz}(0)\sigma_I^{xz}(t)\rangle$ over I. $\langle \sigma_I^{xz}(0)\sigma_I^{xz}(t)\rangle$ is the self part of the correlation within the Ith layer, and is not sufficient to determine the observable, relaxation modulus $G^{xz}(t)$.

It may still be of physical appeal to examine the self part of the stress-stress correlation function per particle contained in the Ith layer defined as

$$\Gamma_{I,\mathrm{self}}^{xz}(t) = \frac{\langle \sigma_I^{xz}(0)\sigma_I^{xz}(t)\rangle}{N_I} \tag{3.23}$$

where N_I is the average number of particles in the Ith layer. The layer width Δz was taken to be σ as in Fig. 3.6, and Fig. 3.8 shows the zero-time component $\Gamma_{I,\mathrm{self}}^{xz}(0)$ and the decay profile $\Gamma_{I,\mathrm{self}}^{xz}(t)/\Gamma_{I,\mathrm{self}}^{xz}(0)$ for $\varepsilon_{\mathrm{wall}}$= 2.65, 1.80, and 0.18. At each $\varepsilon_{\mathrm{wall}}$ and z, $\Gamma_{I,\mathrm{self}}^{xz}(0)$ is smaller than $\Gamma_{\mathrm{ave}}^{xz}(0;z)$ in Fig. 3.6, implying that the interactions among different layers enhance the stress cooperatively. Actually, the z dependence is similar between $\Gamma_{I,\mathrm{self}}^{xz}(0)$ and $\Gamma_{\mathrm{ave}}^{xz}(0;z)$, and their difference is mainly a constant shift. Figure 3.8 further compares the decay profiles of $\Gamma_{I,\mathrm{self}}^{xz}(t)/\Gamma_{I,\mathrm{self}}^{xz}(0)$ and $\Gamma_{\mathrm{ave}}^{xz}(t;z)/\Gamma_{\mathrm{ave}}^{xz}(0;z)$ at $z = \sigma$, 10σ, and 50σ. It is seen that the former decays faster with stronger oscillation for each set of $\varepsilon_{\mathrm{wall}}$ and z. $\Gamma_{I,\mathrm{self}}^{xz}(t)/\Gamma_{I,\mathrm{self}}^{xz}(0)$ can change its sign within several tenths of τ, and the oscillation along the t axis is suppressed when the contributions from distinct layers are incorporated. $\Gamma_{I,\mathrm{self}}^{xz}(t)/\Gamma_{I,\mathrm{self}}^{xz}(0)$ and $\Gamma_{\mathrm{ave}}^{xz}(t;z)/\Gamma_{\mathrm{ave}}^{xz}(0;z)$ have common features in terms of the z dependencies, on the other hand. The stress-stress correlation decays faster near the wall than in the bulk at each $\varepsilon_{\mathrm{wall}}$, and persists over longer times in the well-ordered regions evidenced in Fig. 3.5 when $\varepsilon_{\mathrm{wall}}$ = 2.65 or 1.80. The interactions among the resins belonging to distinct layers thus affect the t dependence of the decay profile mainly.

3.6.3 Procedure to determine the number of segments N

In our coarse-grained simulation, the number of segments N was set by

$$\frac{N\sigma}{l_{\mathrm{K}}^{\mathrm{CG}}} = \frac{\sum_I N_{b,I}^{\mathrm{main}} b_I}{l_{\mathrm{K}}^{\mathrm{AA}}} \tag{3.24}$$

where $l_{\mathrm{K}}^{\mathrm{CG}}$ and $l_{\mathrm{K}}^{\mathrm{AA}}$ are the Kuhn lengths in the coarse-grained and all-atom models, respectively, b_I is the equilibrium length of the Ith bond in the main chain defined in Fig. 3.9, and $N_{b,I}^{\mathrm{main}}$ is the number of Ith type bonds. The main chain in Fig. 3.9 corresponds to the shortest path connecting the terminals, and $l_{\mathrm{K}}^{\mathrm{AA}}$ was evaluated from the end-to-end distance of the main chain through

$$l_{\mathrm{K}}^{\mathrm{AA}} = \frac{\langle R^2 \rangle}{\sum_I N_{b,I}^{\mathrm{main}} b_I} \tag{3.25}$$

where R is the instantaneous value of the end-to-end distance and the denominator refers to the length of the fully stretched chain of the resin. To obtain $\langle R^2 \rangle$, we carried out a 1-ns MD of bulk resin at 600 K and a time step of 0.5 fs; the initial configuration was prepared through the procedure for the bulk resin in Sec. 3.3.2 (before being stacked on the metal). The first 500 ps of the 1-ns run was for equilibration and the last 500 ps was used to evaluate $\langle R^2 \rangle$. This simulation was repeated 50 times, and we obtained $l_{\mathrm{K}}^{\mathrm{AA}} = 0.66$ nm.

The Kuhn length in the coarse-grained model $l_{\mathrm{K}}^{\mathrm{CG}}$ was calculated through

$$l_{\mathrm{K}}^{\mathrm{CG}} = \frac{\langle R^2 \rangle}{N b^{\mathrm{CG}}} = \frac{N (b^{\mathrm{CG}})^2}{N b^{\mathrm{CG}}} = b^{\mathrm{CG}} \tag{3.26}$$

where b^{CG} is the equilibrium distance between the neighboring segments in the chain and $N(b^{\mathrm{CG}})^2$ is the analytic expression for the end-to-end distance of a freely jointed chain [212]. $b^{\mathrm{CG}} \approx 0.94\sigma$ is the distance corresponding to the minimum of the FENE-LJ potential of Eq. (3.9), and we employed $N = 60$ (by rounding off the first digit) as the number of segments.

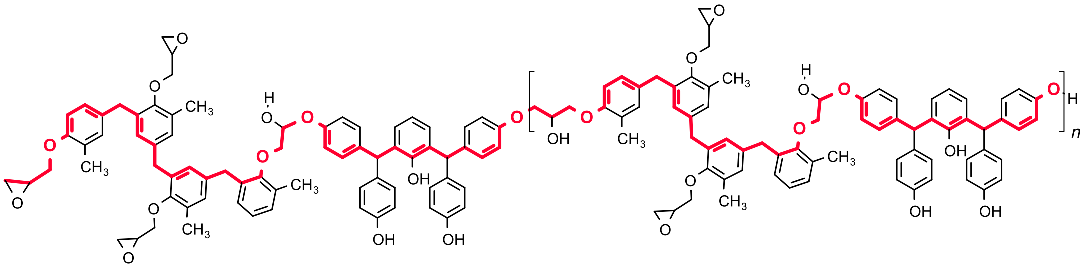

Figure 3.9: Definition of the main chain of the resin. The red color represents the main chain, and $n = 7$.

3.6.4 Procedure to determine $\varepsilon_{\mathrm{wall}}$ and σ_{wall}

$\varepsilon_{\mathrm{wall}}$ and σ_{wall} of Eq. (3.12) were set by referring to the Kuhn length for the all-atom model determined in Appendix 3.6.3. Let N_I^{s} be the number of Ith type atoms contained per segment. It is expressed as

$$N_I^{\mathrm{s}} = N_I \frac{l_{\mathrm{K}}^{\mathrm{AA}}}{\sum_I N_{b,I}^{\mathrm{main}} b_I} \tag{3.27}$$

where N_I is the total number of Ith type atoms in the resin molecule. The effective energy parameter $\varepsilon_{\mathrm{ss}}$ for the interaction between the neighboring segments α and β is then given by

$$\varepsilon_{\mathrm{ss}} = \sum_{i\in\alpha}\sum_{j\in\beta} \varepsilon_{ij} = \sum_I \sum_J N_I^{\mathrm{s}} N_J^{\mathrm{s}} \varepsilon_{IJ} \tag{3.28}$$

where i and j refer to the ith atom in segment α and the jth atom in segment β, respectively, ε_{IJ} is the Lennard-Jones energy parameter between the Ith type and Jth type atoms, and the sums over I and J are taken within segments α and β, respectively. At coarse-graining, the metal part is regarded as a uniform medium that occupies the region of $z < 0$. In this setup, the interaction potential of an Ith type atom located at z is

$$\begin{aligned} U_{\mathrm{rw},I}(z) &= \rho_{\mathrm{m}} \int_{Z<0} dX\,dY\,dZ\,U_{\mathrm{rm}}\left(\sqrt{X^2+Y^2+(Z-z)^2}\right) \\ &= \varepsilon_{\mathrm{rw},I}\left[\frac{2}{15}\left(\frac{\sigma_{\mathrm{rm},I}}{z}\right)^9 - \left(\frac{\sigma_{\mathrm{rm},I}}{z}\right)^3\right] \end{aligned} \tag{3.29}$$

$$\varepsilon_{\mathrm{rw},I} = \frac{2}{3}\pi\lambda\rho_{\mathrm{m}}(\sigma_{\mathrm{rm},I})^3\varepsilon_{\mathrm{rm},I} \tag{3.30}$$

where $\varepsilon_{\mathrm{rm},I}$ and $\sigma_{\mathrm{rm},I}$ are the Lennard-Jones energy and length parameters of Eq. (3.13) for the Ith type atom of the resin with the metal atom, respectively. ρ_{m} is the number density of the metal and is 66 and 60 nm^{-3} for platinum and aluminum, respectively. Eq. (3.29) is of the form of Eq. (3.12), and $\varepsilon_{\mathrm{rw},I}$ is the coarse-grained parameter for the interaction of the Ith type atom with the metal wall. When the resin is further coarse-grained, the segment-wall interaction $\varepsilon_{\mathrm{sw}}$ is a sum of the interactions between the atoms in the segment and the metal wall. $\varepsilon_{\mathrm{sw}}$ is then written with a sum over the atoms in a segment as

$$\varepsilon_{\mathrm{sw}} = \lambda\sum_I N_I^{\mathrm{s}}\varepsilon_{\mathrm{rw},I} \tag{3.31}$$

and $\varepsilon_{\mathrm{wall}}$ of Eq. (3.12) was determined by keeping the ratio of the segment-segment and segment-wall interactions through

$$\varepsilon_{\mathrm{wall}} = \frac{\varepsilon_{\mathrm{sw}}}{\varepsilon_{\mathrm{ss}}} = \lambda\frac{\sum_I N_I^{\mathrm{s}}\varepsilon_{\mathrm{rw},I}}{\sum_I\sum_J N_I^{\mathrm{s}}N_J^{\mathrm{s}}\varepsilon_{IJ}}. \tag{3.32}$$

In our treatment, $\varepsilon_{\mathrm{wall}}$ becomes smaller when the number of atoms in the segment increases with a higher degree of coarse-graining. Indeed, the effect of the wall will be weaker when the segment is taken to be larger.

σ_{wall} of Eq. (3.12) was determined from

$$\frac{\sigma_{\mathrm{wall}}}{l_{\mathrm{K}}^{\mathrm{CG}}} = \frac{1}{l_{\mathrm{K}}^{\mathrm{AA}}}\frac{\sum_I N_I^{\mathrm{s}}\sigma_{\mathrm{rm},I}}{\sum_I N_I^{\mathrm{s}}} \tag{3.33}$$

where N_I^{S} was defined by Eq. (3.27) and the sums over I correspond to the atoms in a segment. The right-hand side is the all-atom value for the averaged $\sigma_{\mathrm{rm},I}$ within a segment divided by the Kuhn length. According to Eq. (3.33), the ratio of the length parameter for the resin-metal interaction to the Kuhn length is in correspondence between the all-atom and coarse-grained models. In addition, the mass m of the segment in the all-atom model is 157.3 g/mol. The unit time τ defined as $\sigma(m/\varepsilon)^{1/2}$ is then 68 ps since ε corresponds to $\varepsilon_{\mathrm{ss}}$ of Eq. (3.28) in the all-atom treatment and σ is the Kuhn length divided by $\sim$0.94 as described at the end of Appendix 3.6.3.

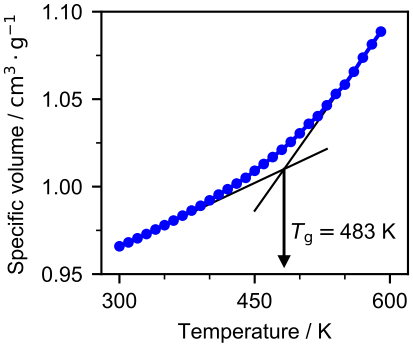

Figure 3.10: Specific volume as a function of temperature.

3.6.5 Procedure to determine T_g of the resin in the all-atom model

The glass-transition temperature of the resin in the all-atom model T_g was obtained from the temperature dependence of the specific volume by conducting a series of simulations with varied temperature. The bulk-resin system prepared with the procedure in Sec. 3.3.2 (before being stacked on the metal) was cooled down from 600 to 300 K at 1 bar using the Nosé-Hoover thermostat and barostat at coupling constants of 1 and 2 ps, respectively. The temperature was reduced at a step of 10 K, and MD was done for 1 ns at each temperature. The specific volume was computed in the last 500 ps, with the first 500 ps discarded as the equilibration period. The above procedures were repeated 30 times, and the averaged specific volume is depicted in Fig. 3.10. T_g was then determined to be 483 K as the intersection of the two lines fitted in the low (from 300 to 400 K) and high (from 500 to 600 K) temperatures. The temperature of the production run T_{prod} was set to keep the ratio of T_{prod} and T_g between the all-atom and coarse-grained treatments, and $T_{prod} = 0.5T_0$ in the coarse-grained simulation.

3.6.6 Components of $\phi(t;z)$ along the lateral and normal directions to the resin-metal interface

To analyze the extent of anisotropy of the segment motion, Eq. (3.16) was decomposed into the lateral and normal components with respect to the resin-metal interface. The lateral and normal components are defined respectively as

$$\phi^l(t;z) = \frac{1}{2}\frac{\langle \sum_i \delta(z - z_i(0))\{(x_i(t) - x_i(0))^2 + (y_i(t) - y_i(0))^2\}\rangle}{\langle \sum_i \delta(z - z_i(0))\rangle} \tag{3.34}$$

and

$$\phi^n(t;z) = \frac{\langle \sum_i \delta(z - z_i(0))(z_i(t) - z_i(0))^2\rangle}{\langle \sum_i \delta(z - z_i(0))\rangle} \tag{3.35}$$

where $x_i(t)$, $y_i(t)$, and $z_i(t)$ are the x, y, and z positions of the segment at time t, respectively, and ϕ^l is expressed as an (average) quantity for a single direction of x or y. Figure 3.11 shows $\phi^l(t;z)$ and $\phi^n(t;z)$ as contours of t and z. It is seen that $\phi^n(t;z)$ is similar to $\phi^l(t;z)$ for each $\varepsilon_{\text{wall}}$, and the motion of the segment is isotropic irrespective of the strength of the segment-wall interaction and the separation from the wall z.

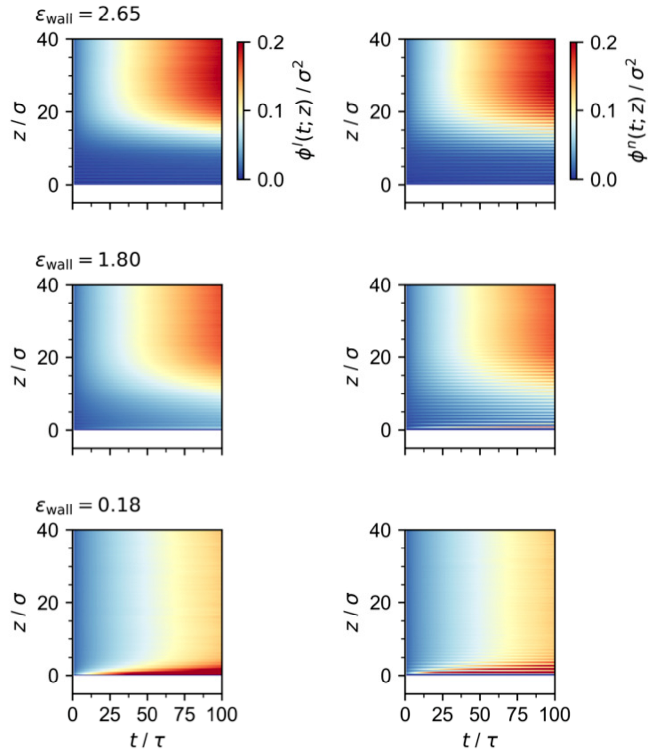

Figure 3.11: $\phi^l(t;z)$ (left) and $\phi^n(t;z)$ (right) as contours of t and z at $\varepsilon_{\text{wall}}$ = 2.65, 1.80, and 0.18 from top to bottom. $z = 0$ refers to the position of the interface, where U_{wall} of Eq. (3.12) is singular. $\phi^l(t;z)$ and $\phi^n(t;z)$ are discretized with $\Delta z = 0.1\sigma$ and $\Delta t = 0.01\tau$.

General Conclusion

We analyzed the filling of epoxy resin into nano-sized pores and the local viscoelasticity at the resin-metal interface by MD simulations. As a result, the following findings were obtained.

Resin filling into nano-sized pores

In Chapter 1, all-atom MD simulation was carried out for the filling of epoxy resin over a variety of degrees of oligomerization into the nano-sized pore. To see the relationship between the extent of filling and the molecular size of the resin with the pushing rate in reality, the MD was conducted at a pushing rate comparable to the experimental. It was shown that a small resin penetrates into the pore along the wall and the filling proceeds uniformly against the pore when the radius of gyration of resin becomes large. When the molecular size exceeds half of the pore size, the density in the pore does not reach half the bulk due to the deformation of the pore.

To obtain more universal guidelines for efficient filling, we analyzed a wide variety of pore and molecular sizes for cylindrical pores in Chapter 2. In Chapter 2, we further monitored the pushing pressure to see the relationship between the extent of filling and the pushing pressure. When the resin was smaller than 1/10 of the pores, the pore was filled beyond half of the bulk at a practical filling pressure. It was further observed that the larger resin can fill the pore by applying a much higher pushing pressure.

Viscoelastic inhomogeneity at the resin-metal interface

In Chapter 3, the spatially decomposed formula was presented for the relaxation modulus and applied it to the resin-metal interface. In this formula, the stress-stress time correlation is conditioned by the distance from the interface to analyze the planar resin-metal interface. When the adhesion energy was large, a layered structure was formed in the vicinity of the interface, which was much larger scale than the segment. We showed that the motion of the resin near the interface is slow and the resin is more viscous in the layered structure. The resin at the interface thus does not flow easily by the external stress, which indicates that the contact of the resin and metal is kept for longer time. A common approach for improving the adhesion strength is to increase the interaction with the substrate, and our simulation results suggest that the modification of viscoelasticity at the interface is an effective approach to obtain good adhesion.

Perspective

Our filling simulation provides a new insight into the design of the attachment process of electronic devices. We showed that the resin should be 1/10 smaller than the pore to achieve good filling via MD simulation. This result indicates that the balance of filling speed and curing speed of the adhesive and the degree of oligomerization of the uncured resin become important design parameters. In addition, the filling pressure does not affect the extent of filling of large resins in a practical range. This suggests that raising the filling pressure is not an effective approach for incomplete filling situations.

For a more universal guideline for efficient filling, it is desirable to simulate not only the filling rate but also the waiting time after filling. In a typical encapsulation process, the pressure is maintained after reaching a certain pressure. Although the resin treated in our simulation is expected to penetrate into the pores at pressures that are not available in industrial practice, the filling can be facilitated simply by reducing the pushing speed. The longer simulation is required to simulate this process, and thus coarse-grained simulation is effective to reduce the calculation cost.

In addition, the spatially decomposed formula for the relaxation modulus is applicable to fields other than adhesion. This method can be extended to a physical property described by time correlation functions such as thermal conductivity and dielectric constant. An example is a highly thermally conductive material used as a heat dissipator for electronic devices, which is composed of a polymer and a thermally conductive substance, such as alumina and boron nitride. In those composite materials, heat dissipation at the interface is often an issue, therefore extending the framework of the spatially decomposed formulation may lead to the development of a new heat dissipation material.

References

[1] W. Ribbens, Understanding automotive electronics: an engineering perspective, Butterworth-heinemann, 2017.

[2] A. Fandakov, A Phenomenological Knock Model for the Development of Future Engine Concepts, Springer, 2018.

[3] M. Brunnbauer, E. Fürgut, G. Beer, T. Meyer, Embedded wafer level ball grid array (ewlb), in: 2006 8th Electronics Packaging Technology Conference, IEEE, 2006, pp. 1–5.

[4] Y. Li, C. P. Wong, Recent advances of conductive adhesives as a lead-free alternative in electronic packaging: Materials, processing, reliability and applications, Materials Science and Engineering R: Reports 51 (1-3) (2006) 1–35.

[5] D. Lu, C. Wong (Eds.), Materials for Advanced Packaging, Springer US, 2009.

[6] M. Töpper, T. Fischer, T. Baumgartner, H. Reichl, A comparison of thin film polymers for wafer level packaging, in: 2010 Proceedings 60th Electronic Components and Technology Conference (ECTC), IEEE, 2010, pp. 769–776.

[7] V. S. Rao, C. T. Chong, D. Ho, D. M. Zhi, C. S. Choong, S. L. PS, D. Ismael, Y. Y. Liang, Development of high density fan out wafer level package (hd fowlp) with multi-layer fine pitch rdl for mobile applications, in: 2016 IEEE 66th Electronic Components and Technology Conference (ECTC), IEEE, 2016, pp. 1522–1529.

[8] S. Yoshitugu, Assembly technologies of double-sided cooling power modules (2009).

[9] H. Naohiko, M. Kuniaki, O. Tomomi, Structural development of double-sided cooling power modules (2009).

[10] D. H. CORPORATION, Structure of manifold absolute pressure sensor, https://www.denso-hokkaido.co.jp/product/product03.html (2019).

[11] A. Biswas, A. Emadi, Energy management systems for electrified powertrains: State-of-the-art review and future trends, IEEE Transactions on Vehicular Technology.

[12] M. Ooi, Future trend in i&m: The smarter car, IEEE Instrumentation & Measurement Magazine 22 (2) (2019) 33–34.

[13] F. Zhao, T. N. Asmus, D. N. Assanis, J. E. Dec, J. A. Eng, P. M. Najt, Homogeneous charge compression ignition (hcci) engines, Tech. rep., SAE Technical Paper (2003).

[14] I.-K. Sung, M. Mitchell, D.-P. Kim, P. J. Kenis, Tailored macroporous sicn and sic structures for high-temperature fuel reforming, Advanced Functional Materials 15 (8) (2005) 1336–1342.

[15] A. Ersoz, H. Olgun, S. Ozdogan, Reforming options for hydrogen production from fossil fuels for pem fuel cells, Journal of Power sources 154 (1) (2006) 67–73.

[16] M. Alias, A. Hairuddin, M. Hassan, K. Rezali, A review of hydrogen addition in an hcci engine fueled with biofuels, in: AIP Conference Proceedings, Vol. 2059, AIP Publishing, 2019, p. 020045.

[17] R. W. Johnson, J. L. Evans, P. Jacobsen, J. R. Thompson, M. Christopher, The changing automotive environment: high-temperature electronics, IEEE transactions on electronics packaging manufacturing 27 (3) (2004) 164–176.

[18] Z. Liang, Status and trend of automotive power packaging, in: 2012 24th International Symposium on Power Semiconductor Devices and ICs, IEEE, 2012, pp. 325–331.

[19] E. automobile industry, Average vehicle age, https://www.acea.be/statistics/article/average-vehicle-agel (2019).

[20] S. Zhou, J. Zhou, Y. Zhu, Chemical composition and size distribution of particulate matters from marine diesel engines with different fuel oils, Fuel 235 (2019) 972–983.

[21] J. Venables, Adhesion and durability of metal-polymer bonds, Journal of Materials Science 19 (8) (1984) 2431–2453.

[22] R. J. Good, Contact angle, wetting, and adhesion: a critical review, Journal of Adhesion Science and Technology 6 (12) (1992) 1269–1302.

[23] E. Liston, L. Martinu, M. Wertheimer, Plasma surface modification of polymers for improved adhesion: a critical review, Journal of Adhesion Science and Technology 7 (10) (1993) 1091–1127.

[24] R. Maboudian, R. T. Howe, Critical review: Adhesion in surface micromechanical structures, Journal of Vacuum Science and Technology B 15 (1) (1997) 1–20.

[25] F. Awaja, M. Gilbert, G. Kelly, B. Fox, P. J. Pigram, Adhesion of polymers, Progress in Polymer Science 34 (9) (2009) 948–968.

[26] M. Shanahan, A. Carre, Viscoelastic dissipation in wetting and adhesion phenomena, Langmuir 11 (4) (1995) 1396–1402.

[27] A. Gent, Adhesion and strength of viscoelastic solids. is there a relationship between adhesion and bulk properties, Langmuir 12 (19) (1996) 4492–4496.

[28] C. Creton, J. Hooker, K. R. Shull, Bulk and interfacial contributions to the debonding mechanisms of soft adhesives: extension to large strains, Langmuir 17 (16) (2001) 4948–4954.

[29] L. Léger, C. Creton, Adhesion mechanisms at soft polymer interfaces, Philosophical Transactions of the Royal Society of London, Series A: Mathematical, Physical and Engineering Sciences 366 (1869) (2008) 1425–1442.

[30] J. D. Venables, Adhesion and durability of metal-polymer bonds, Journal of Materials Science 19 (8) (1984) 2431–2453.

[31] S. O'kell, T. Henshaw, G. Farrow, M. Aindow, C. Jones, Effects of low-power plasma treatment on polyethylene surfaces, Surface and interface analysis 23 (5) (1995) 319–327.

[32] S. Wu, E. Kang, K. Neoh, H. Han, K. Tan, Surface modification of poly (tetrafluoroethylene) films by graft copolymerization for adhesion improvement with evaporated copper, Macromolecules 32 (1) (1999) 186–193.

[33] I. Watanabe, K. S. Kurtz, J. L. Kabcenell, T. Okabe, Effect of sandblasting and silicoating on bond strength of polymer-glass composite to cast titanium., The Journal of prosthetic dentistry 82 (4) (1999) 462–467.

[34] E. Dayss, G. Leps, J. Meinhardt, Surface modification for improved adhesion of a polymer-metal compound, Surface and Coatings Technology 116-119 (1999) 986–990.

[35] E.-Y. Kim, J.-S. Kong, S.-K. An, H.-D. Kim, Surface modification of polymers and improvement of the adhesion between evaporated copper metal film and a polymer. i. chemical modification of pet, Journal of Adhesion Science and Technology 14 (9) (2000) 1119–1130.

[36] P. Molitor, V. Barron, T. Young, Surface treatment of titanium for adhesive bonding to polymer composites: a review, International Journal of Adhesion and Adhesives 21 (2) (2001) 129–136.

[37] P. Laurens, S. Petit, F. Arefi-Khonsari, Study of pet surfaces after laser or plasma treatment: surface modifications and adhesion properties towards al deposition, Plasmas and Polymers 8 (4) (2003) 281–295.

[38] M. Charbonnier, M. Romand, Polymer pretreatments for enhanced adhesion of metals deposited by the electroless process, International journal of adhesion and adhesives 23 (4) (2003) 277–285.

[39] J. Friedrich, G. Kühn, R. Mix, W. Unger, Formation of plasma polymer layers with functional groups of different type and density at polymer surfaces and their interaction with al atoms, Plasma Processes and Polymers 1 (1) (2004) 28–50.

[40] A. Baldan, Adhesively-bonded joints and repairs in metallic alloys, polymers and composite materials: Adhesives, adhesion theories and surface pretreatment, Journal of Materials Science 39 (1) (2004) 1–49.

[41] S. H. Kim, S. W. Na, N. E. Lee, Y. W. Nam, Y. H. Kim, Effect of surface roughness on the adhesion properties of Cu/Cr films on polyimide substrate treated by inductively coupled oxygen plasma, Surface and Coatings Technology 200 (7) (2005) 2072–2079.

[42] V. Kotál, V. Švorčík, P. Slepička, P. Sajdl, O. Bláhová, P. Šutta, V. Hnatowicz, Gold coating of poly (ethylene terephthalate) modified by argon plasma, Plasma Processes and Polymers 4 (1) (2007) 69–76.

[43] B. Finke, F. Luethen, K. Schroeder, P. D. Mueller, C. Bergemann, M. Frant, A. Ohl, B. J. Nebe, The effect of positively charged plasma polymerization on initial osteoblastic focal adhesion on titanium surfaces, Biomaterials 28 (30) (2007) 4521–4534.

[44] B. A. Nemirovskii, A. D. Eselev, Effect of metal-surface preparation on adhesive strength, Polymer Science. Series D 3 (1) (2010) 68–69.

[45] M. Naritomi, N. Andoh, Stainless steel composite and manufacturing method thereof, US Patent App. 12/597319.

[46] M. Naritomi, N. Ando, Metal and resin composite and manufacturing method thereof, US Patent App. 12/669143.

[47] M. Naritomi, N. Andoh, Metal-resin complex and process for production thereof, US Patent 9166212.

[48] D. D. Saperstein, L. J. Lin, Improved surface adhesion and coverage of perfluoropolyether lubricants following far-uv irradiation, Langmuir 6 (9) (1990) 1522–1524.

[49] D. Hegemann, H. Brunner, C. Oehr, Plasma treatment of polymers for surface and adhesion improvement, Nuclear instruments and methods in physics research section B: Beam interactions with materials and atoms 208 (2003) 281–286.

[50] A. Oláh, H. Hillborg, G. J. Vancso, Hydrophobic recovery of uv/ozone treated poly (dimethylsiloxane): adhesion studies by contact mechanics and mechanism of surface modification, Applied Surface Science 239 (3-4) (2005) 410–423.

[51] R. D. Priestley, C. J. Ellison, L. J. Broadbelt, J. M. Torkelson, Structural relaxation of polymer glasses at surfaces, interfaces, and in between, Science 309 (5733) (2005) 456–459.

[52] Z. Jiang, H. Kim, X. Jiao, H. Lee, Y.-J. Lee, Y. Byun, S. Song, D. Eom, C. Li, M. Rafailovich, et al., Evidence for viscoelastic effects in surface capillary waves of molten polymer films, Physical Review Letters 98 (22) (2007) 227801.

[53] T. Koga, C. Li, M. Endoh, J. Koo, M. Rafailovich, S. Narayanan, D. Lee, L. Lurio, S. Sinha, Reduced viscosity of the free surface in entangled polymer melt films, Physical Review Letters 104 (6) (2010) 066101.

[54] T. Koga, N. Jiang, P. Gin, M. Endoh, S. Narayanan, L. Lurio, S. Sinha, Impact of an irreversibly adsorbed layer on local viscosity of nanoconfined polymer melts, Physical Review Letters 107 (22) (2011) 225901.

[55] R. L. Leheny, Xpcs: Nanoscale motion and rheology, Current Opinion in Colloid and Interface Science 17 (1) (2012) 3–12.

[56] S.-f. Wang, S. Yang, J. Lee, B. Akgun, D. T. Wu, M. D. Foster, Anomalous surface relaxations of branched-polymer melts, Physical Review Letters 111 (6) (2013) 068303.

[57] H. K. Nguyen, M. Inutsuka, D. Kawaguchi, K. Tanaka, Depth-resolved local conformation and thermal relaxation of polystyrene near substrate interface, Journal of Chemical Physics 146 (20) (2017) 203313.

[58] S. Sugimoto, M. Inutsuka, D. Kawaguchi, K. Tanaka, Reorientation kinetics of local conformation of polyisoprene at substrate interface, ACS Macro Letters 7 (1) (2017) 85–89.

[59] Y. Zhou, Q. He, F. Zhang, F. Yang, S. Narayanan, G. Yuan, A. Dhinojwala, M. D. Foster, Modifying surface fluctuations of polymer melt films with substrate modification, ACS Macro Letters 6 (9) (2017) 915–919.

[60] F. Yang, D. Presto, Y. Pan, K. Liu, L. Zhou, S. Narayanan, Y. Zhu, Z. Peng, M. D. Soucek, M. Tsige, M. D. Foster, Proximity to graphene dramatically alters polymer dynamics, Macromolecules 52 (14) (2019) 5074–5085. doi:10.1021/acs.macromol.9b00317.

[61] T. Miyamae, H. Nozoye, Correlation of molecular conformation with adhesion at alo x/ poly (ethylene terephthalate) interface studied by sum-frequency generation spectroscopy, Applied physics letters 85 (19) (2004) 4373–4375.

[62] T. Kajiyama, K. Tanaka, I. Ohki, S.-R. Ge, J.-S. Yoon, A. Takahara, Imaging of dynamic viscoelastic properties of a phase-separated polymer surface by forced oscillation atomic force microscopy, Macromolecules 27 (26) (1994) 7932–7934.

[63] C. Hsueh, P. F. Becher, E. R. Fuller, S. Langer, W. Carter, Surface-roughness induced residual stresses in thermal barrier coatings: computer simulations, in: Materials science forum, Vol. 308, Trans Tech Publ, 1999, pp. 442–449.

[64] R. Van Tijum, J. T. M. De Hosson, Effects of self-affine surface roughness on the adhesion of metal-polymer interfaces, Journal of materials science 40 (13) (2005) 3503–3508.

[65] D. Diao, A. Kandori, Finite element analysis of the effect of interfacial roughness and adhesion strength on the local delamination of hard coating under sliding contact, Tribology international 39 (9) (2006) 849–855.

[66] H. D. Rowland, A. C. Sun, P. R. Schunk, W. P. King, Impact of polymer film thickness and cavity size on polymer flow during embossing: toward process design rules for nanoimprint lithography, Journal of Micromechanics and Microengineering 15 (12) (2005) 2414.

[67] T. Tofteberg, E. Andreassen, Multiscale simulation of injection molding of parts with low aspect ratio microfeatures, International Polymer Processing 25 (1) (2010) 63–74.

[68] J. Pina-Estany, A. García-Granada, Molecular dynamics simulation method applied to nanocavities replication via injection moulding, International Communications in Heat and Mass Transfer 87 (2017) 1–5.

[69] K. Maghsoudi, R. Jafari, G. Momen, M. Farzaneh, Micro-nanostructured polymer surfaces using injection molding: A review, Materials Today Communications 13 (2017) 126–143.

[70] S. Kisin, J. Božović Vukić, P. G. T. van der Varst, G. de With, C. E. Koning, Estimating the polymer- metal work of adhesion from molecular dynamics simulations, Chemistry of materials 19 (4) (2007) 903–907.

[71] J.-H. Kang, K.-S. Kim, K.-W. Kim, Molecular dynamics study on the effects of stamp shape, adhesive energy, and temperature on the nanoimprint lithography process, Applied Surface Science 257 (5) (2010) 1562–1572.

[72] P.-H. Huang, Molecular dynamics for lateral surface adhesion and peeling behavior of single-walled carbon nanotubes on gold surfaces, Materials Chemistry and Physics 131 (1-2) (2011) 297–305.

[73] M. Uranagase, S. Ogata, K. Tanaka, H. Mori, S. Tajima, Efficient scheme for calculating work of adhesion between a liquid and polymer-grafted substrate, Journal of Chemical Physics 149 (6) (2018) 064703.

[74] T. Semoto, Y. Tsuji, K. Yoshizawa, Molecular understanding of the adhesive force between a metal oxide surface and an epoxy resin, The Journal of Physical Chemistry C 115 (23) (2011) 11701–11708.

[75] S. Ogata, Y. Takahashi, Moisture-induced reduction of adhesion strength between surface oxidized al and epoxy resin: dynamics simulation with electronic structure calculation, The Journal of Physical Chemistry C 120 (25) (2016) 13630–13637.

[76] S. Ogata, M. Uranagase, Unveiling the chemical reactions involved in moisture-induced weakening of adhesion between aluminum and epoxy resin, The Journal of Physical Chemistry C 122 (31) (2018) 17748–17755.

[77] T. Semoto, T. Yamauchi, K. Yoshizawa, Molecular dynamics study on mechanisms of interfacial adhesionbetween polyp-phenylene sulfideand epoxy resin, Journal of The Adhesion Society of Japan 51 (3) (2015) 80–88.

[78] F. Leroy, F. Müller-Plathe, Dry-surface simulation method for the determination of the work of adhesion of solid–liquid interfaces, Langmuir 31 (30) (2015) 8335–8345.

[79] P. L. Freddolino, F. Liu, M. Gruebele, K. Schulten, Ten-microsecond molecular dynamics simulation of a fast-folding ww domain, Biophysical journal 94 (10) (2008) L75–L77.

[80] M. J. Harvey, G. Giupponi, G. D. Fabritiis, Acemd: accelerating biomolecular dynamics in the microsecond time scale, Journal of chemical theory and computation 5 (6) (2009) 1632–1639.

[81] K. Kempfer, J. Devmy, A. Dequidt, M. Couty, P. Malfreyt, Realistic coarse-grain model of cis-1, 4-polybutadiene: From chemistry to rheology, Macromolecules 52 (7) (2019) 2736–2747.

[82] K.-M. Tu, K. Kim, N. Matubayasi, Spatial-decomposition analysis of viscosity with application to lennard-jones fluid, Journal of Chemical Physics 148 (9) (2018) 094501.

[83] K.-M. Tu, R. Ishizuka, N. Matubayasi, Spatial-decomposition analysis of electrical conductivity in concentrated electrolyte solution, Journal of Chemical Physics 141 (4) (2014) 044126.

[84] K.-M. Tu, R. Ishizuka, N. Matubayasi, Spatial-decomposition analysis of electrical conductivity in ionic liquid, Journal of Chemical Physics 141 (24) (2014) 244507.

[85] Y. Ishii, N. Yamamoto, N. Matubayasi, B. W. Zhang, D. Cui, R. M. Levy, Spatially-decomposed free energy of solvation based on the endpoint density-functional method, Journal of Chemical Theory and Computation 15 (2019) 2896. doi:10.1021/acs.jctc.8b01309.

[86] S. Pasche, S. M. De Paul, J. Vörös, N. D. Spencer, M. Textor, Poly (l-lysine)-graft-poly (ethylene glycol) assembled monolayers on niobium oxide surfaces: A quantitative study of the influence of polymer interfacial architecture on resistance to protein adsorption by tof-sims and in situ owls, Langmuir 19 (22) (2003) 9216–9225.

[87] S. Horiuchi, D. Yin, T. Ougizawa, Nanoscale analysis of polymer interfaces by energy-filtering transmission electron microscopy, Macromolecular Chemistry and Physics 206 (7) (2005) 725–731.

[88] C. K. Wong, H. Gu, B. Xu, M. M. Yuen, A new approach in measuring cu–emc adhesion strength by afm, IEEE transactions on components and packaging technologies 29 (3) (2006) 543–550.

[89] M.-L. Abel, R. P. Digby, I. W. Fletcher, J. F. Watts, Evidence of specific interaction between γ-glycidoxypropyltrimethoxysilane and oxidized aluminium using high-mass resolution tof-sims, Surface and interface analysis 29 (2) (2000) 115–125.

[90] M. Kotera, Y. Urushihara, D. Izumo, T. Nishino, Interfacial structure of all-polyethylene laminate using scanning thermal microscope and nano-Raman spectroscope, Polymer 53 (9) (2012) 1966–1971.

[91] S. M. Foiles, M. I. Baskes, M. S. Daw, Embedded-atom-method functions for the fcc metals Cu, Ag, Au, Ni, Pd, Pt, and their alloys, Physical Review B 33 (12) (1986) 7983–7991.

[92] K. W. Jacobsen, J. K. Norskov, M. J. Puska, Interatomic interactions in the effective-medium theory, Physical Review B 35 (14) (1987) 7423–7442.

[93] S. L. Mayo, B. D. Olafson, W. A. Goddard III, DREIDING: A Generic Force Field for Molecular Simulations, Journal of Physical chemistry 101 (Suite 540) (1990) 8897–8909.

[94] H. Heinz, R. A. Vaia, B. L. Farmer, R. R. Naik, Accurate simulation of surfaces and interfaces of face-centered cubic metals using 12-6 and 9-6 lennard-jones potentials, Journal of Physical Chemistry C 112 (44) (2008) 17281–17290.

[95] S. J. Plimpton, A. P. Thompson, Computational aspects of many-body potentials, MRS bulletin 37 (05) (2012) 513–521.

[96] B. Jelinek, S. Groh, M. F. Horstemeyer, J. Houze, S.-G. Kim, G. J. Wagner, A. Moitra, M. I. Baskes, Modified embedded atom method potential for al, si, mg, cu, and fe alloys, Physical Review B 85 (24) (2012) 245102.

[97] H. Heinz, T. J. Lin, R. Kishore Mishra, F. S. Emami, Thermodynamically consistent force fields for the assembly of inorganic, organic, and biological nanostructures: The INTERFACE force field, Langmuir 29 (6) (2013) 1754–1765.

[98] H. Hao, D. Lau, Atomistic modeling of metallic thin films by modified embedded atom method, Applied Surface Science 422 (2017) 1139–1146.

[99] A. Taga, M. Yasuda, H. Kawata, Y. Hirai, Impact of molecular size on resist filling process in nanoimprint lithography: Molecular dynamics study, Journal of Vacuum Science & Technology B 28 (6) (2010) C6M68–C6M71.

[100] M. Yasuda, K. Araki, A. Taga, A. Horiba, H. Kawata, Y. Hirai, Computational study on polymer filling process in nanoimprint lithography, Microelectronic Engineering 88 (8) (2011) 2188–2191.

[101] S. Yang, S. Yu, M. Cho, Influence of mold and substrate material combinations on nanoimprint lithography process: MD simulation approach, Applied Surface Science 301 (2014) 189–198.

[102] M. Zhou, B. Jiang, C. Weng, Molecular dynamics study on polymer filling into nano-cavity by injection molding, Computational Materials Science 120 (2016) 36–42.

[103] I. Bitsanis, G. Hadziioannou, Molecular dynamics simulations of the structure and dynamics of confined polymer melts, The Journal of Chemical Physics 92 (6) (1990) 3827.

[104] Y. Kong, C. W. Manke, W. G. Madden, A. G. Schlijper, Simulation of a confined polymer in solution using the dissipative particle dynamics method, International Journal of Thermophysics 15 (6) (1994) 1093–1101.

[105] T. Aoyagi, J.-i. Takimoto, M. Doi, Molecular dynamics study of polymer melt confined between walls, The Journal of Chemical Physics 115 (1) (2001) 552–559.

[106] Y. Li, J. Xu, D. Li, Molecular dynamics simulation of nanoscale liquid flows, Microfluidics and Nanofluidics 9 (6) (2010) 1011–1031.

[107] K. Kadau, P. Lomdahl, B. Holian, T. Germann, D. Kadau, P. Entel, D. Wolf, M. Kreth, F. Westerhoff, Molecular-dynamics study of mechanical deformation in nano-crystalline aluminum, Metallurgical and materials transactions A 35 (9) (2004) 2719–2723.

[108] H. Wu, Molecular dynamics simulation of loading rate and surface effects on the elastic bending behavior of metal nanorod, Computational Materials Science 31 (3) (2004) 287–291.

[109] E. Seppälä, J. Belak, R. Rudd, Effect of stress triaxiality on void growth in dynamic fracture of metals: a molecular dynamics study, Physical Review B 69 (13) (2004) 134101.

[110] Q. Pei, C. Lu, F. Fang, H. Wu, Nanometric cutting of copper: A molecular dynamics study, Computational Materials Science 37 (4) (2006) 434–441.

[111] Q. Pei, C. Lu, H. Lee, Large scale molecular dynamics study of nanometric machining of copper, Computational Materials Science 41 (2) (2007) 177–185.

[112] V. Varshney, S. S. Patnaik, A. K. Roy, B. L. Farmer, A molecular dynamics study of epoxy-based networks: cross-linking procedure and prediction of molecular and material properties, Macromolecules 41 (18) (2008) 6837–6842.

[113] C. Li, A. Strachan, Molecular simulations of crosslinking process of thermosetting polymers, Polymer 51 (25) (2010) 6058–6070.

[114] S. G. Lee, S. S. Jang, J. Kim, G. Kim, Distribution and diffusion of water in model epoxy molding compound: molecular dynamics simulation approach, IEEE Transactions on Advanced Packaging 33 (2) (2010) 333–339.

[115] C. Li, A. Strachan, Molecular dynamics predictions of thermal and mechanical properties of thermoset polymer epon862/detda, Polymer 52 (13) (2011) 2920–2928.

[116] C. Li, G. A. Medvedev, E.-W. Lee, J. Kim, J. M. Caruthers, A. Strachan, Molecular dynamics simulations and experimental studies of the thermomechanical response of an epoxy thermoset polymer, Polymer 53 (19) (2012) 4222–4230.

[117] J. J. Gerdy, W. A. Goodard, Atomistic structure for self-assembled monolayers of alkanethiols on au (111) surfaces, Journal of the American Chemical Society 118 (13) (1996) 3233–3236.

[118] H. Heinz, B. L. Farmer, R. B. Pandey, J. M. Slocik, S. S. Patnaik, R. Pachter, R. R. Naik, Nature of molecular interactions of peptides with gold, palladium, and pd- au bimetal surfaces in aqueous solution, Journal of the American Chemical Society 131 (28) (2009) 9704–9714.

[119] T. Iwasaki, Molecular dynamics study on the effect of lattice mismatch on adhesion strength between organic materials and metals, Journal of the Society of Materials Science, Japan 58 (3) (2009) 257–261.

[120] H. Heinz, K. C. Jha, J. Luettmer-Strathmann, B. L. Farmer, R. R. Naik, Polarization at metal–biomolecular interfaces in solution, Journal of The Royal Society Interface (2011) rsif20100318.

[121] R. Coppage, J. M. Slocik, B. D. Briggs, A. I. Frenkel, H. Heinz, R. R. Naik, M. R. Knecht, Crystallographic recognition controls peptide binding for bio-based nanomaterials, Journal of the American Chemical Society 133 (32) (2011) 12346–12349.

[122] J. Feng, R. B. Pandey, R. J. Berry, B. L. Farmer, R. R. Naik, H. Heinz, Adsorption mechanism of single amino acid and surfactant molecules to au $\{111\}$ surfaces in aqueous solution: design rules for metal-binding molecules, Soft Matter 7 (5) (2011) 2113–2120.

[123] J. Feng, J. M. Slocik, M. Sarikaya, R. R. Naik, B. L. Farmer, H. Heinz, Influence of the shape of nanostructured metal surfaces on adsorption of single peptide molecules in aqueous solution, Small 8 (7) (2012) 1049–1059.

[124] C. Bayley, P. Cieplak, W. Cornell, P. Kollman, A well-behaved electrostatic potential based method using charge restraints for deriving atomic charges: The resp method, J. Phys. Chem 97 (1993) 10269–10280.

[125] J. Wang, W. Wang, P. A. Kollman, D. A. Case, Automatic atom type and bond type perception in molecular mechanical calculations, Journal of molecular graphics and modelling 25 (2) (2006) 247–260.

[126] M. J. Frisch, G. W. Trucks, H. B. Schlegel, G. E. Scuseria, M. A. Robb, J. R. Cheeseman, G. Scalmani, V. Barone, B. Mennucci, G. A. Petersson, H. Nakatsuji, M. Caricato, X. Li, H. P. Hratchian, A. F. Izmaylov, J. Bloino, G. Zheng, J. L. Sonnenberg, M. Hada, M. Ehara, K. Toyota, R. Fukuda, J. Hasegawa, M. Ishida, T. Nakajima, Y. Honda, O. Kitao, H. Nakai, T. Vreven, J. A. Montgomery, Jr., J. E. Peralta, F. Ogliaro, M. Bearpark, J. J. Heyd, E. Brothers, K. N. Kudin, V. N. Staroverov, R. Kobayashi, J. Normand, K. Raghavachari, A. Rendell, J. C. Burant, S. S. Iyengar, J. Tomasi, M. Cossi, N. Rega, J. M. Millam, M. Klene, J. E. Knox, J. B. Cross, V. Bakken, C. Adamo, J. Jaramillo, R. Gomperts, R. E. Stratmann, O. Yazyev, A. J. Austin, R. Cammi, C. Pomelli, J. W. Ochterski, R. L. Martin, K. Morokuma, V. G. Zakrzewski, G. A. Voth, P. Salvador, J. J. Dannenberg, S. Dapprich, A. D. Daniels, . Farkas, J. B. Foresman, J. V. Ortiz, J. Cioslowski, D. J. Fox, Gaussian09 Revision E.01, gaussian Inc. Wallingford CT 2009.

[127] W. C. Swope, H. C. Andersen, P. H. Berens, K. R. Wilson, A computer simulation method for the calculation of equilibrium constants for the formation of physical clusters of molecules: Application to small water clusters, The Journal of Chemical Physics 76 (1) (1982) 637–649.

[128] S. Plimpton, Fast Parallel Algorithms for Short-Range Molecular Dynamics, Journal of Computational Physics 117 (1) (1995) 1–19.

[129] R. W. Hockney, J. W. Eastwood, Computer simulation using particles, crc Press, 1988.

[130] S. Plimpton, R. Pollock, M. Stevens, Particle-mesh ewald and rrespa for parallel molecular dynamics simulations., in: Parallel Processing for Scientific Computing, Eighth SIAM Conference, 1997.

[131] S. Nosé, A unified formulation of the constant temperature molecular dynamics methods, The Journal of chemical physics 81 (1) (1984) 511–519.

[132] W. G. Hoover, Canonical dynamics: equilibrium phase-space distributions, Physical review A 31 (3) (1985) 1695.

[133] G. J. Martyna, D. J. Tobias, M. L. Klein, Constant pressure molecular dynamics algorithms, The Journal of Chemical Physics 101 (5) (1994) 4177–4189.

[134] W. Shinoda, M. Shiga, M. Mikami, Rapid estimation of elastic constants by molecular dynamics simulation under constant stress, Physical Review B 69 (13) (2004) 134103.

[135] Winmostar.
URL `https://winmostar.com/en/`

[136] L. Vitos, A. V. Ruban, H. L. Skriver, J. Kollár, The surface energy of metals, Surface Science 411 (1998) 186–202.

[137] F. Aqra, A. Ayyad, Surface energies of metals in both liquid and solid states, Applied Surface Science 257 (15) (2011) 6372–6379.

[138] M. Naritomi, N. Andoh, Process for production of highly corrosion-resistant composite, US Patent 8322013.

[139] H. Mori, N. Matubayasi, MD simulation analysis of resin filling into nano-sized pore formed on metal surface, Applied Surface Science 427 (Part A) (2018) 1084 – 1091.

[140] S. Kim, D. E. Lee, W. I. Lee, Molecular dynamic simulation on the effect of polymer molecular size in thermal nanoimprint lithographic (T-NIL) process, Tribology Letters 49 (2) (2013) 421–430.

[141] M. Kaji, K. Nakahara, T. Endo, Synthesis of a bifunctional epoxy monomer containing biphenyl moiety and properties of its cured polymer with phenol novolac, Journal of Applied Polymer Science 74 (3) (1999) 690–698.

[142] S. Han, H. Gyu Yoon, K. S. Suh, W. Gun Kim, T. Jin Moon, Cure kinetics of biphenyl epoxy-phenol novolac resin system using triphenylphosphine as catalyst, Journal of Polymer Science Part A Polymer Chemistry 37 (6) (1999) 713–720.

[143] M. L. Auad, S. R. Nutt, P. M. Stefani, M. I. Aranguren, Rheological study of the curing kinetics of epoxy–phenol novolac resin, Journal of applied polymer science 102 (5) (2006) 4430–4439.

[144] Y.-M. Kim, B.-J. Lee, M. Baskes, Modified embedded-atom method interatomic potentials for Ti and Zr, Physical Review B 74 (1) (2006) 014101.

[145] M. I. Pascuet, Atomic interaction of the MEAM type for the study of intermetallics in the Al-U alloy, Journal of Nuclear Materials journal 467 (1) (2015) 229–239.

[146] J.-P. Ryckaert, G. Ciccotti, H. J. Berendsen, Numerical integration of the cartesian equations of motion of a system with constraints: molecular dynamics of n-alkanes, Journal of Computational Physics 23 (3) (1977) 327–341.

[147] T. Schneider, E. Stoll, Molecular-dynamics study of a three-dimensional one-component model for distortive phase transitions, Physical Review B 17 (3) (1978) 1302.

[148] B. Dünweg, W. Paul, Brownian dynamics simulations without gaussian random numbers, International Journal of Modern Physics C 2 (03) (1991) 817–827.

[149] D. Hofmann, L. Fritz, J. Ulbrich, C. Schepers, M. Böhning, Detailed-atomistic molecular modeling of small molecule diffusion and solution processes in polymeric membrane materials, Macromolecular theory and simulations 9 (6) (2000) 293–327.

[150] N. C. Karayiannis, V. G. Mavrantzas, D. N. Theodorou, Detailed atomistic simulation of the segmental dynamics and barrier properties of amorphous poly (ethylene terephthalate) and poly (ethylene isophthalate), Macromolecules 37 (8) (2004) 2978–2995.

[151] D. M. Heyes, Pressure tensor of partial-charge and point-dipole lattices with bulk and surface geometries, Physical Review B 49 (2) (1994) 755.

[152] A. P. Thompson, S. J. Plimpton, W. Mattson, General formulation of pressure and stress tensor for arbitrary many-body interaction potentials under periodic boundary conditions, The Journal of chemical physics 131 (15) (2009) 154107.

[153] T. W. Sirk, S. Moore, E. F. Brown, Characteristics of thermal conductivity in classical water models, The Journal of chemical physics 138 (6) (2013) 064505.

[154] K. Tanaka, Y. Tateishi, Y. Okada, T. Nagamura, M. Doi, H. Morita, Interfacial mobility of polymers on inorganic solids, Journal of Physical Chemistry B 113 (14) (2009) 4571–4577.

[155] Y. Fujii, Z. Yang, J. Leach, H. Atarashi, K. Tanaka, O. K. Tsui, Affinity of polystyrene films to hydrogen-passivated silicon and its relevance to the t_g of the films, Macromolecules 42 (19) (2009) 7418–7422.

[156] H. Tsuruta, Y. Fujii, N. Kai, H. Kataoka, T. Ishizone, M. Doi, H. Morita, K. Tanaka, Local conformation and relaxation of polystyrene at substrate interface, Macromolecules 45 (11) (2012) 4643–4649.

[157] S. Shimomura, M. Inutsuka, N. L. Yamada, K. Tanaka, Unswollen layer of cross-linked polyisoprene at the solid interface, Polymer 105 (2016) 526–531.

[158] O. Borodin, G. D. Smith, R. Bandyopadhyaya, O. Byutner, Molecular dynamics study of the influence of solid interfaces on poly (ethylene oxide) structure and dynamics, Macromolecules 36 (20) (2003) 7873–7883.

[159] V. A. Harmandaris, K. C. Daoulas, V. G. Mavrantzas, Molecular dynamics simulation of a polymer melt/solid interface: Local dynamics and chain mobility in a thin film of polyethylene melt adsorbed on graphite, Macromolecules 38 (13) (2005) 5796–5809.

[160] A. Taga, M. Yasuda, H. Kawata, Y. Hirai, Impact of molecular size on resist filling process in nanoimprint lithography: Molecular dynamics study, Journal of Vacuum Science and Technology B 28 (6) (2010) C6M68–C6M71.

[161] Y. Suganuma, S. Yamamoto, T. Kinjo, T. Mitsuoka, K. Umemoto, Wettability of al2o3 surface by organic molecules: Insights from molecular dynamics simulation, Journal of Physical Chemistry B 121 (42) (2017) 9929–9935.

[162] H. Mori, N. Matubayasi, Md simulation analysis of resin filling into nano-sized pore formed on metal surface, Applied Surface Science 427 (2018) 1084–1091.

[163] H. Mori, N. Matubayasi, Resin filling into nano-sized pore on metal surface analyzed by all-atom molecular dynamics simulation over a variety of resin and pore sizes, Polymer 150 (2018) 360–370.

[164] L. V. Woodcock, Equation of state for the viscosity of lennard-jones fluids, AIChE Journal 52 (2) (2006) 438–446.

[165] M. Heyden, J. Sun, S. Funkner, G. Mathias, H. Forbert, M. Havenith, D. Marx, Dissecting the thz spectrum of liquid water from first principles via correlations in time and space, Proceedings of the National academy of Sciences of the United States of America 107 (27) (2010) 12068–12073.

[166] V. A. Levashov, J. R. Morris, T. Egami, Viscosity, shear waves, and atomic-level stress-stress correlations, Physical Review Letters 106 (11) (2011) 115703.

[167] Y. Kubota, A. Yoshimori, N. Matubayasi, M. Suzuki, R. Akiyama, Molecular dynamics study of fast dielectric relaxation of water around a molecular-sized ion, Journal of Chemical Physics 137 (22) (2012) 224502.

[168] M. Śmiechowski, H. Forbert, D. Marx, Spatial decomposition and assignment of infrared spectra of simple ions in water from mid-infrared to thz frequencies: Li+ (aq) and f-(aq), Journal of Chemical Physics 139 (1) (2013) 014506.

[169] R. Jones, D. Ward, J. Templeton, Spatial resolution of the electrical conductance of ionic fluids using a green-kubo method, Journal of Chemical Physics 141 (18) (2014) 184110.

[170] M. Śmiechowski, J. Sun, H. Forbert, D. Marx, Solvation shell resolved thz spectra of simple aqua ions–distinct distance-and frequency-dependent contributions of solvation shells, Physical Chemistry Chemical Physics 17 (13) (2015) 8323–8329.

[171] E. Pluhařová, P. Jungwirth, N. Matubayasi, O. Marsalek, Structure and dynamics of the hydration shell: Spatially decomposed time correlation approach, Journal of Chemical Theory and Computation 15 (2019) 803.

[172] N. Matubayasi, Spatial-decomposition analysis of electrical conductivity, Chemical Record 19 (2019) 723–724.

[173] N. Matubayasi, L. H. Reed, R. M. Levy, Thermodynamics of the hydration shell. 1. excess energy of a hydrophobic solute, Journal of Physical Chemistry 98 (41) (1994) 10640–10649.

[174] N. Matubayasi, R. M. Levy, Thermodynamics of the hydration shell. 2. excess volume and compressibility of a hydrophobic solute, Journal of Physical Chemistry 100 (7) (1996) 2681–2688.

[175] N. Matubayasi, E. Gallicchio, R. M. Levy, On the local and nonlocal components of solvation thermodynamics and their relation to solvation shell models, Journal of Chemical Physics 109 (12) (1998) 4864–4872.

[176] G. Mogami, M. Suzuki, N. Matubayasi, Spatial-decomposition analysis of energetics of ionic hydration, Journal of Physical Chemistry B 120 (8) (2016) 1813–1821.

[177] S. Sen, S. K. Kumar, P. Keblinski, Viscoelastic properties of polymer melts from equilibrium molecular dynamics simulations, Macromolecules 38 (3) (2005) 650–653.

[178] M. Vladkov, J.-L. Barrat, Linear and nonlinear viscoelasticity of a model unentangled polymer melt: molecular dynamics and rouse modes analysis, Macromolecular Theory and Simulations 15 (3) (2006) 252–262.

[179] J.-X. Hou, C. Svaneborg, R. Everaers, G. S. Grest, Stress relaxation in entangled polymer melts, Physical Review Letters 105 (6) (2010) 068301.

[180] D. Squire, A. Holt, W. Hoover, Isothermal elastic constants for argon. theory and monte carlo calculations, Physica 42 (3) (1969) 388–397.

[181] S. R. Williams, D. J. Evans, Viscoelastic properties of crystals, Journal of Chemical Physics 131 (2) (2009) 024115.

[182] H. Yoshino, Replica theory of the rigidity of structural glasses, Journal of Chemical Physics 136 (21) (2012) 214108.

[183] J. P. Wittmer, H. Xu, J. Baschnagel, Simple average expression for shear-stress relaxation modulus, Physical Review E 91 (1) (2015) 022107.

[184] K. Kremer, G. S. Grest, Dynamics of entangled linear polymer melts: A molecular-dynamics simulation, Journal of Chemical Physics 92 (8) (1990) 5057–5086.

[185] H. Morita, K. Tanaka, T. Kajiyama, T. Nishi, M. Doi, Study of the glass transition temperature of polymer surface by coarse-grained molecular dynamics simulation, Macromolecules 39 (18) (2006) 6233–6237.

[186] A. Kinloch, The science of adhesion, Journal of Materials Science 15 (9) (1980) 2141–2166.

[187] T. Okamatsu, Y. Yasuda, M. Ochi, Thermodynamic work of adhesion and peel adhesion energy of dimethoxysilyl-terminated polypropylene oxide/epoxy resin system jointed with polymeric substrates, Journal of Applied Polymer Science 80 (11) (2001) 1920–1930.

[188] T. Aoyagi, J. Takimoto, M. Doi, Molecular dynamics study of polymer melt confined between walls, Journal of Chemical Physics 115 (1) (2001) 552–559.

[189] V. L. Hughes, R. W. Looney, Fully saturated petroleum resin and hot melt pressure sensitive adhesive formulations utilizing same as tackifier, US Patent 4,714,749 (Dec. 22 1987).

[190] S. Akiyama, Y. Kobori, A. Sugisaki, T. Koyama, I. Akiba, Phase behavior and pressure sensitive adhesive properties in blends of poly (styrene-b-isoprene-b-styrene) with tackifier resin, Polymer 41 (11) (2000) 4021–4027.

[191] J. K. Kim, W. H. Kim, D. H. Lee, Adhesion properties of uv crosslinked polystyrene-block-polybutadiene-block-polystyrene copolymer and tackifier mixture, Polymer 43 (18) (2002) 5005–5010.

[192] Y. C. Leong, L. M. S. Lee, S. N. Gan, The viscoelastic properties of natural rubber pressure-sensitive adhesive using acrylic resin as a tackifier, Journal of Applied Polymer Science 88 (8) (2003) 2118–2123.

[193] M. Sasaki, K. Fujita, M. Adachi, S. Fujii, Y. Nakamura, Y. Urahama, The effect of tackifier on phase structure and peel adhesion of a triblock copolymer pressure-sensitive adhesive, International Journal of Adhesion and Adhesives 28 (7) (2008) 372–381.

[194] J. Irving, J. G. Kirkwood, The statistical mechanical theory of transport processes. iv. the equations of hydrodynamics, Journal of Chemical Physics 18 (6) (1950) 817–829.

[195] W. Noll, On the continuity of the solid and fluid states, Journal of Rational Mechanics and Analysis 4 (1955) 3–81.

[196] R. J. Hardy, Formulas for determining local properties in molecular-dynamics simulations: Shock waves, Journal of Chemical Physics 76 (1) (1982) 622–628.

[197] P. Schofield, J. R. Henderson, Statistical mechanics of inhomogeneous fluids, Proceedings of the Royal Society of London Series A 379 (1776) (1982) 231–246.

[198] A. Murdoch, The motivation of continuum concepts and relations from discrete considerations, Computational Materials ScienceQuarterly Journal of Mechanics and Applied Mathematics 36 (2) (1983) 163–187.

[199] R. Goetz, R. Lipowsky, Computer simulations of bilayer membranes: self-assembly and interfacial tension, Journal of Chemical Physics 108 (17) (1998) 7397–7409.

[200] J. A. Zimmerman, E. B. WebbIII, J. Hoyt, R. E. Jones, P. Klein, D. J. Bammann, Calculation of stress in atomistic simulation, Modelling and Simulation in Materials Science and Engineering 12 (4) (2004) S319.

[201] A. I. Murdoch, A critique of atomistic definitions of the stress tensor, Journal of Elasticity 88 (2) (2007) 113–140.

[202] N. C. Admal, E. B. Tadmor, A unified interpretation of stress in molecular systems, Journal of Elasticity 100 (1-2) (2010) 63–143.

[203] E. Lindahl, O. Edholm, Spatial and energetic-entropic decomposition of surface tension in lipid bilayers from molecular dynamics simulations, Journal of Chemical Physics 113 (9) (2000) 3882–3893.

[204] S. Ollila, M. T. Hyvönen, I. Vattulainen, Polyunsaturation in lipid membranes: dynamic properties and lateral pressure profiles, Journal of Physical Chemistry B 111 (12) (2007) 3139–3150.

[205] O. S. Ollila, H. J. Risselada, M. Louhivuori, E. Lindahl, I. Vattulainen, S. J. Marrink, 3d pressure field in lipid membranes and membrane-protein complexes, Physical Review Letters 102 (7) (2009) 078101.

[206] M. Soleymani, M. Parsa, H. Mirzadeh, Molecular dynamics simulation of stress field around edge dislocations in aluminum, Computational Materials Science 84 (2014) 83–96.

[207] S. Ma, N. Ren, J. Zhang, Observation of morphology and stress distribution around dislocation in ni3al on the atomic scale, Solid State Communication 211 (2015) 4–9.

[208] J. M. Vanegas, A. Torres-Sánchez, M. Arroyo, Importance of force decomposition for local stress calculations in biomembrane molecular simulations, Journal of Chemical Theory and Computation 10 (2) (2014) 691–702.

[209] A. Torres-Sánchez, J. M. Vanegas, M. Arroyo, Examining the mechanical equilibrium of microscopic stresses in molecular simulations, Physical Review Letters 114 (25) (2015) 258102.

[210] N. C. Admal, E. B. Tadmor, The non-uniqueness of the atomistic stress tensor and its relationship to the generalized beltrami representation, Journal of the Mechanics and Physics of Solids 93 (2016) 72–92.

[211] K. M. Nakagawa, H. Noguchi, Nonuniqueness of local stress of three-body potentials in molecular simulations, Physical Review E 94 (5) (2016) 053304.

[212] M. Rubinstein, R. H. Colby, et al., Polymer physics, Vol. 23, Oxford university press New York, 2003.

List of Publications, Patents, and Conference Presentations

Main papers:

1. H. Mori and N. Matubayasi, ”MD simulation analysis of resin filling into nano-sized pore formed on metal surface”, *Applied Surface Science* 427, Part A, 1084-1091 (2018).
2. H. Mori and N. Matubayasi, ”Resin filling into nano-sized pore on metal surface analyzed by all-atom molecular dynamics simulation over a variety of resin and pore sizes”, *Polymer* 150, 360-370 (2018).
3. H. Mori and N. Matubayasi, ”Local viscoelasticity at resin-metal interface analyzed with spatial-decomposition formula for relaxation modulus”, *Journal of Chemical Physics* 151, 114904 (14 pages) (2019).

Patents:

1. Patent application to be examined No.2018-75805
2. Patent application to be examined No.2019-148446

Conference Presentations:

1. H, Mori; N. Matubayasi, ”MD simulation of resin filling into nano-sized pore”, *30th Molecular Simulation Symposium*, 119P, Osaka, Japan, November 30 - December 2, 2016 (Poster, **Student Presentation Award**)
2. H, Mori; N. Matubayasi, ”MD Simulation Analysis of Resin Filling into Nano-Sized Pore Formed on Metal Surface”, *40th Symposium on Solution Chemistry of Japan*, P40, Hyogo, Japan, October 18-20, 2017 (Poster)
3. H, Mori; N. Matubayasi, ”All-atom MD analysis of resin filling into nano-Sized pore formed on metal surface”, *31th Molecular Simulation Symposium*, 318S (165P), Ishikawa, Japan, November 29 - December 1, 2017 (Oral and Poster)
4. H, Mori; N. Matubayasi, ”Local Viscoelasticity at Resin-Metal Interface Analyzed with Spatial-Decomposition Formula for Relaxation Modulus”, *68th SPSJ Annual Meeting*, 2Pf026, Osaka, Japan, March 29-31, 2019 (Poster)

Acknowledgement

The author is greatly indebted to Professor Nobuyuki Matubayasi for their constant guidance and helpful advice throughout this work. We are grateful to Prof. Kang Kim of Osaka University for valuable discussion. The author is sincerely grateful to Professor Masayoshi Nakano and Professor Shinji Sakai for a number of valuable comments and criticism during the completion of this thesis.

The author acknowledges all members of the Matubayasi laboratory for their friendship. Special thanks are given to the following colleagues for the discussions: Dr. Kazuo Yamada, Dr. Yoshiki Ishii, Dr. Hidekazu Kojima.

This works is supported through the HPCI System Research Project (Project IDs: hp180045, hp180173, and hp190149) partly using Reedbush-U at The University of Tokyo and ITO at Kyushu University, as well as CX400 at Nagoya University, OCTOPUS at Osaka University, and the K computer at RIKEN Advanced Institute for Computational Science.

The author also acknowledges the financial support by Sensor & Semiconductor Packaging Division of DENSO CORPORATION. I am deeply grateful to Mr. Naohiko Hirano, Mr. Nobumasa Ueda, Mr. Hirokazu Imai, Mr. Akiyoshi Asai, Dr. Ryosuke Izumi for their continuous encouragement and supports. Special thanks are given to the following colleagues in DENSO CORPORATION for the useful advise: Dr. Koichi Tanaka, Mr. Kazuki Koda, and Mr. Akito Nagakubo.

Finally, the author sincerely wishes to thank his family, Atsuko Mori, Keita Mori, and Shiori Mori for their moral support and warm encouragements.

Hodaka Mori
Division of Chemical Engineering
Graduate School of Engineering Science
Osaka University, Toyonaka, Osaka 560-8531, Japan